RESOLUTION IN NEUTRON SPECTROMETRY; PHONONS IN $Cu_{63}Ni_{21}Zn_{16}$

A STUDY OF THE RESOLUTION OF A TRIPLE-AXIS SPECTROMETER
AND
MEASUREMENT OF THE PHONON SPECTRUM OF THE TERNARY ALLOY $Cu_{.63}Ni_{.21}Zn_{.16}$

By

ANDRÉ LAROSE, B.Sc.

A Thesis
Submitted to the Faculty of Graduate Studies
in Partial Fulfilment of the Requirements
for the Degree
Master of Sciences

McMaster University

October 1970

MASTER OF SCIENCES (1970)
(Physics)

McMASTER UNIVERSITY
Hamilton, Ontario.

TITLE: A Study of the Resolution of a Triple-axis Spectrometer and Measurement of the Phonon Spectrum of the Ternary Alloy $Cu_{.63}Ni_{.21}Zn_{.16}$

AUTHOR: André Larose, B.Sc. (Université de Montréal).

SUPERVISOR: Professor B. N. Brockhouse.

NUMBER OF PAGES: ix, 166.

SCOPE AND CONTENTS: The phonon dispersion relation in the principal symmetry directions of a crystal of Cu-Ni-Zn was measured at 298°K by means of inelastic scattering of thermal neutrons. The specimen had an electronic concentration per atom very close to that of pure copper and it came as no surprise that no significant shift in the phonon spectrum relative to that of pure copper could be observed.

The particular specimen used had a poor mosaic distribution; this contribution was taken into account in the calculation of the line shape and it was found that the widths of the neutron groups could be well accounted for in this way.

The appendix is divided into six parts, four of which contain a description of projects of secondary importance that were realized.

Acknowledgements.

My gratitude goes to Dr. B. N. Brockhouse for having introduced me to this powerful probe of the condensed state which is the technique of the scattering of thermal neutrons. It was always considered an honour to have the privilege to work with him.

Most of the experimental work was done at the Chalk River Nuclear Laboratory and the cooperation of the Atomic Energy of Canada is sincerely acknowledged.

Many thanks also to all the people in our group: Dr. D. Hallman (now at Laurentian University), and Messrs. J. Copley, D. Dutton, R. Dymond, W. Kamitakahara, A. P. Roy and H. C. Teh for their guidance in introducing me to experimental work and for many instructive discussions.

The chemical analysis of the Cu-Ni-Zn specimen was done thanks to the cooperation of Dr. O. E. Hileman and to the devotion of one of his graduate student, Mister R. Prime, without whose help the experimental chemistry work would not have been attempted.

The financial assistance of the National Research Council contributed to make this work possible.

Finally, a debt of gratitude goes to the typist, Mrs. S. McQueen for having inherited of a difficult manuscript and to both Mrs. S. Duke and Mr. J. Ho whose artistic talent is responsible for a large portion of the drawings.

TABLE OF CONTENT

List of figures

Page

List of tables

I). Introduction.

Ever since that it was made technically feasible, the scattering of thermal neutrons has revealed itself as a most sensitive probe of the micro-dynamics of systems in the condensed state. This reflected by the number of papers being published on the subject [Appendix A-6] and by the ever-increasing number of neutron spectrometers being used in the world. The virtue of the thermal neutron as a probe stems from two facts. Firstly, its momentum and energy lie within the same range as the pseudo-momentum and energy of excitations found in many-body systems. This makes for an easily observable detection of the interaction between an excitation and a neutron. Secondly, because of its permanent magnetic moment as well as its lack of electric charge, the neutron does interact with the scattering system through a short range potential which is either of a nuclear or magnetic nature. If this potential is represented by a Fermi pseudo-potential, perturbation theory can be used and the theory of linear response is applicable (Taylor [70]).

However, these merits of the neutron probe are offset by the relatively low intensities of the sources (nuclear reactors) of thermal neutrons and this is the cause of the present limitations of this technique. In fact, the scattering of thermal neutrons is essentially a spectrometry technique and this aspect of its nature is more evident in the case of inelastic scattering. Because of this, it is conflicted between the requirements of a high signal intensity and of good resolution.

The optimization in signal to noise ratio is obtained by a judicious compromise between these conflicting requirements and it is known that it is possible to gain intensity from focusing considerations. One says that focusing occurs when there is a correlation between the imperfect instrumental resolution and the scattering surface of the specimen. A familiar case would be that of two crystals arranged in a parallel configuration (for elastic scattering). A similar situation may be obtained on a triple-axis neutron spectrometer and it is aimed to demonstrate the validity of a model used to calculate line shapes by comparing the results of calculations with those experimentally measured on a specimen of Cu-Ni-Zn having a poor mosaic distribution.

The main body of this work is concerned with the resolution of a triple-axis neutron spectrometer. In the following sections, we will consider individually each of the factors affecting the measured intensity distribution in inelastic scattering. Section II-3 contains the theoretical derivation of the resolution matrix and is basic in all that follows; althought somewhat monotonous to read, it is a very general approach first derived by Cooper/Nathans [67] and it gives a precise expression for the resolution of the instrument in terms of all the experimental parameters. This expression is then integrated over the cross-section of the specimen in order to obtain the intensity distribution along the scan. This is the content of section II-4 where the line shape calculation was extended to the general case where the scattering plane is not parallel to a symmetry plane of the reciprocal lattice of the specimen. This is of rather academic interest since experiments are commonly performed in a symmetry plane. Section II-5 deals with the peculiar behaviour of the constant frequency surface for $[\zeta\zeta\zeta]_t$ phonons and the consequences on the line shape is discussed. The case of the real specimen crystal with its imperfect mosaic distribution is considered in section II-6. Finally, section II-7 is concerned with the shift between apparent and true peak position as caused by the composite action of the mosaic spread and the population factor.

Chapter III deals with empirical results of neutron scattering measurements made on a disordered alloy of Cu-Ni-Zn. After a brief introductory part where the reasons for choosing this alloy are explained, we proceed to the characterization of the specimen as to chemical composition, lattice parameter and mosaic distribution. Because of its poor mosaic distribution, the specimen afforded a double interest in the sense that not only did the dispersion curves corresponding to a particular electronic concentration were measured but also it afforded the occasion to perform a study of the resolution of a triple-axis neutron spectrometer in order to see the relative effect of poor mosaic distribution and atomic force constant disorder on the observed line width. Use was made of the theoretical results of chapter II and the validity of the calculations was verified by comparing the predictions with the measurements made on a good copper specimen. This being an homogeneous substance with comparativly little mosaic spread, then there is no contribution to the line width from mosaic spread or atomic force constants disorder.

The result of section II-7 are used to extract the true peak position from the apparent peak position in the case of phonons of transverse polarization. This chapter is terminated by presenting the results of the measurements of the dispersion curves for this specimen with an accompanying discussion.

* * * * *

A word about symbolism and convention. The symbols used are listed in table I-1 and will be faithfully adhered to throughout the text. Many differ from the ones usually used, but this type of change was made necessary in order to avoid any ambiguity. For exemple, the wave vectors (energies) of the neutron beam incident on and scattered from the specimen will be labeled $\underset{\sim}{k}_m$ ($\hbar\omega_m$) and $\underset{\sim}{k}_a$ ($\hbar\omega_a$) respectivly. The indices i=0,1,2,3 are reserved stricly to label the different regions of the spectrometer (see table I-1).

The thesis is divided into chapters which are dealing with the theoretical and experimental results separatly. The chapters are themselves divided into sections which are concerned with a well defined topic and the sections are possibly divided into sub-sections. Figures are labeled according to the chapter, section and sub-section (if any) where it is first refered from. The equations are refered to by giving a single number if it is to be found in the same section and including the chapter and section numbers if it is elsewhere in the text.

Table I-1: Notation.

$\underset{\sim}{k}_o$ ($\underset{\sim}{k}'$) : Value of a wave vector before (after) single scattering.

$\underset{\sim}{k}_m$ ($\underset{\sim}{k}_a$) : Value of an incident (analyzed) wave vector.

$\hat{x}$: Central value of a quantity "x".

$\tilde{x}$: Non-central value of a quantity "x".

$\underset{\sim}{Q} = \underset{\sim}{k}_m - \underset{\sim}{k}_a$; momentum-transfer. $\hbar\omega = \frac{\hbar^2}{2M}(k_m^2 - k_a^2)$; energy transfer.

M : mass of the neutron.

m (or m_k) : mass of an atom at the site "k" in the specimen crystal.

$\Delta\underset{\sim}{k}_m = \tilde{\underset{\sim}{k}}_m - \hat{\underset{\sim}{k}}_m$; $\Delta\underset{\sim}{k}_a = \tilde{\underset{\sim}{k}}_a - \hat{\underset{\sim}{k}}_a$; $\Delta\underset{\sim}{Q} = \tilde{\underset{\sim}{Q}} - \hat{\underset{\sim}{Q}}$; $\Delta\omega = \tilde{\omega} - \hat{\omega}$

α_i (β_i) : Horizontal (vertical) collimation angle in the i^{th} region.

γ_i (δ_i) : Horizontal (vertical) angular deviation from the central direction.

i^{th} region : i=0 (in-pile region);
i=1 (monochromator-to-specimen region);
i=2 (specimen-to-analyzer crystal region);
i=3 (analyzer crystal-to-counter region).

η_m (η'_m) : Horizontal (vertical) mosaic spread of the monochromator. [standard deviation].

η_a (η'_a) : same for the analyzer.

Γ : Any full width at half maximum.

II- Resolution in triple-axis neutron spectrometry.

1)- Transmission characteristics of a neutron collimator.

i)- In neutron scattering as well as in x-ray work, collimators are used to define the direction of propagation of the incident and scattered beams. Collimation serves to delimit angular divergence of the neutron flux impinging on the specimen and accepted by the analyser. This is a necessary requirement since a precise knowledge of the value of the momentum-transfer $\underset{\sim}{Q}$ requires well defined incident and scattered beams with respect to direction as well as to energy. This last requirement is determined by monochromating and analysing crystals properties which later will be considered.

An ideal collimator should allow perfect definition of the direction of propagation in both the horizontal and vertical planes. However, because of limited available neutron intensities, such a wasteful procedure is never adopted and it is usual to restrict collimation to the scattering plane only. This limitation is not as severe as it may seem since the component of the momentum transfer $\underset{\sim}{Q}$ perpendicular to the scattering plane contributes a second order effect in inelastic scattering performed in symmetry planes. However, the effect of vertical collimation can sometimes result in spurious peaks appearing over the neutron groups as was recently discovered by Copley [70], Cowley [70]

An obvious way to obtain collimation in the horizontal plane is to have a prismatic channel with the width smaller than the height inserted in the neutron beam. In practice, the vertical collimation is achieved by the beam tube channel and by the distances between monochromator, specimen and analyser. In order to maximize the through beam intensity, it is necessary to stack the collimating channels side by side to proportionally increase the transmitted intensity at no cost in horizontal collimation. This object is called a Soller-slit collimator.

II-1-ii) In this section we present a simple derivation of the transmission function of a collimator. A more rigorous approach, which proves hard to manipulate in practice , is given by Szabo [59]. The two methods essentially give similar conclusions because the small angle approximation is valid.

Using the same symbols as Szabo and Cooper/Nathans [67] we define the horizontal (vertical) characteristic angle of a collimator as $\alpha(\beta)$. This value depends on the physical arrangement of the Soller slits and is intuitively independant of the neutron energy. On the other hand, it depends on the mathematical object used to characterize the collimator.

The characteristic angles are related to the physical dimensions in the following way. Assume a collimator of length L and plate spacing d.

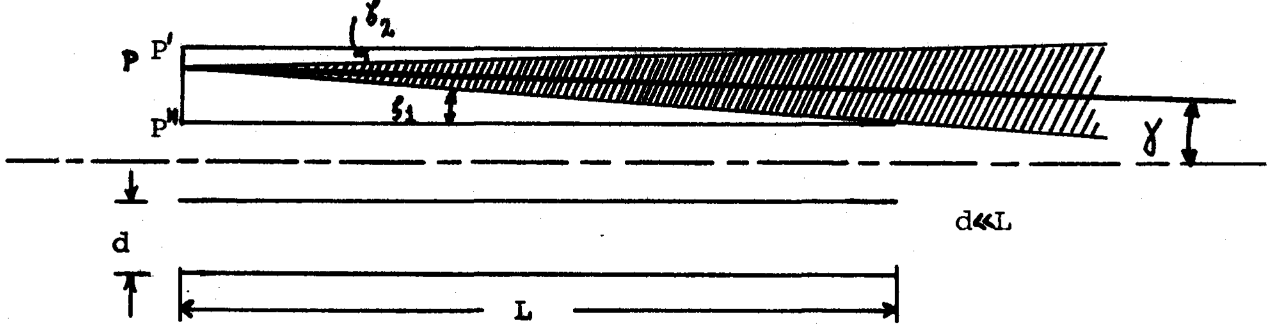

Fig. II-1-ii-1

From an optical analogy, it is possible to consider the plane P'P"i.e. the collimator inlet as a virtual neutron source(Huygens Principle). This is a valid approximation since the collimation is much smaller than the angular divergence of the incident beam; then for all practical purpose, the collimator inlet may be considered as an isotropically radiating source.

For any point on the P'P" plane, the horizontal angle subtended by the allowed paths is d/L assuming perfect absorption of the collimator walls for any other angle. The position of P defines the extremum paths by the angles ζ_1 and $\zeta_2$which satisfies:

$$\zeta_1 + \zeta_2 = d/L = \Gamma \qquad (1)$$

If we now imagine moving the point source P horizontally along P'P", the hatched region will change and the angle ζ_1 will vary linearly with the position of P. The transmission probability of a neutron from the vertical line source P to the collimator outlet region is then

1 if $-\zeta_2<\gamma<\zeta_1$
0 otherwise

$$\text{i.e. } T(\gamma,\zeta_1) = \theta(\zeta_1-\gamma)\,\theta(\gamma+\zeta_2) \qquad (2a)$$

$$\zeta_2 = \Gamma-\zeta_1 \qquad (2b)$$

Where $T(\gamma,\zeta_1)$ is the transmission probability of a neutron having a direction of propagation defined by γ and coming from point P as defined by ζ_1 and the θ function is

$$\begin{aligned} \theta(x) &= 1 \quad x \geq 0 \\ &= 0 \quad x < 0 \end{aligned} \qquad (3)$$

The transmission probability of any neutron impinging with an angle γ with respect to the collimator axis is obtained by integrating the contribution from all virtual sources P on P'P"

$$\begin{aligned} \text{i.e. } T(\gamma) &= \int_o^{\Gamma} T(\gamma,\zeta_1)\,d\zeta_1 \\ &= \int_o^{\Gamma} \theta(\zeta_1-\gamma)\,\theta(\gamma+\overset{\Gamma}{\phi}-\zeta_1)\,d\zeta_1 \\ &= \int_o^{|\gamma|} \theta(\zeta_1-\gamma)\,\theta(\gamma+\overset{\Gamma}{\phi}-\zeta_1)\,d\zeta_1 \\ &\quad + \int_{|\gamma|}^{\Gamma} \theta(\zeta_1-\gamma)\,\theta(\gamma+\overset{\Gamma}{\phi}-\zeta_1)\,d\zeta_1 \\ &= \int_{|\gamma|}^{\Gamma} \theta(\gamma+\overset{\Gamma}{\phi}-\zeta_1)\,d\zeta_1 \\ &= \Gamma\left(1-\frac{|\gamma|}{\Gamma}\right) \qquad |\gamma| < \Gamma \end{aligned} \qquad (4)$$

From this expression for the transmission probability of a neutron making an angle γ with the collimator axis, we recognize the triangular function that we could have guessed on intuitive grounds. The assumption of an incident flux which is isotropic in the small angular range of interest means that the integral of equation (4) over γ must be linear in Γ. This normalization requirement means that equation (4) becomes simply

$$T(\gamma) = 1 - \frac{|\gamma|}{\Gamma} \tag{4a}$$

Neutrons transmitted with a probability of one half that of the maximum are those making an angle $\pm\frac{\Gamma}{2}$ with respect to the axis. The full width at half height is thus equal to Γ in the case of a purely triangular transmissivity.

II-1-iii Effect of small angle scattering. Geometrical considerations have shown that a Soller slit collimator would have a triangular transmission function if the channel walls were perfectly absorbing and at the same time the small angle reflection was inexistant.

We now proceed to show how much the second of those two processes contributes in the departure from the ideal case considered above. The angle defining critical reflection at a neutron wavelength λ, i.e. the critical angle, is expressed as

$$\phi^{(\lambda)}_{crit} = \lambda \sum_i \left(\frac{N_i \; b_{coh_i}}{\pi}\right)^{1/2} \tag{5}$$

where N_i is the number of scattering centers of index i per unit volume and b_{coh_i} is the coherent scattering length.

A suggested reference on this subject is Gurevich [68].

In the thermal neutron range, we see that ϕ_{crit} is a linear function of λ; in other words the effect of critical angle scattering on the effective characteristics of a collimator should be more important at the lower energies of the spectrum. From a practical point of view, it means that for all other things being held constant, the incident beam collimator has an energy dependence and that the scattered beam collimation "looks" differently depending on whether the scattering process was that of neutron energy loss or neutron energy gain.

How big is this effect? Table II-1-iii-1 lists a set of values of ϕ_c for steel using

$$N = 8.49 \times 10^{22}\ \mathrm{cm}^{-3}$$

$$b = 0.96 \times 10^{-12}\ \mathrm{cm} \qquad \text{(Bacon [62])}$$

and for cadmium using

$$N = 4.635 \times 10^{22}\ \mathrm{cm}^{-3}$$

$$b = (0.38 + i\ 0.12)\ 10^{-12}\ \mathrm{cm} \qquad \text{(Bacon [62])}$$

This last case concerns the cadmium-plated steel plates which are used in our collimators. Then for steel $\phi_c(\mathrm{min}) = 5.55\lambda(\mathrm{A})$ (6a)

$$= \frac{24.6}{\sqrt{\nu(\mathrm{THz})}} \qquad (6b)$$

and for cadmium, the values are 0.4645 of the corresponding values for steel (using the real part of the scattering length).

Table II-1-iii-1

Maximum angle for total small angle reflection

ν(THz)	ϕ_c minutes (steel)	ϕ_c minutes (cadmium)
1.0	24.6	11.4
2.0	17.4	8.08
4.0	12.3	5.7
8.0	8.7	4.04
16.0	6.15	2.9

One now has to modify the previous conclusions regarding the transmission function of a collimator being given by a triangular function. Assuming that a neutron incident on a surface with an angle greater than ϕ_c has a unit probability of being absorbed while it has the same probability of being reflected if its incidence angle is less than ϕ_c, one expects that the transmission function should remain unaffected for incidence angle greater than ϕ_c. On the other hand, any neutron making an angle less than ϕ_c with the collimator axis should be transmitted after possible multiple scattering on the collimator walls resulting in a saturation effect for the angular region between $-\phi_c$ and $+\phi_c$.

Fig.II-1-iii-1 Relative effect of small angle scattering on collimation; intensity vs. deviation.

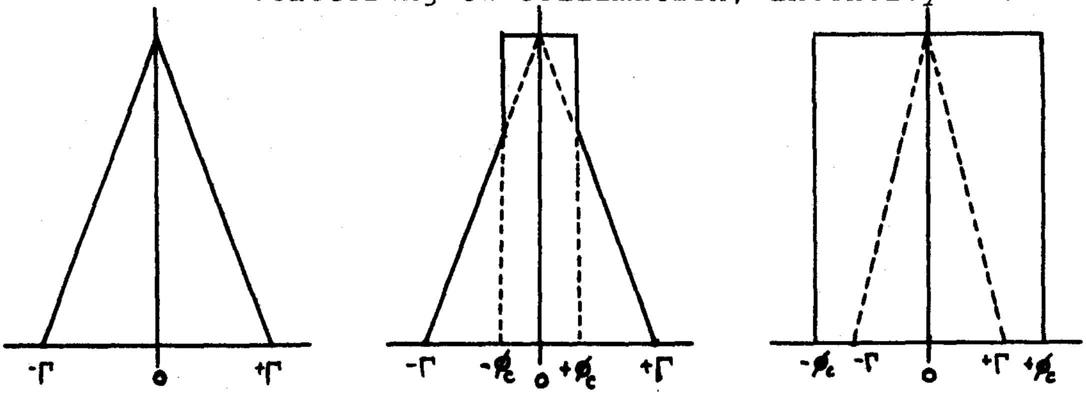

a) $\phi_c=0$ b) $\phi_c<\Gamma$ c) $\phi_c>\Gamma$

Fig. II-iii-i illustrates the different possible transmission functions for collimators. In case a), the phenomena of mirror reflection is not considered and the transmission function is triangular, as deduced in the previous section. In b) and c), the phenomena of mirror reflection is considered. In b), the collimation angle is larger than the value of the angle for critical scattering resulting in a transmission probability equal to unity (saturation) in the central region, while the tail portion still shows the triangular behaviour. Case c) represents the extreme case where $\phi_c > \Gamma$; in this case, the collimation angle is independant of the value of the characteristic angle of the collimator and is given by the value of the critical angle ϕ_c. The transmission probability is equal to unity in the range $\pm\phi_c$. Thus, the triangular function becomes less suitable to characterize a collimator in the case of tight collimation and/or low neutron energy.

iv) Experimental results

Measurements were made to obtain experimentally the transmission function of a Soller-slit collimator. The experimental procedure consisted in rocking the collimator under testing in the monochromatic incident beam with the analyser set in the straight through position.

Obviously, in this way, it is not possible to isolate directly the collimator characteristic function. What is measured instead is a convolution of the incident beam collimator function, the monochromator mosaic distribution and the transmission function of the collimator under testing. If all three functions were gaussian, the resulting convoluted function would also be gaussian with a width given by

$$\sigma = \sum_{i=1,3} \sigma_i^2 \qquad (7)$$

σ_i being the true width contributed by each of the components.

Figure II-1-iv-1 shows the results with two combinations of the most commonly used collimators, namely $\Gamma = 1/80$ (43') and $\Gamma = 1/160$ (21.5'). The point to observe is the fact that the composite transmission function has a very nearly gaussian shape. The values of the effective half-height, that is after correction for the background, can be used to determine the standard deviation σ of the intensity distribution. The continuous line in this figure represents the calculated gaussian curve using this value of σ.

The values of the collimation angles and neutron energies used in these measurements correspond to case b) in figure II-1-iii-1 since table II-1-iii-1 gives an angle of 6 minutes as the critical angle on cadmium for neutrons having a frequency of 3.5 THz.

Thus there is overall agreement with experiment both in terms of the composite width and the intensity distribution if the transmission function of the collimators is assumed to be gaussian. The resulting simplification coming from the use of such a well-behaved function will be vital in obtaining an analytical expression for the resolution matrix and the line shape (sections II-3 and 4). For this reason, the relevance of the gaussian approximation applied to collimators will not be further questioned and the validity of this assumption is left to be verified with actual phonon measurements.

We have seen before that the characteristic angle of a collimator is equal to the FWHM (Γ) in the case of a triangular function. In the case of interest of a gaussian function, the standard deviation of $\exp(-\frac{1}{2}\frac{x^2}{\sigma^2})$ obtained by matching the widths at half height is given by:

$$\sigma = \frac{\Gamma}{2(2\ \ln 2)^{1/2}} = \Gamma/2.354 \ ; \quad \Gamma = d/L \qquad (8)$$

Fig. II-1-iv-1

Experimental determination of the transmission function of a Soller-slit collimator

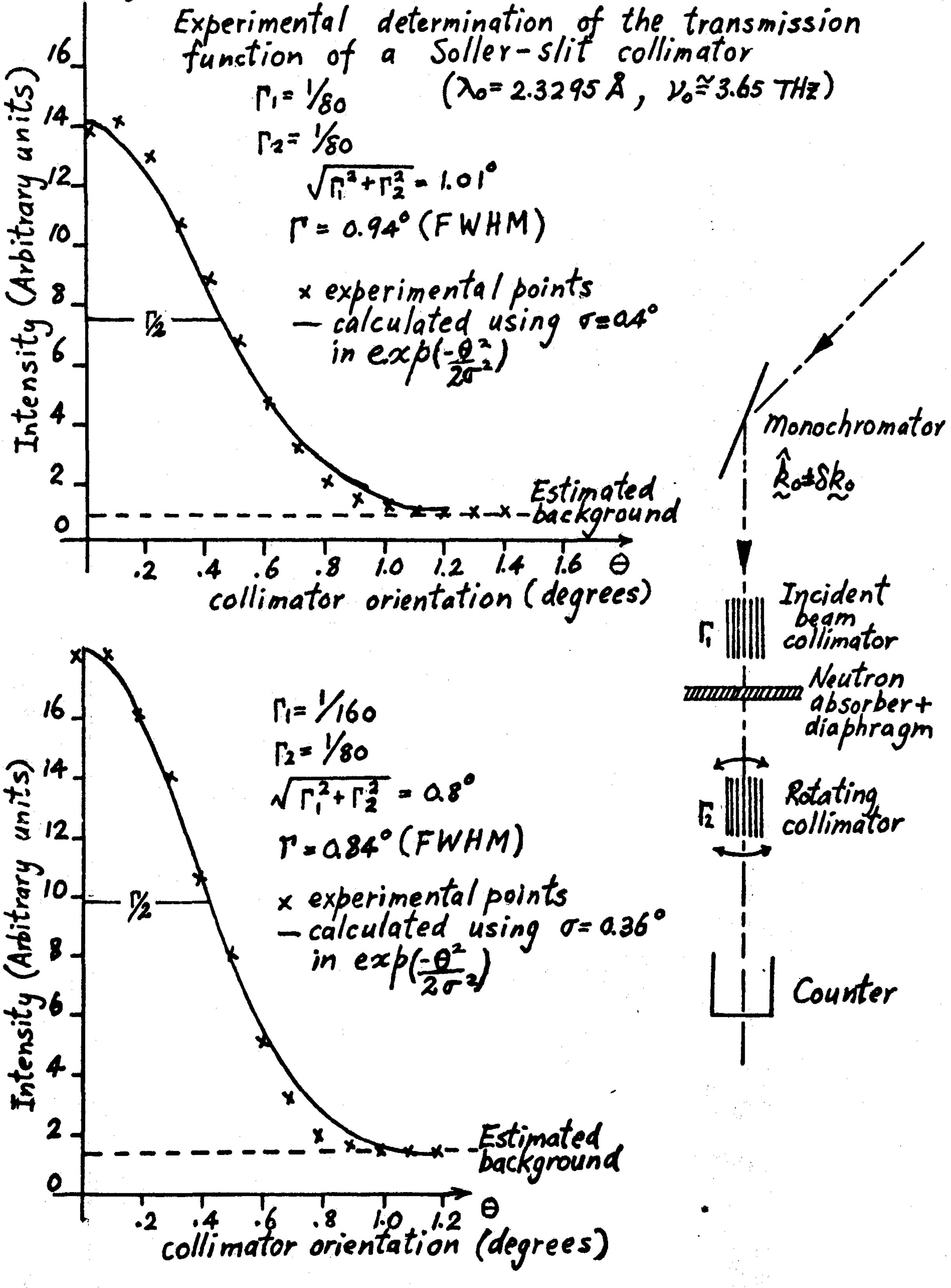

II-2 Elastic coherent scattering of neutrons from a monocrystal.

It is the purpose of this section to show how the effects of imperfect collimation, mosaic distribution and crystal inhomogeneities affect the angular distribution and monochromatization of neutrons Bragg-scattered from a monocrystal. Each of these factors will be considered individually before considering the composite effect.

i) Elastic coherent scattering from a set of planes having Miller indices (hkl) is governed by the Bragg equation which may be written as

$$k = \frac{\pi}{d_{hkl}\sin(\theta_s)} \qquad (1)$$

or equivalently

$$\underset{\sim}{k}\cdot\underset{\sim}{n} = \pi/d_{hkl} \qquad (2)$$

where $2\theta_s$ is the scattering angle

and $\underset{\sim}{n}$ is a unit vector perpendicular to the scattering planes.

Writing the Bragg equation in this way affords an interesting geometrical interpretation. For a given plane spacing, the product $\underset{\sim}{k}\cdot\underset{\sim}{n}$ is a constant; that is the projection of the wave vector obeying Bragg equation on the unit vector $\underset{\sim}{n}$ is independent of the scattering angle for a given (hkl) reflection. A moment reflection shows that this is simply another formulation of the condition that the momentum transfer $\underset{\sim}{Q}$ be equal to a reciprocal lattice vector, since $\|\underset{\sim}{k}_0\| = \|\underset{\sim}{k}'\|$

and $\|\underset{\sim}{Q}/2\| = \|\underset{\sim}{k}_o - \underset{\sim}{k}'\|/2 = \|\underset{\sim}{k}_o\| \sin(\theta_s) = \pi/d_{hkl}$ (3)
(see fig. II-2-i-1)

In fig. II-2-i-2, the different lines labelled with Miller indices correspond to the loci of allowed wave vectors for different reflections off a copper crystal. In practice, the scattering angle may be physically limited to a given range and therefore determines the maximum and minimum values of the wave vector that can undergo scattering through a given momentum-transfer. The limiting values in the case of the monochromator and analyser on E-2 hole are included in the figure.
In practice, the (220) reflection is used for the monochromator and the (200) for the analyser. This is justified in section III-5.

ii) Effect of collimation

Because of imperfect collimation, the neutrons incident on a crystal do not have a perfectly defined direction of propagation. The same thing may be said about neutrons reflected from the crystal. This double uncertainty results in a corresponding uncertainty in the value of the scattering angle.

To illustrate the effect of imperfect collimation, we assume a perfect crystal as illustrated in fig. II-2-ii-1.
Let the deviations with respect to the main directions of propagation be γ_1 and γ_2 in the case of the incident and scattered beam respectively. Since the crystal is supposed to be perfect, then Bragg condition requires that $\gamma_1 = \gamma_2$. The scattering angle is thus changed from $2\theta_s$ to $2\theta_s + 2\gamma_1$. The wave vector corres-

FIG. II-2-i-1

GEOMETRICAL INTERPRETATION OF BRAGG RELATION

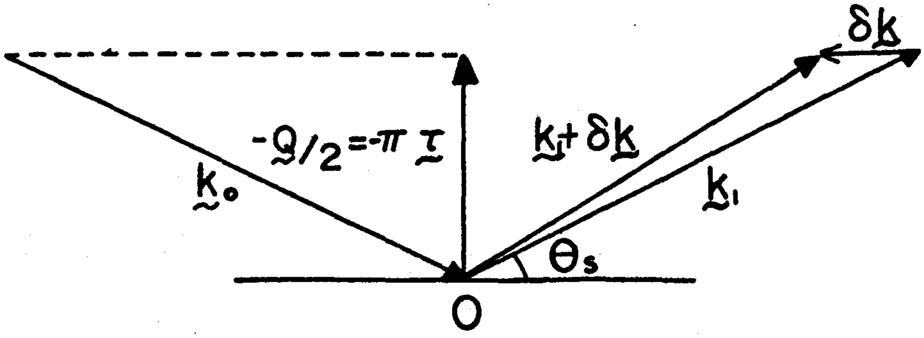

FIG. II-2-i-2

LOCI OF ALLOWED WAVE VECTORS ($ƙ = 1/\lambda$ A^{-1}) FOR SCATTERING OFF Cu CRYSTALS

(a=3.6147 Å)

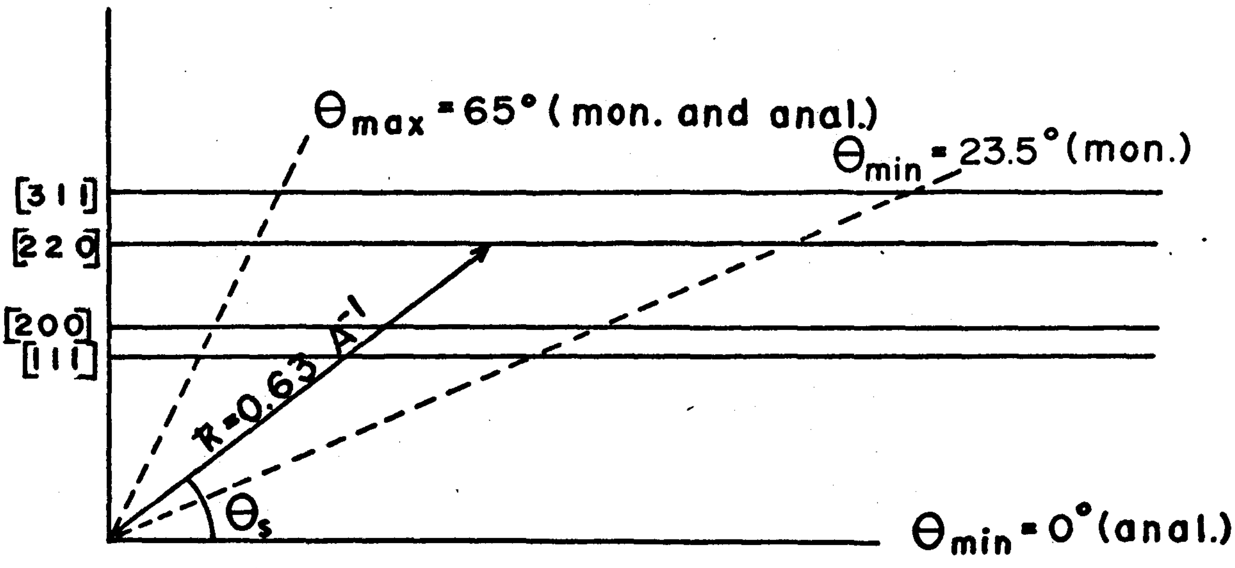

SCALE FOR WAVE VECTOR (ƙ) : 1cm = 0.1 A^{-1}

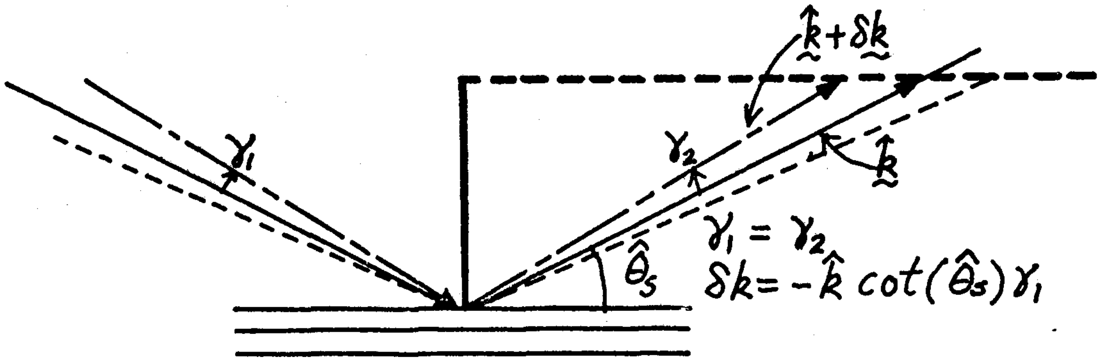

FIG. II-2-ii-1 EFFECT OF IMPERFECT COLLIMATION

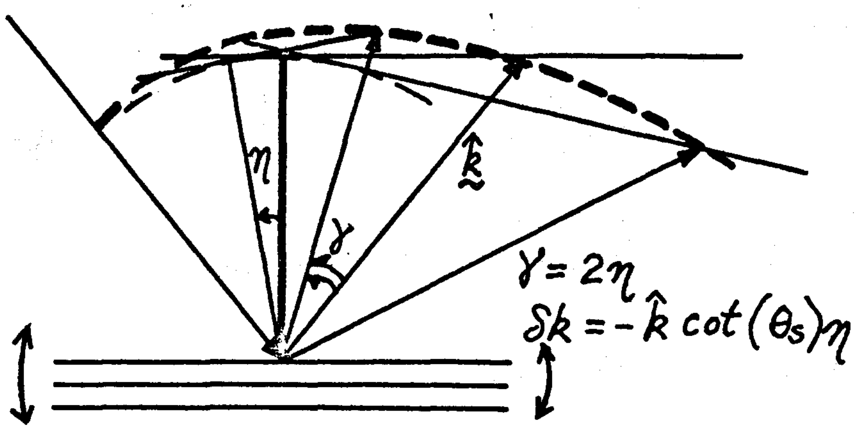

FIG. II-2-iii-1 EFFECT OF MOSAIC SPREAD

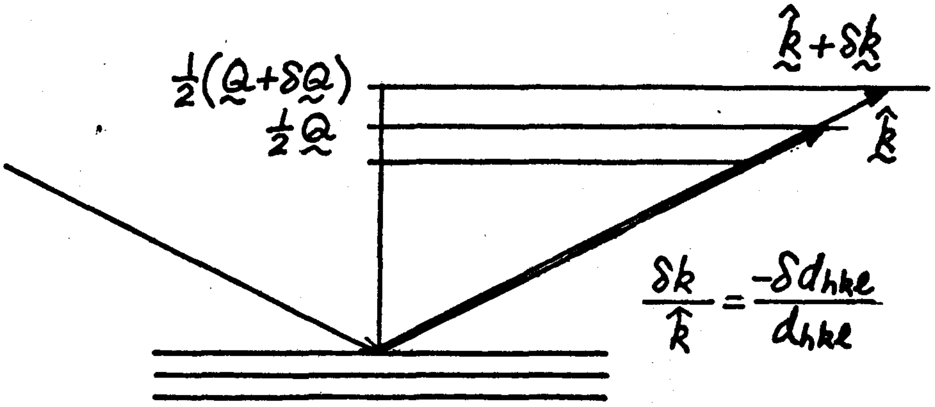

FIG. II-2-iv-1 EFFECT OF CRYSTAL INHOMOGENEITIES ponding to this scattering angle is then

$$k = \frac{\pi}{d_{hkl}\sin(\theta_s+\gamma_1)} \tag{4}$$

Since the usual collimation is such that γ_1 and γ_2 are much smaller than unity, we can write

$$\delta k = -\,\hat{k}\cot(\hat{\theta}_s)\,\delta\theta_s \tag{5}$$

which is obtained by differentiating (1). Thus,

$$\hat{k} + \delta k = \hat{k}\,\left(1 - \gamma_1 \cot(\hat{\theta}_s)\,\right) \tag{6}$$

If the equation II-2-i-(2) had been differentiated instead, the result would have been

$$0 = \delta \underset{\sim}{k}\bullet\underset{\sim}{n} \tag{7}$$

thus indicating that the vectors $\delta\underset{\sim}{k}$ and $\underset{\sim}{n}$ are perpendicular, in conformity with the diagram in fig. II-2-i-1. The correlation between the scattered wave vector and the deviation with respect to the main direction of propagation is an equivalent formulation of the Bragg equation.

Since it was assumed that the crystal is perfect, the probability of occurence of such a process is really determined by the transmission probabilities of the incident and scattered beams through their respective collimators. From the considerations of subsection II-1-iv, the transmission probability may be written

$$\pi(\tilde{k},\gamma) = \exp\left(\frac{-1\gamma^2}{2\alpha^2}\right)\,\delta\left((\underset{\sim}{\tilde{k}}-\underset{\sim}{\hat{k}})\bullet\underset{\sim}{n}\right) \tag{8a}$$

or equivalently

$$= \exp\left(-\frac{1\gamma^2}{2\alpha^2}\right)\,\delta\left(\hat{k}(1-\gamma\cot(\hat{\theta}_s)) - \tilde{k}\right) \tag{8b}$$

where α is the effective composite collimation defined by

$$1/\alpha^2 = 1/\alpha_1^2 + 1/\alpha_2^2 \tag{9a}$$

and

$$\gamma = \gamma_1 = \gamma_2 \tag{9b}$$

iii) Effect of the mosaic structure of the reflecting crystal.

The perfect crystal considered above is an idealization. It is known that no crystal is perfect up to the macroscopic level [appendix A-3] but rather is made up of micro-crystallites which are themselves perfect and which are distributed preferentially along the average crystal orientation. Denote the crystallite distribution function as $W(\eta)$; it gives the density of crystallites oriented at an angle η with respect to the average orientation. In many cases, a gaussian function proves to be a suitable approximation for $W(\eta)$; this is what will be adopted here. Note that if the mosaic blocks are distributed with a cylindrical symmetry along the main orientation, then the function $W(\eta)$ is actually a function of two variables,

$$W(\eta_x, \eta_y) = \frac{1}{2\pi \; \sigma_x \sigma_y} \exp\left(\frac{-1}{2}\frac{\eta_x^2}{\sigma_x^2}\right) \times \exp\left(\frac{-1}{2}\frac{\eta_y^2}{\sigma_y^2}\right) \qquad (10)$$

If we arbitrarily choose the x and y axis such that the x axis lies in the scattering plane while the y axis is perpendicular to this plane, we expect that the y component will be unimportant if the vertical collimation is much relaxed compared with the standard deviation of the crystallites. In practice, such is the case and the crystallite distribution is effectively given by a one-dimensionnal gaussian function of the form

$$W(\eta) = W(\eta_x) = \int_{-\infty}^{\infty} W(\eta_x, \eta_y)\,dy = \frac{1}{\sqrt{2\pi}\,\sigma_x} \exp\left(-\frac{1}{2}\frac{\eta_x^2}{\sigma_x^2}\right) \qquad (11)$$

Fig. II-2-iii-1 illustrates the effects of mosaic spread on the monochromatization of scattered neutrons. The projection of the scattered wave vector on the normal to the scattering plane has to be constant, as was already said. Since this normal is not uniquely defined because of the mosaic structure, the loci of points in reciprocal space are smeared out on a curve with a probability density given by $W(\eta)$. It should then be self-evident from fig. II-2-iii-1 how this curve determines the possible scattered vectors.

For each of the crystallites orientations, the value of the scattered wave vectors obey the Bragg equation for each of the different scattering angles $(2\theta_s + \gamma)$. If the incident beam is assumed perfectly collimated and polychromatic, the scattering angle is related to the crystallite orientation through the relation: $\eta = \gamma/2$. Thus the intensity of the scattered beam in the direction $(2\theta_s + \gamma)$ is proportionnal to $W(\gamma/2)$, the density of crystallites properly oriented to produce scattering in this direction.

Eq. II-2-(5) which gives the change in magnitude of the scattered wave vector as a result of a change of $2\delta\theta_s$ in the scattering angle thus reads in this case:

$$\|\delta \underset{\sim}{k}\| = -\|\hat{\underset{\sim}{k}}\| \cot(\hat{\theta}_s)\, \eta \qquad (12)$$

since
$$2\delta\theta_s = \gamma = 2\eta$$

Similarly as in the previous section we can define the distribution of scattered neutrons by

$$\pi(\tilde{k},\gamma) = \frac{1}{\sqrt{2\pi}\,\sigma} \exp\left\{-\frac{1}{2}(\gamma^2/(4\sigma^2 + \alpha_2^2)\right\} \delta(\hat{k}(1 - \frac{\gamma}{2}\cot(\Theta_s) - \tilde{k}) \qquad (13)$$

where the two terms in the exponential describe respectively the mosaic distribution and the transmission of the collimator in the scattered beam.

iv) Effect of the presence of inhomogeneities in the scattering crystal.

The presence of inhomogeneities in a crystal results in a variation of the lattice parameter which in turn affects the distribution of neutrons scattered from such a crystal. In practice crystal chosen as monochromator or analyser are an homogeneous substance and these considerations do not apply. However this effect is mentioned for the sake of completeness.

Consider again the Bragg equation II-2-(1) . Taking the partial derivative with respect to d_{hkl} yields:

$$\delta k / k = -\delta d_{hkl}/d_{hkl} \qquad (14)$$

The negative sign expresses the fact that distances in reciprocal space are inversely related to those in real space and an increase in the value of the plane spacing by the amount δd_{hkl} results in a contraction of distances in reciprocal space by the relative quantity $|\delta d_{hkl}| / d_{hkl}$.

Thus the projection of the scattered wave vector on the normal to the scattering plane varies throughout the crystal (fig. II-2-iv-1) resulting in a correlation k-γ such that the intensity distribution is zero for any deviation angle γ from the central direction of the scattered beam.

that is to say that the wave vector $\delta\underset{\sim}{k}$ is parallel to $\underset{\sim}{k}$ so that $\underset{\sim}{k} + \delta\underset{\sim}{k}$ is also parallel to $\underset{\sim}{k}$.

The analog of equations (8) and (13) for the intensity distribution of the scattered neutrons is in this case

$$\pi(\tilde{k},\gamma) = W(d_{hkl})\ \delta(\gamma) \tag{15}$$

$W(d_{hkl})$ being the distribution of plane spacings and d_{hkl} being equal to $\pi/(\underset{\sim}{\tilde{k}}\cdot\underset{\sim}{n})$.

The simple argument of the delta function reflects the fact that $\delta\underset{\sim}{k}$ is parallel to $\underset{\sim}{k}$.

The situation of an inhomogeneous crystal will not be further considered since this situation was not encountered in practice; even the ternary alloy used in the measurement of phonons showed remarkable homogeneity.

v) Composite effect of imperfect collimation and mosaic structure of the scattering crystal.

The three cases previously considered dealt with the contribution of a single factor to the distribution of scattered neutrons and these idealized cases resulted in the magnitude of the scattered wave vector being correlated with the deviation from the average scattering angle; this is reflected by the presence of the delta function in the three equations for the intensity distribution (equations (8), (13) and (15)).

We now will calculate this same intensity distribution but taking into account the simultaneous effect of mosaic structure and of imperfect collimation in both the incident and scattered beam. The crystal is assumed to be homogeneous (cf. section II-2-iv). Physical intuition predicts that the superposition of these two factors (cf. fig. II-2-ii-1 and II-2-iii-1) would remove the delta function from the expression for the intensity distribution resulting in this function being a well behaved continuous function of two variables.

For the time being, no assumption will be made about the transmission function of the i^{th} collimator ($T_i(\gamma_i)$) or the mosaic distribution of the specimen ($W(\eta)$). We restrict ourselves to angles coplanar with the scattering plane.

What is the probability of having a neutron of wave vector $\hat{k}+\delta k$ scattered in the direction γ_2 relative to the central direction of the scattered beam? (γ_2 is positive for angles measured toward the unit vector $\underset{\sim}{n}$; see Fig. II-2-v-1). Assuming that the propagation of a neutron through the individual steps of the transmission through the incident beam collimator (i=1), the scattering by properly oriented mosaic blocks and the transmission through the scattered beam collimator (i=2) correspond to statistically independent processes, the composite probability is given as the product of the individual probabilities, i.e.

$$\pi(\hat{k},\delta k,\gamma_2) = T_1(\gamma_1)W(\eta)T_2(\gamma_2) \tag{16}$$

where the angles γ_1, η and γ_2 are coupled with each other and with δk; they have to satisfy indentities which are now derived.

The value of the wave vector $\hat{k}+\delta k$ defines the corresponding Bragg angle θ_S and allows us to calculate η and γ_1. Fig. II-2-v-1 illustrates the relation between the different angles. The results of interest are:

$$\eta = \gamma_2 - \delta\theta \tag{17a}$$

$$\gamma_1 = \gamma_2 - 2\delta\theta \tag{17b}$$

Hence we may write equation (1) as

$$\Pi(\hat{k},\delta k,\gamma_2) = T_1(\gamma_2-2\delta\theta)W(\gamma_2-\delta\theta)T_2(\gamma_2) \tag{18}$$

where

$$\delta\theta = \frac{-\delta k}{\hat{k}} \tan\hat{\theta} \tag{5}$$

Hence the composite probability function is a function of two independant variables for a given value of the central wave vector $\hat{k}$.

In order to proceed any further, we have to make some assumptions on the nature of the functions $T_i(\gamma_i)$ and $W(\eta)$. It is physically plausible and it will be mathematically convenient in the calculation of a phonon line shape in II-4 to assume a normalized Gaussian function for $W(\eta)$, i.e.

$$W(\eta) = \frac{1}{\sqrt{2\pi}\sigma} \exp\left[-\frac{1}{2}\left(\frac{\eta}{\sigma}\right)^2\right] \tag{19}$$

A study of the more general case where the standard deviation is itself a variable has been performed by Dymond [70] for the case of elastic scattering but it will **not be considered here.**

The analytic form of the transmission function should properly be chosen as a triangular function with a flat central region to take into account critical scattering (sub-section II-1-iii), i.e. $T_i(\gamma_i) = \theta(|\gamma_i|-\phi_c)\theta(\alpha_i-|\gamma_i|)(\alpha_i-|\gamma_i|)+\theta(\phi_c-|\gamma_i|)$ (20)

where we have used the previously defined θ function (equation II-1-(3) and ϕ_c is defined by equation II-1-(5). However, this is mathematically difficult to handle and, for the reason already mentioned we adopt the approximation of a Gaussian transmission function for the collimators, i.e.

$$T_i(\gamma_i) = \exp(-\tfrac{1}{2}\gamma_i^2/\alpha_i^2) \qquad (21)$$

Hence the final expression for equation (18) is

$$\pi(\hat{k},\delta k,\gamma_2) = \frac{1}{\sqrt{2\pi}\sigma}\exp(-\tfrac{1}{2}\Sigma^2) \qquad (22)$$

where $$\Sigma^2 = (\gamma_2+2\frac{\delta k}{\hat{k}}\tan\hat{\theta})^2/\alpha_1^2+\gamma_2^2/\alpha_2^2 + (\gamma_2+\frac{\delta k}{\hat{k}}\tan\hat{\theta})^2/\sigma^2 \qquad (23a)$$

$$= \Sigma_1\gamma_2^2 + \Sigma_2\gamma_2(\delta k)+\Sigma_3(\delta k)^2 \qquad (23b)$$

$\Sigma_1,\Sigma_2,\Sigma_3$ being defined as

$$\Sigma_1 = \frac{1}{\alpha_1^2} + \frac{1}{\alpha_2^2} + \frac{1}{\sigma^2} \qquad (24a)$$

$$\Sigma_2 = \frac{2\tan\hat{\theta}}{\hat{k}}\left(\frac{2}{\alpha_1^2} + \frac{1}{\sigma^2}\right) \qquad (24b)$$

$$\Sigma_3 = \frac{\tan^2\hat{\theta}}{\hat{k}^2}\left(\frac{4}{\alpha_1^2} + \frac{1}{\sigma^2}\right) \qquad (24c)$$

Equation (23b) is the equation of an ellipse centred on the origin and rotated with respect to the $(\delta k,\gamma_2)$ axes and it governs the behaviour of the two dimensional Gaussian composite probability as a function of the two variables γ_2 and δk. For a given value of γ_2, the intensity distribution in terms of δk has a Gaussian structure centred around the value

$$\delta k = \frac{-\Sigma_2\gamma_2}{2\Sigma_3} \qquad (25a)$$

Similarly, if δk is a constant, the maximum occurs at

$$\gamma_2 = \frac{-(\delta k)\Sigma_2}{2\Sigma_1} \qquad (25b)$$

the set of $(\delta k, \gamma_2)$ points such that Σ^2 is a constant defined as isoprobability contour in k-space. This contour may be obtained by solving the quadratic (23b) or alternatively by joining points of equal probability on the set of functions of one variable (either δk or γ_2) for different values of the other variable as illustrated in figure II-2-v-2 depicting the situation of a Cu(200) at a neutron energy of 2Thz with collimation and mosaic parameters corresponding to those found in the analyser. Observe that the low energy end of the ellipse is closest to the normal of the scattering planes, as expected. It was verified that calculations according to equation (20) or (21) give essentially the same result.

The total intensity scattered in a given direction is obtained by integrating equation (22) over all possible wave vectors

$$I(\hat{k}, \gamma_2) = \int_0^\infty \pi(\hat{k}, \delta k, \gamma_2)\, d(\delta k) \qquad (26)$$

In the small range where the integrant is large, we assume that the Maxwell spectrum is constant. Using the result of part i) of appendix A-1, this gives

$$I(\hat{k}, \gamma_2) = \frac{1}{2\sigma\sqrt{\Sigma_3}} \exp\left\{-\frac{1}{2}\left(\Sigma_1 - \frac{\Sigma_2^2}{4\Sigma_3}\right)\gamma_2^2\right\} \qquad (27)$$

we have neglected the term

$$\mathrm{erf}\left(\frac{\Sigma_2 \gamma_2^2}{2\sqrt{\Sigma_3}}\right)$$

because of the small angle approximation. Note that the result of the integration gives a Gaussian intensity distribution as a function of angular displacement away from the central direction of propagation of the scattered beam.

The total intensity is obtained by integrating (26) over all angles in the scattering plane

$$I_{tot}(\hat{k}) = \int_{-\infty}^{\infty} d\gamma_2 \; I(\hat{k},\gamma_2) \tag{28}$$

where the physical limits $(-\pi,\pi)$ were replaced by the convenient ones $(-\infty,\infty)$. Again using the result of part i of appendix A-1, we get

$$I_{tot}(k) = \frac{\sqrt{2\pi}}{\sigma\sqrt{4\Sigma_1\Sigma_3-\Sigma_2^2}} \tag{29a}$$

$$= \frac{\alpha_1\alpha_2 \;(\pi)^{3/2}}{\sin\hat{\theta}\tan\hat{\theta}d_{hkl}\sqrt{2(4\sigma^2+\alpha_1^2+\alpha_2^2)}} \tag{29b}$$

This result should not be used to obtain the effect of variation of crystal mosaic spread (σ) on the scattered intensity since no considerations were made of extinction (appendix A-3) It however illustrates the dependence of the total intensity upon collimation angles.

GEOMETRY OF SCATTERING FROM A MONO-CRYSTAL

$$\zeta_1 = \frac{\pi}{2} - \theta = \frac{\pi}{2} - \hat{\theta} + \eta - \gamma_2 \qquad \eta = \hat{\theta} + \gamma_2 - \theta$$

$$\zeta_2 = \zeta_1 + \eta = \frac{\pi}{2} - \hat{\theta} + 2\eta - \gamma_2$$

$$\gamma_1 = \zeta_2 - \left(\frac{\pi}{2} - \hat{\theta}\right) = 2\eta - \gamma_2$$

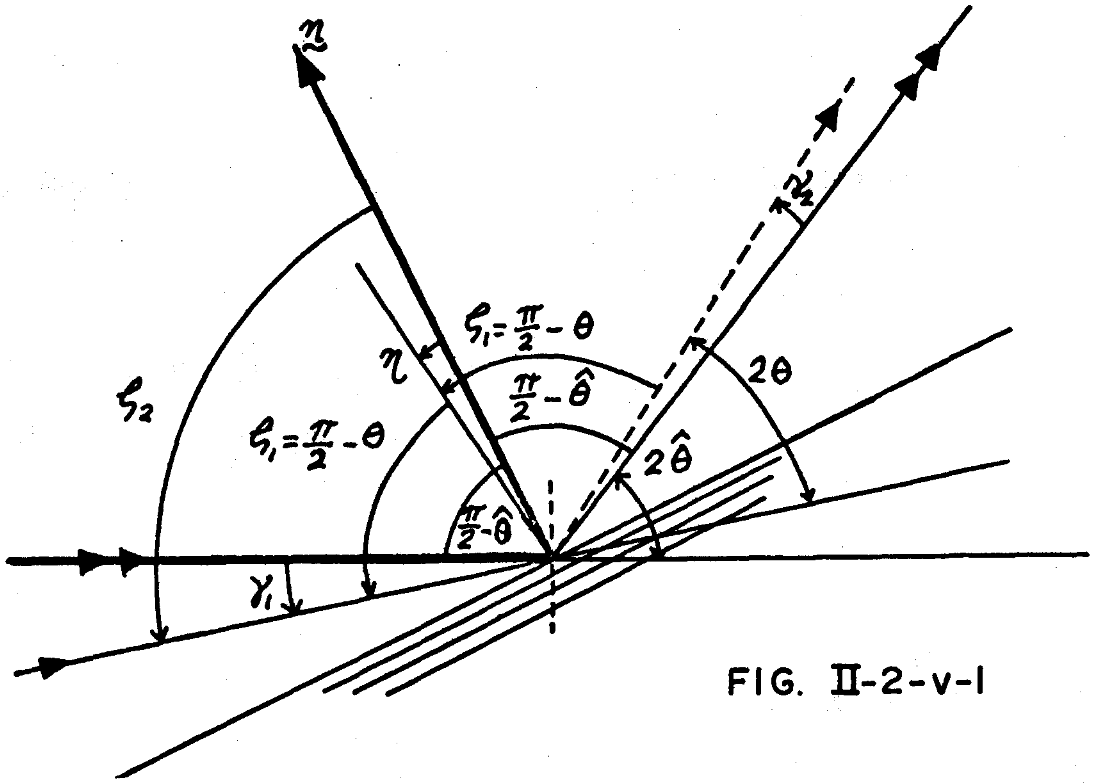

FIG. II-2-v-1

Legend: $\underset{\sim}{n}$, unit vector defining the centre of the crystallite distribution

γ_i, deviation relative to the central directions

$\hat{\theta}$, central Bragg angle

θ, Bragg angle for a non-central process

η, deviation of a mosaic block relative to $\underset{\sim}{n}$.

1/e isoprobability contour for the scattering of neutrons of average energy $\hat{\nu} = 2$ THz on a Cu(200) crystal

Fig. II-2-V-2

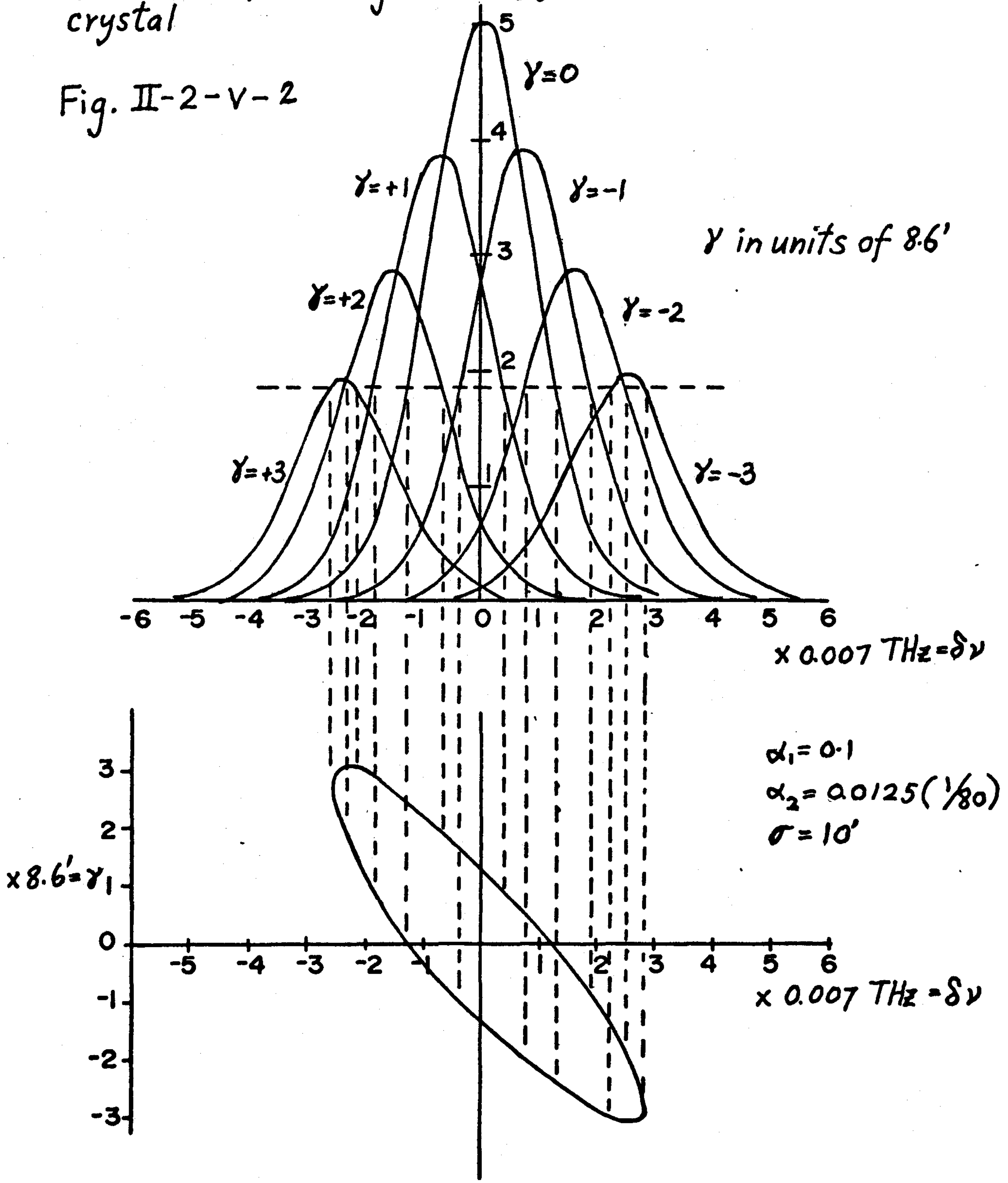

II-3 Derivation of the instrumental resolution function.

We now proceed to derive an analytic expression for the resolution function of a neutron spectrometer. Altought the mathematical derivation may make this part a bit painful to read, we will try as much as possible to keep in close touch with the corresponding physical reality. The necessary and plausible approximations will be well indicated as well as being justified. In fact, this section which deals with the instrumental resolution itself, i.e. independently of the characteristics of a particular specimen, is quite exact. This is because of the fact that the components of a spectrometer are characterized by angular parameters such that the small angle approximation is valid. On the other hand, the next section which deals with the contribution to the resolution function from the specimen being studied is of a much more restricted scope; it will define the limit of validity of the theory. The approach adopted here follows that of the classic paper by Cooper/Nathans [67].

The natural variables being the momentum transfer $\hbar\underset{\sim}{Q}$ and the energy transfer $\hbar\omega$, we proceed to define an object giving the probability of detection of a neutron having gone through a $(\underset{\sim}{\tilde{Q}},\tilde{\omega})$ scattering process while the instrument is set for looking at the point $(\underset{\sim}{\hat{Q}},\hat{\omega})$ in $(\underset{\sim}{Q},\omega)$ space; this object is the resolution function $R(\hat{\underset{\sim}{Q}}+\Delta\underset{\sim}{Q},\hat{\omega}+\Delta\omega)$ of the instrument. In other words, it give the relative probability that a neutron recorded in the detector went through a $(\hat{\underset{\sim}{Q}}+\Delta\underset{\sim}{Q},\hat{\omega}+\Delta\omega)$ process. Ideally, the resolution should be a delta function in the $\underset{\sim}{Q}$ and ω variables, but the existence of non-zero mosaic spreads in the monochromating and analysing crystals as well as the imperfect collimation resulting from the requirements of intensity, result in the resolution function having a non-zero window width in both the $\underset{\sim}{Q}$ and ω variables.

i) Derivation of the resolution matrix.

This section is fairly general. No assumptions are needed about the type of scattering or about the response of the specimen to a $(\underset{\sim}{Q},\omega)$ probe. Consider a certain spectrometer setting:

$$\hat{\underset{\sim}{Q}} = \hat{\underset{\sim}{k}}_m - \hat{\underset{\sim}{k}}_a \qquad (1)$$

$$\hbar\hat{\omega} = \frac{\hbar^2}{2M}(\hat{\underset{\sim}{k}}_m^2 - \hat{\underset{\sim}{k}}_a^2) \qquad (2)$$

as illustrated by the vector diagram of fig. II-3-i-1.

Here $\hat{\underset{\sim}{k}}_m$ and $\hat{\underset{\sim}{k}}_a$ are the most probable neutron wave vectors being scattered from the monochromator and analyser respectively. Their magnitudes determine the energy transfer, as given in (2), and both their magnitudes and relative directions of propagation determine the the momentum transfer, as given in (1). This means that an uncertainty in the magnitude of either the incident or scattered wave vectors results in an uncertainty in the momentum as well as the

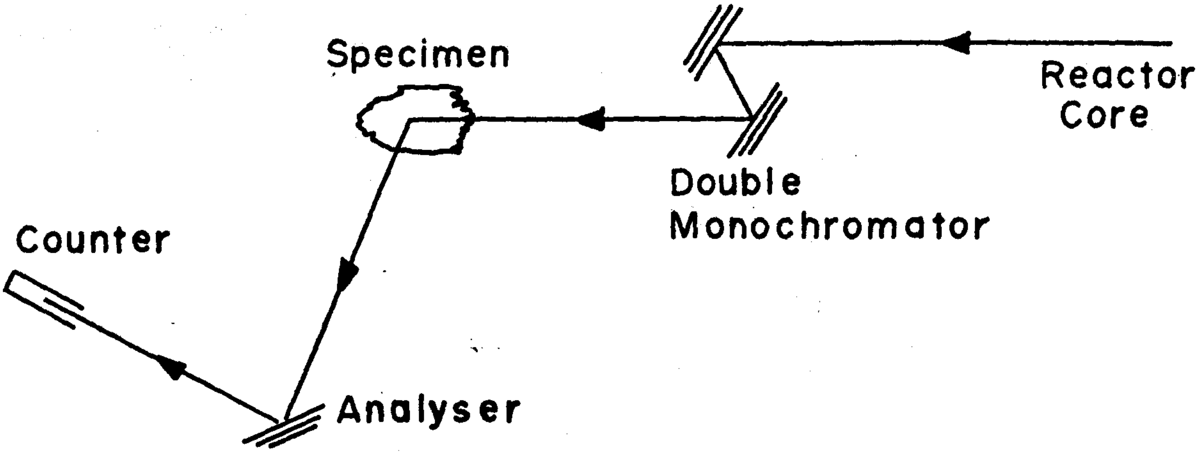

NEUTRON PATH IN X-SPACE (BOTTOM VIEW)

VECTOR DIAGRAM IN K-SPACE

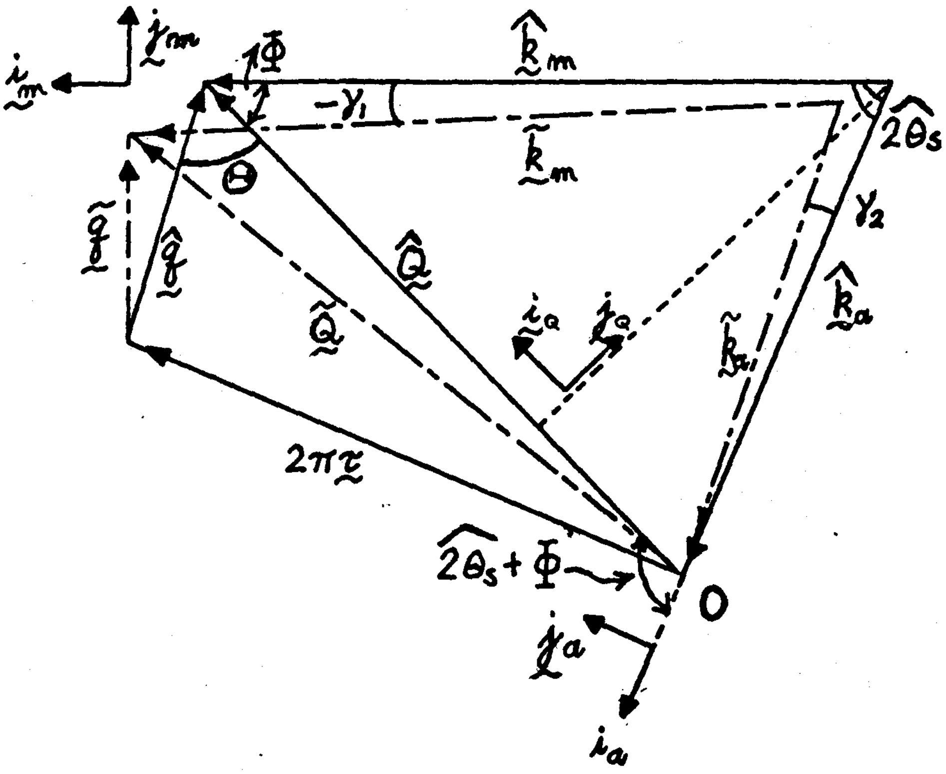

FIG. II-3-1-1

energy transfer, while an uncertainty in their relative direction of propagation only results in an uncertainty of the momentum-transfer.

The most probable wave vector values are defined by

$$\hat{k}_m = \frac{\pi}{d_m \sin(\hat{\theta}_m)} \quad \text{(3-a)} \quad ; \quad \hat{k}_a = \frac{\pi}{d_a \sin(\hat{\theta}_a)} \quad \text{(3-b)}$$

Any $(\tilde{\underset{\sim}{Q}},\tilde{\omega})$ process is obviously related to the most probable $(\hat{\underset{\sim}{Q}},\hat{\omega})$ process by the deviations of the incident and scattered wave vectors from their central values defined in equations (3) by

$$\Delta \underset{\sim}{k}_m = \tilde{\underset{\sim}{k}}_m - \hat{\underset{\sim}{k}}_m \quad \text{(4-a)} \quad ; \quad \Delta \underset{\sim}{k}_a = \tilde{\underset{\sim}{k}}_a - \hat{\underset{\sim}{k}}_a \quad \text{(4-b)}$$

The corresponding shifts in energy and momentum transfer are

$$\Delta \underset{\sim}{Q} = \tilde{\underset{\sim}{Q}} - \hat{\underset{\sim}{Q}} = \Delta \underset{\sim}{k}_m - \Delta \underset{\sim}{k}_a \quad \text{(5-a)}$$

$$\begin{aligned} \Delta \varepsilon &= \hbar(\tilde{\omega} - \hat{\omega}) = \frac{h^2}{2M}\left\{(\tilde{k}_m^2 - \tilde{k}_a^2) - (\hat{k}_m^2 - \hat{k}_a^2)\right\} \\ &= \frac{\hbar^2}{M}\left\{(\hat{\underset{\sim}{k}}_m \bullet \Delta \underset{\sim}{k}_m - \hat{\underset{\sim}{k}}_a \bullet \Delta \underset{\sim}{k}_a) + \frac{1}{2}(\Delta k_m)^2 - \frac{1}{2}(\Delta k_a)^2\right\} \end{aligned} \quad \text{(5-b)}$$

Now we may consider a few interesting cases; these are illustrated in fig. II-3-i-2.

a) Assume that $\Delta \underset{\sim}{k}_m = \Delta \underset{\sim}{k}_a = \Delta \underset{\sim}{k}$

then $\quad \Delta \underset{\sim}{Q} = 0$

and $\quad \Delta \varepsilon = \frac{\hbar^2}{M}(\hat{\underset{\sim}{k}}_m - \hat{\underset{\sim}{k}}_a) \bullet \Delta \underset{\sim}{k} = \frac{\hbar^2}{M}\hat{\underset{\sim}{Q}} \bullet \Delta \underset{\sim}{k}$

Observe that if $\hat{\underset{\sim}{Q}}$ and $\Delta \underset{\sim}{k}$ are orthogonal, then there is no shift in either $\underset{\sim}{Q}$ or ω.

a) $\Delta \underset{\sim}{k}_m = \Delta \underset{\sim}{k}_a = \Delta \underset{\sim}{k} \quad \Rightarrow \begin{cases} \Delta \underset{\sim}{Q} = 0 \\ \Delta \mathcal{E} = 2\, \hat{\underset{\sim}{Q}} \cdot \Delta \underset{\sim}{k} \end{cases}$

$\hat{\underset{\sim}{Q}} \cdot \Delta \underset{\sim}{k} = 0 \Rightarrow \Delta \omega = 0$

---

b) $\Delta \underset{\sim}{k}_a = 0 \quad \Rightarrow \begin{cases} \Delta \underset{\sim}{Q} = \Delta \underset{\sim}{k}_m \\ \Delta \mathcal{E} = 2\, \hat{\underset{\sim}{k}}_m \cdot \Delta \underset{\sim}{k}_m \end{cases}$

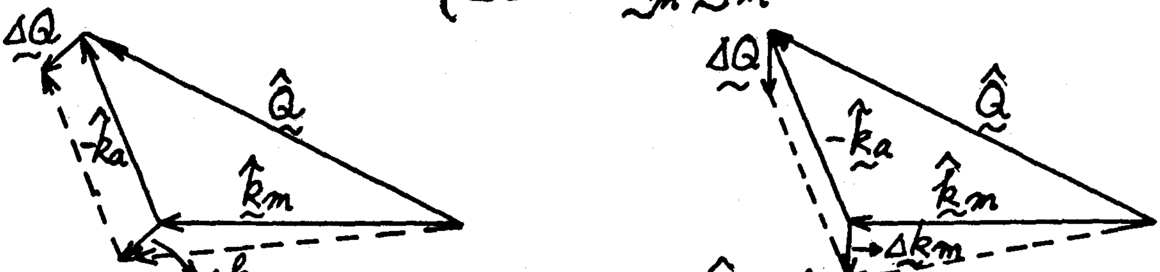

$\hat{\underset{\sim}{k}} \cdot \Delta \underset{\sim}{k}_m = 0 \Rightarrow \Delta \omega = 0$

---

c) $\underset{\sim}{k}_m \cdot \Delta \underset{\sim}{k}_m = \underset{\sim}{k}_a \cdot \Delta \underset{\sim}{k}_a \quad \Rightarrow \begin{cases} \Delta \underset{\sim}{Q} = \Delta \underset{\sim}{k}_m - \Delta \underset{\sim}{k}_a \\ \Delta \mathcal{E} = 0 \end{cases}$

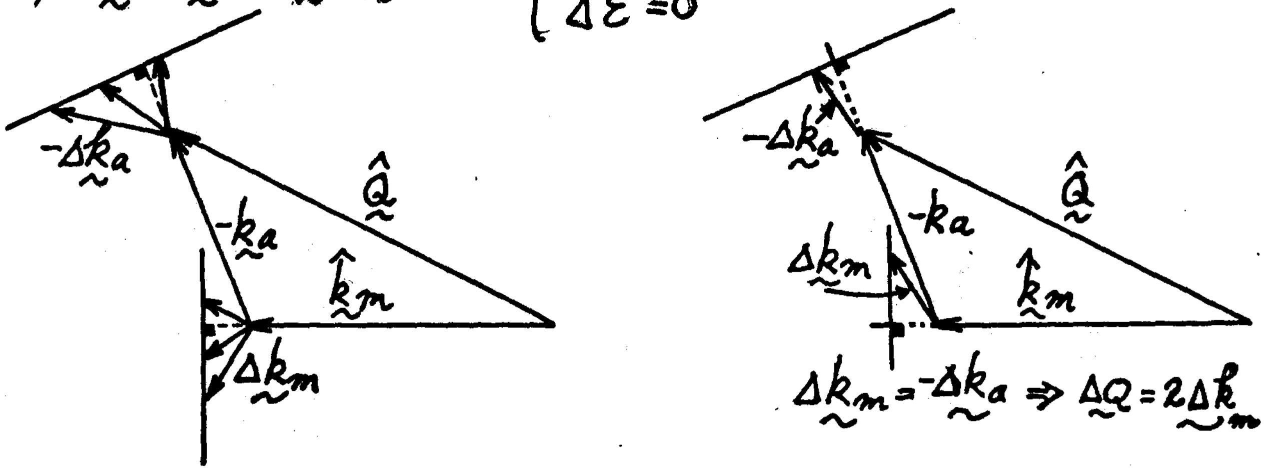

$\Delta \underset{\sim}{k}_m = -\Delta \underset{\sim}{k}_a \Rightarrow \Delta \underset{\sim}{Q} = 2 \Delta \underset{\sim}{k}_m$

Fig. II-3-i-2; illustration of first order shifts in $\underset{\sim}{Q}$ and ω in some interesting cases
Note : $\frac{\hbar^2}{2M} = 1$

b) If $\Delta \underset{\sim}{k}_a = 0$ then $\Delta \underset{\sim}{Q} = \Delta \underset{\sim}{k}_m$

and
$$\Delta \varepsilon = \frac{\hbar^2}{M}(\hat{\underset{\sim}{k}}_m + \Delta \underset{\sim}{k}_m/2) \cdot \Delta \underset{\sim}{k}_m$$
$$\cong \frac{\hbar^2}{M}\hat{\underset{\sim}{k}}_m \cdot \Delta \underset{\sim}{k}_m \quad \text{(to first order)}$$

Thus there is no shift in energy (to first order) for incident wave vectors whose projection on the direction of propagation of k_m (i.e. defined by the unit vector $\underset{\sim}{i}_m$ as defined below) is equal to k_m. Obviously the same type of argument holds if $\Delta \underset{\sim}{k}_m$ is assumed zero instead of $\Delta \underset{\sim}{k}_a$.

c) If $\hat{\underset{\sim}{k}}_m \cdot \Delta \underset{\sim}{k}_m - \hat{\underset{\sim}{k}}_a \cdot \Delta \underset{\sim}{k}_a = 0$

then $\Delta \underset{\sim}{Q} \neq 0$ in general

and $\Delta \varepsilon = 0$ (to first order)

If also $\Delta \underset{\sim}{k}_m = \Delta \underset{\sim}{k}_a$ as in a) then there is no shift in both $\underset{\sim}{Q}$ and ω in first order.

Thus if we define the transmission functions: (using the symbols defined in table I-1).

as $C_m(\hat{k}_m, \Delta k_m, \gamma_1)$ for the monochromator crystal

$C_a(\hat{k}_a, \Delta k_a, \gamma_2)$ for the analyser crystal

and $T_i(\gamma_i, \delta_i)$ for the individual collimators, the index i=0,1,2,3 referring to the respective regions: in-pile, monochromator-to-specimen, specimen-to-analyser and analyser-to-counter, the total probability for the propagation of a neutron through each of the elements of a spectrometer is

$$P(\underset{\sim}{\tilde{k}}_m, \underset{\sim}{\tilde{k}}_a) = \prod_{i=0}^{3} T_i(\gamma_i, \delta_i) C_m(\hat{k}_m, \Delta k_m, \gamma_1) C_a(\hat{k}_a, \Delta k_a, \gamma_2) \qquad (6)$$

As usual, the γ_i are defined as positive when they are measured toward the normal to the scattering plane. This convention differs from that used by Cooper/Nathans in that they used a counter-clockwise positive direction, resulting in a positive angle corresponding to an increase in the magnitude of the scattered wave vector in the case of the analyser and to a decrease in the case of the monochromator. It seems desirable to remove this asymmetry and at the same time be consistent with the previous notation; thus, as before, an increase in the magnitude of the angle γ always corresponds to a decrease in the magnitude of the most probable wave vector.

From the considerations made in section II-1 on collimators, it is obvious that the transmission function of a collimator may be decomposed in two terms dependent respectively on the vertical and on the horizontal direction of propagation:

$$T_i(\gamma_i, \delta_i) = T_i^h(\gamma_i) T_i^v(\delta_i)$$

where $T_i^h(\theta_i) = \exp(-\frac{1}{2}\theta_i^2/\alpha_i^2)$; $T_i^v(\theta_i) = \exp(-\frac{1}{2}\theta_i^2/\beta_i^2)$

We may rewrite the expression for the total probability, using the result of equation II-2-(22), as

$$P(\tilde{\underset{\sim}{k}}_m, \tilde{\underset{\sim}{k}}_a) = P_h(\tilde{\underset{\sim}{k}}_m, \tilde{\underset{\sim}{k}}_a) \times P_v(\tilde{\underset{\sim}{k}}_m, \tilde{\underset{\sim}{k}}_a) \qquad (7)$$

$$P_h(\tilde{\underset{\sim}{k}}_m, \tilde{\underset{\sim}{k}}_a) = \pi(\hat{k}_m, \delta k_m, \gamma_1) \times \pi(\hat{k}_a, \delta k_a, \gamma_2) \qquad (8\text{-a})$$

$$P_v(\tilde{\underset{\sim}{k}}_m, \tilde{\underset{\sim}{k}}_a) = \left\{\prod_{i=0}^{3} T_i^v(\delta_i)\right\} \qquad (8\text{-b})$$

Thus, the transmission probability may be separated into two independent terms corresponding to processes in and out of the scattering plane, since equation II-2-(22) shows no correlation between the scattered wave vector and the vertical divergence angles.

We show in appendix A-2 that the in-pile and counter vertical deviation angles (δ_o and δ_3) are not independent but are respectivly related to the vertical divergence angles in the monochromator-to-sample and in the sample-to-analyser regions (δ_1 and δ_2); hence, the function $P_v(\tilde{\underset{\sim}{k}}_m, \tilde{\underset{\sim}{k}}_a)$ is actually a function of δ_1 and δ_2 (equation 8-b). Using equations II-2-(22) and (23), we may write

$$P_h(\tilde{\underset{\sim}{k}}_m, \tilde{\underset{\sim}{k}}_a) = P_h^o \exp[-\frac{1}{2}(\Sigma_m^2 + \Sigma_a^2)] \qquad (9a)$$

$$\Sigma_m^2 = \Sigma_1^m \hat{k}_m^2 \gamma_1^2 + \Sigma_2^m \hat{k}_m \gamma_1 \Delta k_m + \Sigma_3^m (\Delta k_m)^2 \quad (9b); \quad \Sigma_a^2 = \Sigma_a^2 \hat{k}_a^2 \gamma_2^2 + \Sigma_2^a \hat{k}_a \gamma_2 \Delta k_a + \Sigma_3^a (\Delta k_a)^2 \quad (9c)$$

where

$$\Sigma_1^m = [\frac{1}{\alpha_o^2} + \frac{1}{\alpha_1^2} + \frac{1}{\eta_m^2}]/\hat{k}_m^2 \quad (10a); \quad \Sigma_1^a = [\frac{1}{\alpha_3^2} + \frac{1}{\alpha_2^2} + \frac{1}{\eta_a^2}]/\hat{k}_a^2 \quad (10b)$$

$$\Sigma_2^m = \frac{2\tan(\hat{\theta}_m)}{\hat{k}_m^2}[\frac{2}{\alpha_o^2} + \frac{1}{\eta_m^2}] \quad (10c); \quad \Sigma_2^a = \frac{2\tan(\hat{\theta}_a)}{\hat{k}_a^2}[\frac{2}{\alpha_3^2} + \frac{1}{\eta_a^2}] \quad (10d)$$

$$\Sigma_3^m = \frac{\tan^2(\hat{\theta}_m)}{\hat{k}_m^2}[\frac{4}{\alpha_o^2} + \frac{1}{\eta_m^2}] \quad (10e); \quad \Sigma_3^a = \frac{\tan^2(\hat{\theta}_a)}{\hat{k}_a^2}[\frac{4}{\alpha_3^2} + \frac{1}{\eta_a^2}] \quad (10f)$$

and

$$P_v(k_m, k_a) = P_v^o \exp[-\frac{1}{2}(a_{11}^2 k_m^2 \delta_1^2 + a_{12}^2 k_a^2 \delta_2^2)] \qquad (11a)$$

where

$$a_{11}^2 = \frac{1}{(4\tan^2(\hat{\theta}_m)\eta'^2_m + \beta_o^2)\hat{k}_m^2} + \frac{1}{\beta_1^2 \hat{k}_m^2} \qquad (11b)$$

$$a_{12}^2 = \frac{1}{\beta_2^2 \hat{k}_a^2} + \frac{1}{(4\tan^2(\hat{\theta}_a)\eta'^2_a + \beta_3^2)\hat{k}_a^2} \qquad (11c)$$

The symbols being properly defined in table I-1.

Since there is no unique path for a neutron going through a $(\tilde{\underset{\sim}{Q}},\tilde{\omega})$ scattering process, the resolution function for a given point $(\tilde{\underset{\sim}{Q}},\tilde{\omega})$ is obtained by integrating the probability of such a process over all possible paths (in $\underset{\sim}{Q}-\omega$ space) leading to that transfer in momentum and energy, namely the sextuple integration

$$R(\tilde{\underset{\sim}{Q}},\tilde{\omega}) = \int d\tilde{\underset{\sim}{k}}_m\, d\tilde{\underset{\sim}{k}}_a\, P(\tilde{\underset{\sim}{k}}_m,\tilde{\underset{\sim}{k}}_a)\,\delta(\tilde{\underset{\sim}{Q}}-(\tilde{\underset{\sim}{k}}_m-\tilde{\underset{\sim}{k}}_a))\,\delta(\tilde{\omega}-\frac{\hbar}{2M}(\tilde{k}_m^2-\tilde{k}_a^2)) \tag{12}$$

where the vector notation was used in the arguments of the functions for compactness and the constraints on $\underset{\sim}{k}_m$ and $\underset{\sim}{k}_a$ are given by the delta functions.

The observed intensity for a given instrument setting is the convolution of the resolution function and the scattering cross-section, i.e. the quadruple integration

$$I(\hat{\underset{\sim}{Q}},\hat{\omega}) = \int R(\tilde{\underset{\sim}{Q}},\tilde{\omega})\,\sigma(\tilde{\underset{\sim}{Q}},\omega)\,d\tilde{\underset{\sim}{Q}}\,d\omega \tag{13}$$

$$= \int R(\hat{\underset{\sim}{Q}}+\Delta\underset{\sim}{Q},\hat{\omega}+\Delta\omega)\,\sigma(\hat{\underset{\sim}{Q}}+\Delta\underset{\sim}{Q},\hat{\omega}+\Delta\omega)\,d(\Delta\underset{\sim}{Q})\,d(\Delta\omega) \tag{14}$$

The second form where the variables of integration are the deviations from the central point $(\hat{\underset{\sim}{Q}},\hat{\omega})$ turns out to be the natural choice here and the analytic form of the resolution function using these variables can be conveniently formulated in matrix notation; the explicit form of the matrix elements will now be derived.

Let us define three sets of right-handed orthonormal vectors* namely $(\underset{\sim}{i}_Q,\underset{\sim}{j}_Q,\underset{\sim}{l}_Q)$, $(\underset{\sim}{i}_m,\underset{\sim}{j}_m,\underset{\sim}{l}_m)$ and $(\underset{\sim}{i}_a,\underset{\sim}{j}_a,\underset{\sim}{l}_a)$ in relation to respectivly the central values of the wave vector transfer $\hat{\underset{\sim}{Q}}$,

*Note: that is, obeying the relation $\underset{\sim}{i}_x \wedge \underset{\sim}{j}_x = \underset{\sim}{l}_x$ (x=Q,m,a) the incident wave vector $\hat{\underset{\sim}{k}}_m$ and the scattered wave vector $\hat{\underset{\sim}{k}}_a$. As illustrated in fig. II-3-i-1, the i_x vectors (x=Q,m,a) are chosen to lie in the direction of the corresponding wave vectors and the j_x vectors, perpendicular to the associated i_x, are in the scattering plane; the third vectors (l_x) are perpendicular to the scattering plane, parallel to each other.

Consider first the uncertainty in momentum transfer $\underset{\sim}{Q}$; equations (4) and (5-a) have already shown that it is of the form:

$$\Delta \underset{\sim}{Q} = \Delta \underset{\sim}{k}_m - \Delta \underset{\sim}{k}_a \qquad \text{(5-a)}$$

Let the vectors on the right hand side be expressed in terms of their respective orthonormal vectors:

i.e.

$$\Delta \underset{\sim}{k}_m = x_m \underset{\sim}{i}_m + y_m \underset{\sim}{j}_m + z_m \underset{\sim}{l}_m \qquad \text{(15-a)}$$

$$\Delta \underset{\sim}{k}_a = x_a \underset{\sim}{i}_a + y_a \underset{\sim}{j}_a + z_a \underset{\sim}{l}_a \qquad \text{(15-b)}$$

By a trivial linear transformation, these can also be expressed in terms of the set $(\underset{\sim}{i}_Q, \underset{\sim}{j}_Q, \underset{\sim}{l}_Q)$. Fig. II-4-i-1 shows the rotation angle between $\underset{\sim}{i}_m$ and $\underset{\sim}{i}_Q$, that is between $\hat{\underset{\sim}{k}}_m$ and $\hat{\underset{\sim}{Q}}$, labelled as Φ and that it is equal to $(\widehat{2\theta}_s + \Phi)$ between $\underset{\sim}{i}_a$ and $\underset{\sim}{i}_Q$. Thus,

$$\Delta \underset{\sim}{k}_m = (x_m \hat{b} + y_m \hat{a}) \underset{\sim}{i}_Q + (-x_m \hat{a} + y_m \hat{b}) \underset{\sim}{j}_Q + z_m \underset{\sim}{l}_Q \qquad \text{(16-a)}$$

$$\Delta \underset{\sim}{k}_a = (x_a \hat{B} + y_a \hat{A}) \underset{\sim}{i}_Q + (-x_a \hat{A} + y_a \hat{B}) \underset{\sim}{j}_Q + z_a \underset{\sim}{l}_Q \qquad \text{(16-b)}$$

where

$$\hat{a} = \sin\Phi \quad ; \quad \hat{A} = \sin(\Phi + \widehat{2\theta}_s)$$

$$\hat{b} = \cos\Phi \quad ; \quad \hat{B} = \cos(\Phi + \widehat{2\theta}_s)$$

Equation (5-a) may then be written as

$$\Delta \underset{\sim}{Q} = X_1 \underset{\sim}{i}_Q + X_2 \underset{\sim}{j}_Q + X_3 \underset{\sim}{l}_Q \qquad \text{(17)}$$

where $$X_1 = x_m\hat{b} + y_m\hat{a} - x_a\hat{B} - y_a\hat{A} \qquad (18\text{-a})$$

$$X_2 = -x_m\hat{a} + y_m\hat{b} + x_a\hat{A} - y_a\hat{B} \qquad (18\text{-b})$$

$$X_3 = z_m - z_a \qquad (18\text{-c})$$

Notice that these values are the negative of those used by Cooper/Nathans since these workers had defined $\underset{\sim}{Q}$ in the opposite way as what was done in eq. (1).

Now consider the uncertainty in energy transfer; equation (5-b) which includes second order terms may be simplified to read in first order:

$$\Delta\epsilon = \frac{\hbar^2}{M}(\underset{\sim}{\hat{k}_m} \bullet \underset{\sim}{\Delta k_m} - \underset{\sim}{\hat{k}_a} \bullet \underset{\sim}{\Delta k_a}) \qquad (19)$$

In conformity with equation (15) and with the definition of the $(\underset{\sim}{i}_m, \underset{\sim}{j}_m, \underset{\sim}{l}_m)$ and $(\underset{\sim}{i}_a, \underset{\sim}{j}_a, \underset{\sim}{l}_a)$ orthonormal vectors, the two scalar products in equation (19) can be simplified

and $$\Delta\mathcal{E} = \frac{h^2}{M}(x_m\hat{k}_m - x_a\hat{k}_a) \qquad (20)$$

being the same as would have been obtained by taking partial derivatives in eq. (2). Thus the longitudinal component of the shift in magnitude of the scattered wave vector

is $$x_a = \Lambda x_m - \Omega \qquad (21)$$

where $$\Lambda = \hat{k}_m/\hat{k}_a \quad ; \quad \Omega = M\Delta\omega/(\hat{k}_a\hbar)$$

In the following, we will treat the shifts in momentum transfer and energy on equal footing as components of a "distance" in $(\underset{\sim}{Q}-\omega)$ space and we can achieve a symmetrized notation with equations (18-a,b,c) by writing (5-b) as

$$X_4 = \Delta\omega = \tilde{\omega} - \hat{\omega} \qquad (18\text{-d})$$

Similarly, by using the relations (18-a) and (18-b) it is possible to write y_m and y_a in the same form as x_a in equation (21) above, i.e.

$$\alpha y_m = -BX_1 + AX_2 + \beta x_m - x_a \qquad (22\text{-a})$$

$$\alpha y_a = -bX_1 + aX_2 + x_m - \beta x_a \qquad (22\text{-b})$$

where $\alpha = \sin(\widehat{2\theta_s}) = \hat{b}\hat{A} - \hat{a}\hat{B}$; $\beta = \cos(\widehat{2\theta_s}) = \hat{a}\hat{A} + \hat{b}\hat{B}$

But we know from equation (21) that x_a is a function of x_m

$$\alpha y_m = -\hat{B}X_1 + \hat{A}X_2 + (\beta - \Lambda)x_m + \Omega \qquad (23\text{-a})$$

$$\alpha y_a = -\hat{b}X_1 + \hat{a}X_2 + (1 - \beta\Lambda)x_m + \beta\Omega \qquad (23\text{-b})$$

Equations (21), (23-a) and (23-b) can now be written in condensed symmetrized form:

$$\left\| \begin{array}{llr} x_a = \Lambda x_m + H & & (24\text{-a}) \\ y_m = Cx_m + D \; ; & C = (\beta - \Lambda)/\alpha & (24\text{-b}) \\ y_a = Ex_m + F \; ; & E = (1 - \beta\Lambda)/\alpha & (24\text{-c}) \end{array} \right.$$

It might be appropriate to pause here and explain that the purpose of the above mathematical transformations was simply to express the deviations of the incident and scattered wave vectors as a function of the deviation in $(\underset{\sim}{Q},\omega)$ space from the central point $(\hat{\underset{\sim}{Q}},\hat{\omega})$ in order to perform the integral (12) for the resolution function. The delta functions in that integral giving the constraints between the variables of integration were used to express these variables as a function of x_m thus effectivly transforming a multiple integral into an integration over a single variable.

In equations (24-a,b,c) the dependence on X_1, X_2, X_3 and X_4 (i.e. the "distance" in $(\underset{\sim}{Q}-\omega)$ space comes from the terms H, D and F which may be written

$$D = \underset{\sim}{d}\bullet\underset{\sim}{X} \ \text{(25-a)}; \quad F = \underset{\sim}{f}\bullet\underset{\sim}{X} \ \text{(25-b)}; \quad H = \underset{\sim}{h}\bullet\underset{\sim}{X} \ \text{(25-c)}$$

the components of d, f and h being

$$\underset{\sim}{d} = (-\hat{B}/\alpha, \ \hat{A}/\alpha, \ 0, \ M/\alpha\hbar\hat{k}_a) \qquad \text{(26-a)}$$

$$\underset{\sim}{f} = (-\hat{b}/\alpha, \ \hat{a}/\alpha, \ 0, \ \beta M/\hbar\hat{k}_a\alpha) \qquad \text{(26-b)}$$

$$\underset{\sim}{h} = (\ 0, \ 0, \ 0, \ -M/\hbar\hat{k}_a) \qquad \text{(26-c)}$$

We are now in a position to calculate the integral (12) for the contribution to the resolution function of processes taking place in the scattering plane; the effect of vertical divergence will soon be considered but for the time being the variables of interest are the horizontal components of $\widetilde{d\underset{\sim}{k}}_m$ (i.e. x_m, y_m) and $\widetilde{d\underset{\sim}{k}}_a$ (i.e. x_a, y_a) in equation (12).

Since the small angle approximation is valid, the deviation angles γ_1 and γ_2 are coupled to the quantities y_m and y_a through the relations:

$$\gamma_1 = y_m/\hat{k}_m \quad \text{(27-a)} \ ; \qquad \gamma_2 = -y_a/\hat{k}_a \qquad \text{(27-b)}$$

The negative sign in the second expression stems from the angle convention in fig. II-3-i-1. Equation (9) may now be written in terms of the components x_m, x_a, y_m and y_a without reference to the deviation angles and the term of the exponent becomes

$$\Sigma_m^2 + \Sigma_a^2 = \Sigma_1^m y_m^2 + \Sigma_2^m x_m y_m + \Sigma_3^m x_m^2 + \Sigma_1^a y_a^2 - \Sigma_2^a x_a y_a + \Sigma_3^a x_a^2 \qquad (28)$$

Replacing the terms x_a, y_m and y_a by their expressions given in (24) renders the argument of the exponential function in equation (9) particularly simple so that

$$R_h(\tilde{\underset{\sim}{Q}},\tilde{\omega}) = \int_{-\infty}^{\infty} dx_m P_h^o \exp[\frac{-1}{2}(A'x_m^2 + B'x_m + C')] \tag{29}$$

where

$$A' = \Sigma_1^m C^2 + \Sigma_1^a E^2 + \Sigma_2^m C - \Sigma_2^a \Lambda E + (\Sigma_3^m + \Sigma_3^a \Lambda^2) \tag{30}$$

$$B' = (2\Sigma_1^m C + \Sigma_2^m) D + (2E\Sigma_1^a - \Sigma_2^a \Lambda) F + (2\Sigma_3^a \Lambda - \Sigma_2^a E) H \tag{31}$$

$$C' = \Sigma_1^m D^2 + \Sigma_1^a F^2 - \Sigma_2^a FH + \Sigma_3^a H^2 \tag{32}$$

* * * * * *

Using the results of appendix A-1, integral (29) may be evaluated to be

$$R_h(\tilde{\underset{\sim}{Q}},\tilde{\omega}) = R_h^o \exp[\frac{-1}{2}(C' - \frac{B'^2}{4A'})] \tag{33}$$

In order to obtain an explicit dependence on the natural variables X_i (i=1,4), it is necessary to carry out the substitution in the exponential (33) of the relations (25) and (26). So we may write for convenience

$$C' - \frac{B'^2}{4A'} = g_o D^2 + g_1 F^2 + g_2 H^2 + g_3 FH + g_4 DF + g_5 DH \tag{34}$$

The X_i dependence is contained in the terms D,F and H. Their coefficients are defined by:

$$g_0 = \Sigma_1^m - (2\Sigma_1^m C + \Sigma_2^m)^2/(4A') \tag{35a}$$

$$g_1 = \Sigma_1^a - (2\Sigma_1^a E - \Sigma_2^a \Lambda)^2/(4A') \tag{35b}$$

$$g_2 = \Sigma_3^a - (2\Sigma_3^a \Lambda - \Sigma_2^a E)^2/(4A') \tag{35c}$$

$$g_3 = -[\Sigma_2^a + (2\Sigma_1^a E - \Sigma_2^a \Lambda)(2\Sigma_3^a \Lambda - \Sigma_2^a E)]/(2A') \tag{35d}$$

$$g_4 = -(2\Sigma_1^m C + \Sigma_2^m)(2\Sigma_1^a E - \Sigma_2^a \Lambda)/(2A') \tag{35e}$$

$$g_5 = -(2\Sigma_1^m C + \Sigma_2^m)(2\Sigma_3^a \Lambda - \Sigma_2^a E)/(2A') \tag{35f}$$

From the expressions (25-a,b,c) for D, F and H, it should be obvious that the argument of the exponential is of the form:

$$\frac{-1}{2} \sum_{r,s=1,2,4} M_{rs} X_r X_s \tag{36}$$

where

$$\begin{aligned} M_{rs} = \tfrac{1}{2}[&2g_o d_r d_s + 2g_1 f_r f_s + 2g_2 h_r h_s + \\ &g_3(f_r h_s + f_s h_r) + g_4(d_r f_s + d_s f_r) + g_5(d_r h_s + d_s h_r)] \end{aligned} \tag{37}$$

Let us recapitulate. The basic equation for the calculation of the resolution function is equation (12). We have seen with equations (7) and (8) that the probability function $P(\tilde{\utilde{k}}_m, \tilde{\utilde{k}}_a)$ could be separated into a product of two functions of different variables describing the neutron propagation in the scattering plane and perpendicular to it. Hence the sextuple integral in (12) could be writen as the product of a quadruple integral

$$\begin{aligned} R_h(\hat{\utilde{Q}}+\Delta \utilde{Q}, \hat{\omega}+\Delta\omega) = &\int dx_m dy_m dx_a dy_a \; P_h(\tilde{\utilde{k}}_m, \tilde{\utilde{k}}_a) \\ &\times \delta\{\Delta \utilde{Q} - (x_m \utilde{i}_m + y_m \utilde{j}_m - x_a \utilde{i}_a - y_a \utilde{j}_a)\} \\ &\times \delta\{\Delta\omega - \frac{\hbar}{2M}(\hat{k}_m x_m - \hat{k}_a x_a)\} \end{aligned} \tag{38}$$

and a double integral

$$R_v(\hat{\underset{\sim}{Q}}+\Delta\underset{\sim}{Q},\hat{\omega}+\Delta\omega) = \int dz_m dz_a \; P_v(\tilde{\underset{\sim}{k}}_m,\tilde{\underset{\sim}{k}}_a)$$

$$\times \, \delta\{\Delta\underset{\sim}{Q} - (z_m - z_a)\underset{\sim}{\ell}_o\}$$

$$\times \, \delta(\Delta\omega) \qquad (39)$$

the function P_h and P_v being given in (8). The delta functions expresses the constraints on the components of the incident and scattered wave vector so that the scattering process is one which is shifted a distance $(\Delta\underset{\sim}{Q},\Delta\omega)$ from the central process $(\hat{\underset{\sim}{Q}},\hat{\omega})$ (See equations 5-a,b).

Let us now proceed with the determination of the remaining matrix elements. First we observe the fact that the absence of correlation between vertical angular deviation and the magnitude of the scattered wave vectors allows us to write immediately

$$M_{3S} = M_{S3} = 0 \quad (S=1,2) \qquad (40)$$

Similarly, the fact that there is no first order shift in energy as a function of vertical wave vector components (Eq. 20) results in

$$M_{34} = M_{43} = 0 \qquad (41)$$

There now only remains M_{33} to evaluate by performing the integration in (39). As before we use the small angle approximation to write

$$\delta_1 = z_m/\hat{k}_m \text{ (42-a)}; \quad \delta_2 = z_a/\hat{k}_a \text{ (42-b)}$$

and the expression for $P_v(\tilde{\underset{\sim}{k}}_m,\tilde{\underset{\sim}{k}}_a)$ (Eq. 11) becomes

$$P_v(\tilde{\underset{\sim}{k}}_m,\tilde{\underset{\sim}{k}}_a) = P_v^o \exp\{-\tfrac{1}{2}(a_{11}^2 \; z_m^2 + a_{12}^2 \; z_a^2)\} \qquad (43)$$

The variables z_m and z_a are coupled to each other by the first delta function in (39) and using equation (18-c) we may write:

$$z_a = z_m - X_3$$

z_m is now the only variable of integration and we can evaluate (39) as

$$P_v^o \exp\{-\tfrac{1}{2} a_{12}^2 X_3^2\} \int dz_m \exp\{-\tfrac{1}{2}(a_{11}^2 + a_{12}^2) z_m^2 - 2a_{12}^2 X_3 a_m\} \quad (44)$$

With the result of appendix A-1 we get

$$R_v(\hat{\underset{\sim}{Q}}+\Delta\underset{\sim}{Q}, \hat{\omega}+\Delta\omega) = R_v^o \exp\{-\tfrac{1}{2} M_{33} X_3^2\} \quad (45)$$

where

$$M_{33} = \frac{a_{11}^2 \; a_{12}^2}{a_{11}^2 + a_{12}^2} \quad (46)$$

which completes the determination of the matrix elements.

Equation (7-12) lead to the final expression for the resolution function

$$R(\hat{\underset{\sim}{Q}}+\Delta\underset{\sim}{Q}, \hat{\omega}+\Delta\omega) = R(\underset{\sim}{X}) = R_o \exp\left(-\tfrac{1}{2} X^T M X\right) \quad (47)$$

where $R_o = R_H^o \times R_V^o$ is the value of the resolution function for the central process $(\hat{\underset{\sim}{Q}}, \omega)$; it could be called the luminosity of the instrument for a particular setting and although it could be calculated in principle from a knowledge of the absolute characteristics of each of the spectrometer components (e.g. crystal reflectivities, incident flux distribution, counter sensitivity, etc), in practice one is rather interested in knowing how the resolution can be optimized for the measurement of a particular phonon and how the apparent peak position is related to the true peak position and this is governed by the exponential term in (47).

ii) The matrix notation is mathematically convenient but does not have an immediate physical interpretation as such. However the equation $X^TMX=p$ can be visualized as an ellipsoid defining an isoprobability surface in 4-dimensional $(\underset{\sim}{Q},\omega)$ space such that the quantity $e^{-p/2}$ is the probability of detection of a neutron having gone through a $[(\hat{\underset{\sim}{Q}},\hat{\underset{\sim}{\omega}})+\underset{\sim}{X}]$ scattering process relative to the probability for a $(\hat{\underset{\sim}{Q}},\hat{\omega})$ process. It turns out that this ellipsoid always has a principal axis along X_3 (ΔQ_z), a second one very nearly parallel to X_1, and the last two are rotated relative to the X_2-X_4 axis. This last feature has a most important consequence since it allows the possibility of focussing by introducing a correlation between the orientation of the ellipsoid and the dispersion surface of the specimen. The dispersion surface is defined as the loci of points in $(\underset{\sim}{Q},\omega)$ space where the dispersion relation of the specimen $\omega\equiv\omega(\underset{\sim}{q}+\underset{\sim}{\tau})$ is satisfied. Consider a small portion of that surface which does not contain any singularity (i.e. reciprocal lattice point, or Kohn kinks); then the energy gradient with respect to wave vector is a well defined quantity and we may write

$$\omega(\hat{\underset{\sim}{q}}+\delta\underset{\sim}{q}) = \omega(\hat{\underset{\sim}{q}}) + \delta\underset{\sim}{q}\cdot\underset{\sim}{\nabla}_q\omega(\hat{q}) + 0(\delta q^2) \qquad (48)$$

The point is that the particular value of the energy gradient has but a small effect on the linewidth when $\text{grad}_q\omega$ is parallel to $\underset{\sim}{Q}$(i.e. $\underset{\sim}{i}_Q$). Such is not the case when $\text{grad}_q\omega$ is parallel to $\underset{\sim}{j}_Q$ since the amount of parallelism between the dispersion surface and the tilted resolution ellipsoid determines the intensity distribution along the scan. This focussing is more pronounced when the dispersion surface is parallel to the ellipsoid and it falls off with departure from parallelism. In general, $\mathrm{grad}_q \omega$ is not exactly parallel to either $X_1 i_{\underset{\sim}{Q}}$ or $X_2 j_{\underset{\sim}{Q}}$ and may lie anywhere between these positions (See below); in this general case, it is only the component of $\mathrm{grad}_q \omega$ along $X_2 j_{\underset{\sim}{Q}}$ which determines the focussing, as the other component of the energy gradient is in a direction where the principal axis of the ellipsoid lies in the plane $\omega=0$.

We may now anticipate and, referring to the expression for the one-phonon scattering cross-section, we observe that the polarization dependent term $(Q\cdot\xi)^2$ governs the choice of the position in reciprocal space suitable for observing a particular phonon. The situation is particularly simple along the symmetry direction since only then are the polarizations either truly longitudinal or truly transverse. Another simplification found in this case is the fact that the energy gradient is along the symmetry direction because of reflection invariance perpendicular to the symmetry direction.

Thus, a longitudinal phonon is measured in a direction closely, if not, parallel to the vector $\underset{\sim}{Q}$; where it was previously shown that the only contribution to focussing comes from the component of the energy gradient parallel to the direction $X_2 j_{\underset{\sim}{Q}}$, which is indeed a small effect in the case of longitudinal phonons.

In the case of transverse phonons, on the other hand, measurements are carried out in a direction closely perpendicular to the vector $\underset{\sim}{Q}$, resulting in the energy gradient having a large component in the direction $X_2\underset{\sim}{j}_Q$ with correspondingly large possible focussing. The amount of focussing depends on the degree of parallelism between the dispersion surface and the ellipsoid; this degree of parallelism can be varied as the gradient varies along the symmetry direction or as the angle between $\underset{\sim}{Q}$ and $\underset{\sim}{q}$ varies. Focussing goes through a maximum when parallelism is complete; this is to be contrasted with the case of longitudinal phonons where the degree of focussing increases from zero as the angle between $\underset{\sim}{Q}$ and $\underset{\sim}{q}$ changes from the ideal value of $\pi/2$.

iii) The resolution function near a reciprocal lattice point can be measured in a straightforward way, as first suggested by Møller-[67], and the experimental procedure will not be repeated here. The point of interest is the fact that in the previous theoretical considerations, the natural variables were $X_1\underset{\sim}{i}_Q$ parallel to $\underset{\sim}{Q}$ and $X_2\underset{\sim}{j}_Q$ perpendicular to $\underset{\sim}{Q}$. However, although the measurements could be made by scanning in the direction of $\underset{\sim}{i}_Q$ and $\underset{\sim}{j}_Q$, it is more convenient to scan in the symmetry direction along which the phonons are measured and thus obtain the resolution function along the direction of interest. Obviously, the resolution function obtained in this way becomes less and less suitable the farther away in $(\underset{\sim}{Q},\omega)$ space a phonon is measured from a reciprocal lattice point $(\underset{\sim}{\tau},0)$ used to measure this function.

In order to compare the measured isoprobability contour and the calculated one, it is necessary to solve for the intersection of the resolution ellipsoid with the plane $(\underset{\sim}{q},\omega)$

A comparison between the calculated and measured contour affords an illustration of the worsening of the resolution from the specimen mosaic spread and will be discussed in Chapter III. For the time being we will briefly describe how to solve for the intersection of the resolution ellipsoid with the plane $(\underset{\sim}{q},\omega)$

The isoprobability "surface" is given by

$$X^T M X = \sum_1^4 X_r M_{rs} X_s = p \tag{49}$$

where p is a number such that $e^{-p/2}$ is the value of the resolution function at the "point" X. A general linear transformation to a new basis leaves (49) unchanged:

$$X'^T M' X' = p$$

Assume that X = AX' (A; a linear operation) thus:

$$\begin{aligned} X^T M X &= (AX')^T M (AX') \\ &= X'^T (A^T M A) X' \\ &= X'^T M' X' \end{aligned} \tag{50}$$

In this case, the linear transformation must leave X_3 and X_4 unchanged and rotates X_1 and X_2 along and perpendicular to the symmetry direction respectively. The operator A is necessarily of the form

$$A \equiv \begin{pmatrix} A_2 & 0 \\ O & I_2 \end{pmatrix}$$

where the submatrices are 2 x 2. The matrix A_2 is that for a simple rotation in the X_1 X_2 plane given by

$$\begin{pmatrix} \cos\Theta & -\sin\Theta \\ \sin\Theta & \cos\Theta \end{pmatrix}$$

where Θ is the angle between $\underset{\sim}{Q}$ and the symmetry direction.

Thus,

$$A^T \equiv \begin{pmatrix} A_2^T & O \\ O & I_2 \end{pmatrix}$$

and the new matrix given by

$$M' = A^T M A$$

can be calculated in a straightforward way. The matrix elements of M' are

$$M'_{11} = M_{11}\cos^2\Theta + M_{22}\sin^2\Theta + 2M_{12}\sin\Theta\cos\Theta \qquad (51a)$$

$$M'_{22} = M_{11}\sin^2\Theta + M_{22}\cos^2\Theta - 2M_{12}\sin\Theta\cos\Theta \qquad (51b)$$

$$M'_{33} = M_{33} \qquad (51c)$$

$$M'_{44} = M_{44} \qquad (51d)$$

$$M'_{21} = M'_{12} = -M_{11}\sin\Theta\cos\Theta + M_{22}\ \sin\Theta\cos\Theta + M_{12}(\cos^2\Theta-\sin^2\Theta) \qquad (51e)$$

$$M'_{41} = M'_{14} = M_{14}\cos\Theta + M_{24}\sin\Theta \qquad (51f)$$

$$M'_{42} = M'_{24} = -M_{14}\sin\Theta + M_{24}\cos\Theta \qquad (51g)$$

$$M'_{13} = M'_{31} = M'_{23} = M'_{32} = M'_{34} = M'_{43} = 0 \qquad (51h)$$

Knowing these matrix elements, it is a simple matter to solve for the intersection of the resolution ellipsoid with the (X'_1, X'_4) and (X'_2, X'_4) planes to obtain a contour which can be compared with experimental results. This calculation was incorporated in the computer programme for the calculation of the line shape which uses the theory of the next section.

4-Line shape of a neutron group for a one-phonon scattering process.

i) The scattered flux per unit solid angle when the instrument is "looking" at the point $(\hat{Q},\hat{\omega})$ is given by the equation II-3-(14), i.e.

$$I(\hat{\underset{\sim}{Q}},\hat{\omega}) = \int R(\hat{\underset{\sim}{Q}}+\Delta\underset{\sim}{Q},\hat{\omega}+\Delta\omega)\frac{d^2\sigma}{d_\Omega d(\Delta\omega)}(\hat{\underset{\sim}{Q}}+\Delta\underset{\sim}{Q},\hat{\omega}+\Delta\omega)\,d(\Delta\underset{\sim}{Q})\,d(\Delta\omega) \qquad (1)$$

and the expression for the partial differential cross-section for a one-phonon process is

$$\frac{d^2\sigma}{d\Omega d\omega} = (2\pi)^3\frac{\hbar}{2}\frac{k'}{k_o}\sum_S\left(\frac{n(x_s)+\frac{1}{2}\pm\frac{1}{2}}{\omega_S}\right)|g_S(\underset{\sim}{Q})|^2\,\delta(\underset{\sim}{Q}\pm\underset{\sim}{q}-2\pi\underset{\sim}{\tau})\,\delta(\omega\pm\omega_S) \qquad (2)$$

where

$$n(x_S) \quad \frac{1}{\exp(x_S)-1} \qquad \left(x_S = \frac{\hbar\omega_j(q)}{kT}\right) \qquad (3)$$

is the Bose-Einstein population factor (Reif [65])

and

$$g_S(\underset{\sim}{Q}) = \sum_k\frac{\bar{b}_k}{\sqrt{M_k}}(\underset{\sim}{Q}\cdot\underset{\sim}{\xi}(S,k))\exp(i\underset{\sim}{Q}\cdot\underset{\sim}{R}_k)\exp(-W(\underset{\sim}{Q})) \qquad (4)$$

is a modified form of the structure factor for inelastic scattering by a one-phonon process (Bak [64]). In the following we restrict ourselves to this type of process and this limits the validity of the calculation of the line shape to cases where elastic coherent/incoherent and multi-phonon processes can be neglected.

We will assume that the variation of the structure factor throughout the region of reciprocal space within the resolution of the instrument is insignificant and we write

$$g_S(Q) = g_{<S>}(<Q>) \qquad (<S>=<q>,<j>) \qquad (5)$$

i.e. S is taken as the value of q and j of the peak of the measured phonon.

For convenience, we will also assume that the value of the mode S=(q,j) only refers to one branch j. This is no restriction in generality since the final line shape may be obtained by adding the contribution of the different branches in cases where the spacing between the different dispersion surfaces is comparable to the energy resolution of the instrument. Hence the factor of interest in the cross-section is

$$\sum_{q} \frac{k'}{k_o} \frac{(n(x_q)+\frac{1}{2}\pm\frac{1}{2})}{\omega_{\underset{\sim}{q}}} \delta(\underset{\sim}{Q}+\underset{\sim}{q}-2\pi\underset{\sim}{\tau})\,\delta(\omega-\omega_q) \qquad (6)$$

The two delta functions define what we have already called the dispersion surface (sub-section II-3-ii).

In order to carry out the integration in (1), it is necessary to define the geometrical shape of this dispersion surface. An obvious way would to be solve the dynamical matrix for a mesh of points in the region of k-space contained within the resolution of the instrument. By doing this one also gets the polarization vectors as a function of $\underline{q}$; thus one can calculate the exact structure factor as a function of $\underline{q}$ and by numerical integration solve (1). Such a computer programme was written by Dr. E.R. Cowley and proves very useful when the curvature of the dispersion surface is very pronounced (Copley [70]).

Since we are assuming a constant structure factor, this requires that the eigenvectors are very nearly constant and physical intuition tells that this is best verified when there is little mixing between the modes, i.e. when the dispersion surface has a small curvature. Then the $\underset{\sim}{Q}$-dependent dispersion relation can be well approximated as a first order function in $\underset{\sim}{q}$. Hence we may write the frequency expansion as (see II-3-(48))

$$\omega = \omega_o + \underset{\sim}{c}\cdot\delta\underset{\sim}{q} \tag{7}$$

where $\underset{\sim}{c}=\nabla_{\underset{\sim}{q}}\omega\Big|_{q=q_o}$ (the group velocity) and $\frac{\delta q}{q} \ll 1$.

The dispersion surface linear in δq is the most restrictive approximation of this theory. Obviously it breaks down near a reciprocal lattice point but the great advantage over the numberical method is that it allows a much more rapid calculation without any knowledge of atomic force constants.

Since this calculation does not apply to the small wave vector region, we are justified, as a first approximation to assume that the factor

$$\frac{k'}{k_o}\left(\frac{n(x_q)+\frac{1}{2}\pm\frac{1}{2}}{\omega_q}\right) \tag{8}$$

in equation (6) varies but little within the resolution of the instrument. This allows a completely analytical solution to the calculation of the line shape.

However this last approximation may easily be removed by performing numerical integration. We will come back to this point later.

The population factor, or rather the quantity $(n(x)+\frac{1}{2}\pm\frac{1}{2})/x$ which enters into the expression for the cross-section (2), determines the relative merit of performing an experiment under the conditions of phonon creation or phonon annihilation. This comes about from the behaviour of (3) in the limit of large x

$$\lim_{x\to\infty} n(x) \to 0 \qquad \text{(Phonon annihilation)}$$

and $$\lim_{x\to\infty} n(x)+1 \to 1 \qquad \text{(Phonon creation).}$$

Both functions are monotonously decreasing, as illustrated in Fig. II-4-i-1, and it is seen that the situation becomes increasingly more unfavourable for phonon annihilation as the phonon reduced energy becomes larger than 1 (e.g. measurements at low temperature). At the other extreme, i.e. for x<<1, the graph shows that the corresponding curves for phonon creation and phonon annihilation converge into one another; thus at high temperature and/or low phonon energy it is indifferent whether one does the experiment under a process of phonon creation or annihilation. A particularly illuminating discussion on this aspect of quantum statistics is to be found in Feynman [65].

The third function plotted in Fig. II-4-i-1 is related to the energy difference between the true peak position and apparent peak position of transverse phonons and will be discussed in Section II-7.

ii) Calculation of the line shape for phonons other than Λ_t.

We have previously (sub-section II-3-ii) discussed briefly the symmetry property of the energy gradient of phonons measured along a symmetry direction. In the rest of this section we will consider only phonons along directions other than Λ_t, reserving the entire section 5 for the peculiar

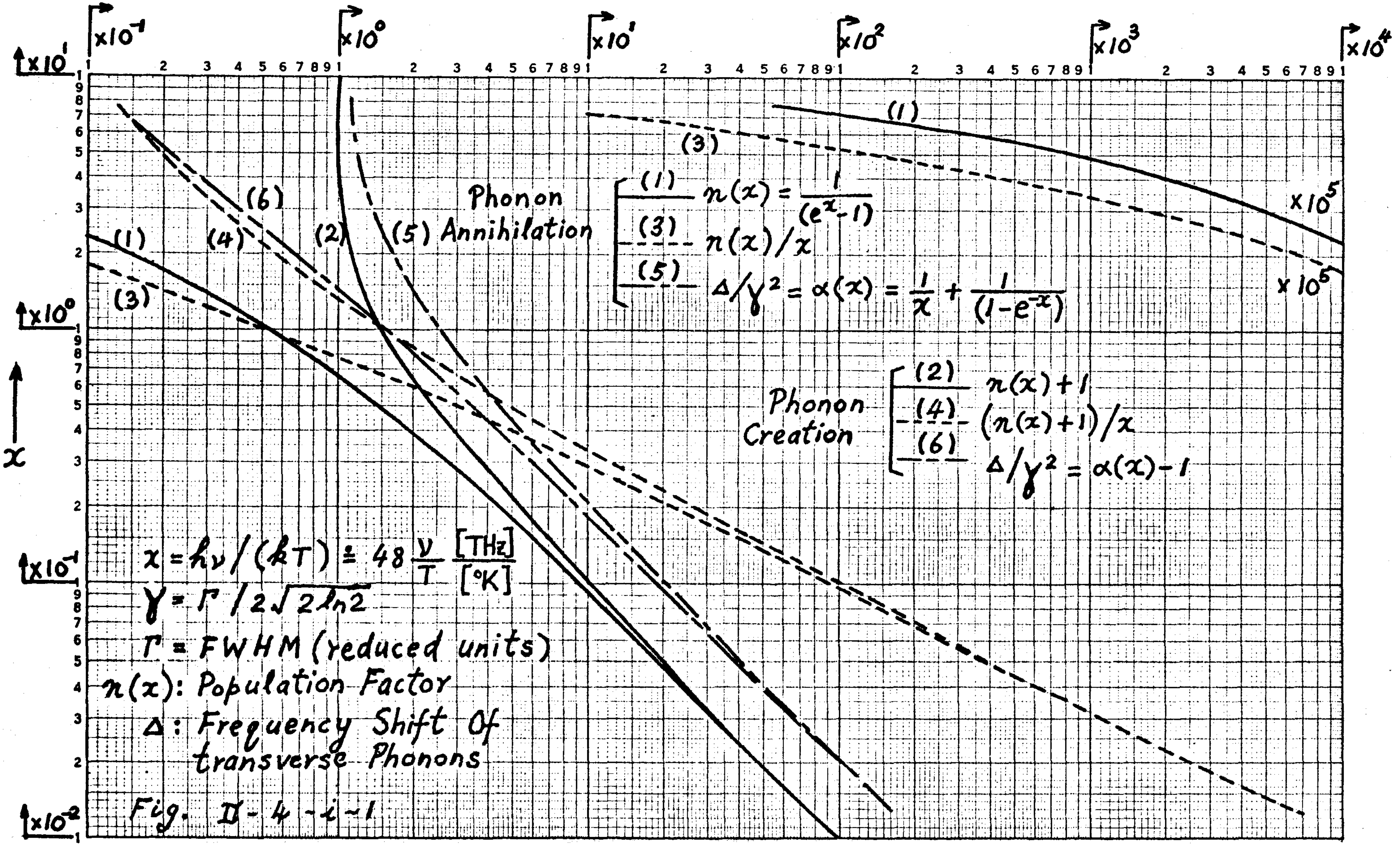
x10^-1
x10^0
x10^1
x10^2
x10^3
x10^4
1 2 3 4 5 6 7 8 9 1
x10^1
x10^0
x10^-1
x10^-2
x
(1)
(2)
(3)
(4)
(5)
(6)
x10^5
Phonon Annihilation
(1) $n(x) = \frac{1}{(e^x - 1)}$
(3) $n(x)/x$
(5) $\Delta/\gamma^2 = \alpha(x) = \frac{1}{x} + \frac{1}{(1-e^{-x})}$
Phonon Creation
(2) $n(x)+1$
(4) $(n(x)+1)/x$
(6) $\Delta/\gamma^2 = \alpha(x) - 1$
$x = h\nu/(kT) \doteq 48\,\frac{\nu}{T}\,\frac{[\mathrm{THz}]}{[^\circ\mathrm{K}]}$
$\gamma = \Gamma / 2\sqrt{2 \ln 2}$
Γ = FWHM (reduced units)
$n(x)$: Population Factor
Δ: Frequency Shift Of transverse Phonons

Fig. II-4-i-1

case of the Λ_t branch.

The expression for the cross-section in equation II-4-(2) explicitly contains the conservation relations of pseudo-momentum and energy and this can be taken into account in the integration II-4-(1) by writing the equation of the dispersion surface as a function of wave vector.

Consider the relative position of the dispersion surface and the resolution ellipsoid as illustrated in Fig. II-4-ii-1. We have to integrate in equation II-4-(1) the resolution function over this surface in order to satisfy the conservation in the delta functions of equation II-4-(2).

We can define ($\Delta\underset{\sim}{Q}_*$, $\Delta\omega_*$) as the separation in $(\underset{\sim}{Q},\omega)$ space between the actual position of the centre of resolution ellipsoid (i.e. point $(\hat{\underset{\sim}{Q}},\hat{\omega})$) and the intersection point of the scan with the dispersion plane(i.e. point $(\langle\underset{\sim}{Q}\rangle,\langle\omega\rangle)$). Hence, the energy difference between any point on the dispersion plane and the energy $\hat{\omega}$ is given (in the planar approximation) by

$$\Delta\omega = (\underset{\sim}{\mathrm{grad}}_Q\,\omega)\bullet(\Delta\underset{\sim}{Q}-\Delta\underset{\sim}{Q}_*) + \Delta\omega_* \qquad (9)$$

This is a function of three variables (the three components of $\Delta\underset{\sim}{Q}$). Physically $\underset{\sim}{\mathrm{grad}}_Q\,\omega$ is the group velocity (c) and we define its three components along (i_Q,j_Q,l_Q) as (c_1,c_2,c_3)

i.e.

$$\underset{\sim}{c} = c_1\underset{\sim}{i}_Q + c_2\underset{\sim}{j}_Q + c_3\underset{\sim}{l}_Q \qquad (10)$$

Hence,

$$\Delta\omega = \underset{\sim}{c}\cdot\Delta\underset{\sim}{Q} - (\underset{\sim}{c}\cdot\Delta\underset{\sim}{Q}_*-\Delta\omega_*) \qquad (11a)$$

a simplification could be introduced by the fact that

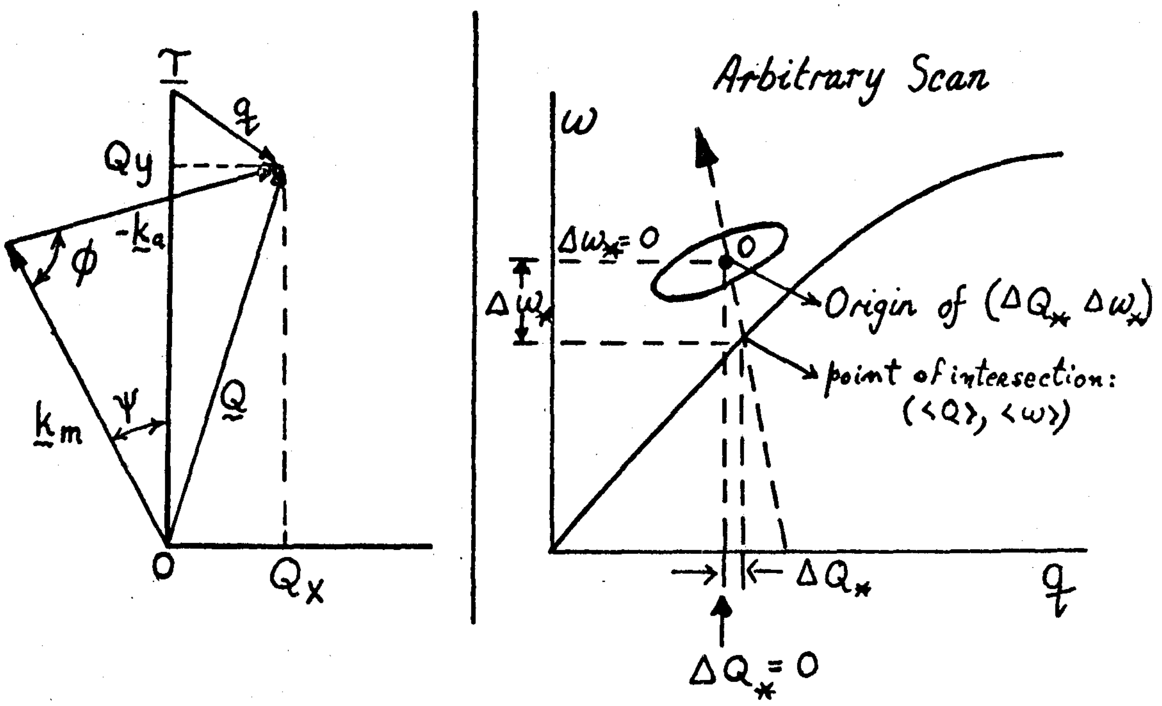

Figure II-4-ii-1: illustration of the relative position of the resolution ellipsoid and the dispersion surface.

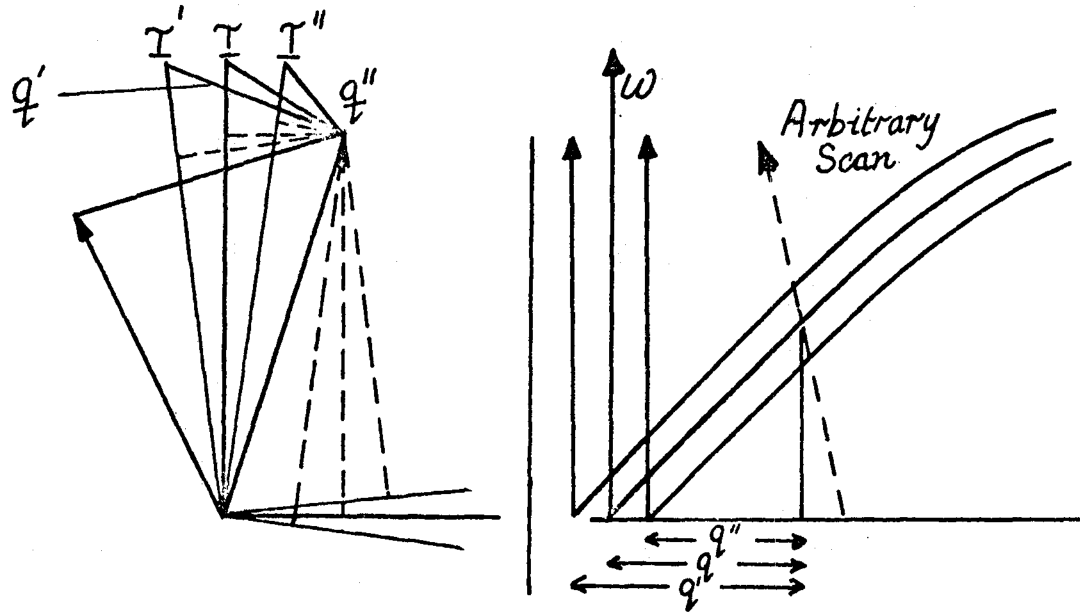

Figure II-6-1: Illustration of the effect of mosaic spread of the specimen on the measured phonon wave vector.

experiments are commonly performed in a symmetry plane of the specimen's reciprocal lattice. In this case the energy dependence as a function of a perpendicular displacement out of the scattering plane is a second order effect and the component c_3 could be put equal to zero. However for the sake of completeness, we will consider the general case; the conclusion is the same as that of Cooper/Nathans if one puts $c_3=0$ in the final solution but the result will allow a calculation of the line shape should experiments be performed out of a mirror plane in a region of reciprocal space where the planar approximation is valid.

Equation (11-a) can be conveniently written as

$$X_4 = c_1X_1 + c_2X_2 + c_3X_3 - W \tag{11b}$$

where

$$W = \underset{\sim}{c}\cdot\Delta\underset{\sim}{Q}_* - \Delta\omega_* \tag{11c}$$

Hence X_4 is a function of (X_1,X_2,X_3) so that the quadruple integration in the general expression II-4-(1) is now reduced to a triple integration.

Hence we may write the

$$\begin{aligned} X^TMX = {} & M_{11}X_1^2 + M_{22}X_2^2 + M_{33}X_3^2 \\ & + M_{44}(c_1X_1 + c_2X_2 + c_3X_3 - W)^2 \\ & + 2M_{12}X_1X_2 \\ & + 2(M_{14}X_1 + M_{24}X_2)(c_1X_1 + c_2X_2 + c_3X_3 - W) \end{aligned} \tag{12a}$$

$$\begin{aligned} = {} & (AX_1^2 + BX_2^2 + CX_3^2) + (DX_1X_2 + EX_1X_3 + FX_2X_3) \\ & + (GX_1 + HX_2 + JX_3) + M_{44}W^2 \end{aligned} \tag{12b}$$

where the following coefficients were used

$$A = M_{11} + c_1^2 M_{44} + 2c_1M_{14} \tag{13a}$$

$$B = M_{22} + c_2^2 M_{44} + 2c_2M_{24} \tag{13b}$$

$$C = M_{33} + c_3^2 M_{44} \tag{13c}$$

$$D = 2(c_1c_2M_{44} + M_{12} + c_2M_{14} + c_1M_{24}) \tag{13d}$$

$$E = 2c_3 \ (c_1M_{44} + M_{14}) \tag{13e}$$

$$F = 2c_3 \ (c_2M_{44} + M_{24}) \tag{13f}$$

$$G = -2W(c_1M_{44} + M_{14}) \tag{13g}$$

$$H = -2W \ (c_2M_{44} + M_{24}) \tag{13h}$$

$$J = -2W \ \ c_3M_{44} \tag{13i}$$

In i) we have discussed the convenience of assuming a constant partial differential cross-section. In this case, the intensity at a given spectrometer setting is proportional to

$$I(\hat{Q},\hat{\omega}) = R_o \iiint dX_1dX_2dX_3 \ \exp(-\tfrac{1}{2}X^TMX) \tag{14}$$

Using(12) and(13) and the result of appendix A-1-iii), this integral may be evaluated analytically to yield:

$$I(\hat{Q},\hat{\omega}) = 4(2\pi)^{3/2} \ \frac{R_o}{\sqrt{\beta}} \ \exp\{-\tfrac{1}{2}[M_{44}W^2 - \tfrac{\alpha}{\beta}]\} \tag{15}$$

where α and β are defined in part iii) of appendix A-1. The remarkable feature of this result is the fact that it predicts a nearly Gaussian line shape. In order to see this, observe that the only coefficients in equation(13) dependent on W are G, H and J. From the form of these coefficients and the result of appendix A-1-iii) we see that these terms only come in the factor α products of pairs, eg. J^2, HJ etc. and hence the dependence of the argument of the exponential on W is quadratic in the general case where the scattering plane is not parallel to a symmetry plane of the specimen's reciprocal lattice.

This can be illustrated if one considers an experiment performed in a symmetry plane which allows us to write $c_3=0$ resulting in a considerable simplification of equation (13) and (A-1-iii-8) for the line shape. In this case equations read

$$E = F = J = 0 \quad (\text{if } c_3=0)$$

Hence

$$\beta = 4(4ABC-D^2C) \tag{16a}$$

$$\alpha = 4(BCG^2 + ACH^2 - CDGH) \tag{16b}$$

and the argument of the exponential function is

$$-\frac{1}{2}\frac{(M_{44}W^2+DGH-AH^2-BG^2)}{4AB-D^2} =$$

$$-\frac{1}{2}\, W^2\{M_{44}+4[D(c_1M_{44}+M_{14})(c_2M_{44}+M_{24})$$
$$- A(c_2M_{44}+M_{24})^2-B(c_1M_{44}+M_{14})^2]\} \tag{17}$$

two remarks:

a) Notice that we have said that the calculated curve is nearly Gaussian. This comes about because of the fact that the coefficients α and β are slowly varying functions throughout the scan since the matrix elements in (6) are themselves functions of the magnitude of the wavevectors and the scattering angles (section II-3). Hence, one cannot rigorously extract the width of the scan from the factor of W^2 in equation (15) and the numerical approach whereby the coefficients α and β are calculated for each instrument setting along the scan proves to be the right procedure.

b) The second remark concerns the mode of scanning independently of any form of focusing. We have seen that the factor governing the intensity distribution along the scan is the quantity

$$W = \underset{\sim}{c}\cdot\Delta\underset{\sim}{Q}_{*} - \Delta\omega_{*} \tag{11c}$$

In an arbitrary scan, both ΔQ_* and $\Delta\omega_*$ are varied. The quantity W varies fastest when $\Delta\underset{\sim}{Q}_*$ and $\Delta\omega_*$ vary in opposite directions if $c>0$ and in the same direction otherwise. This has a simple geometrical interpretation as illustrated in Fig. II-4-ii-2.

In order to take into account the possible error introduced by neglecting the variation of the factor $n(x)/\omega$ in the region of the dispersion surface within the resolution of the instrument, it is necessary to evaluate numerically equation II-4-(1) which now becomes proportionnal to

$$\iiint dX_1 dX_2 dX_3 \, \frac{n(Y)}{\frac{kT}{\hbar}\,Y} \exp\left(-\frac{1}{2} X^T M X\right) \tag{18}$$

where

$$Y = \frac{\hbar}{kT}\left(\langle\omega\rangle + c_1X_1 + c_2X_2 + c_3X_3 - \underset{\sim}{c}\cdot\Delta\underset{\sim}{Q}_{*}\right) \tag{19}$$

and $n(Y)$ is defined by equation II-4-(3).

In using this procedure one must obviously exclude the

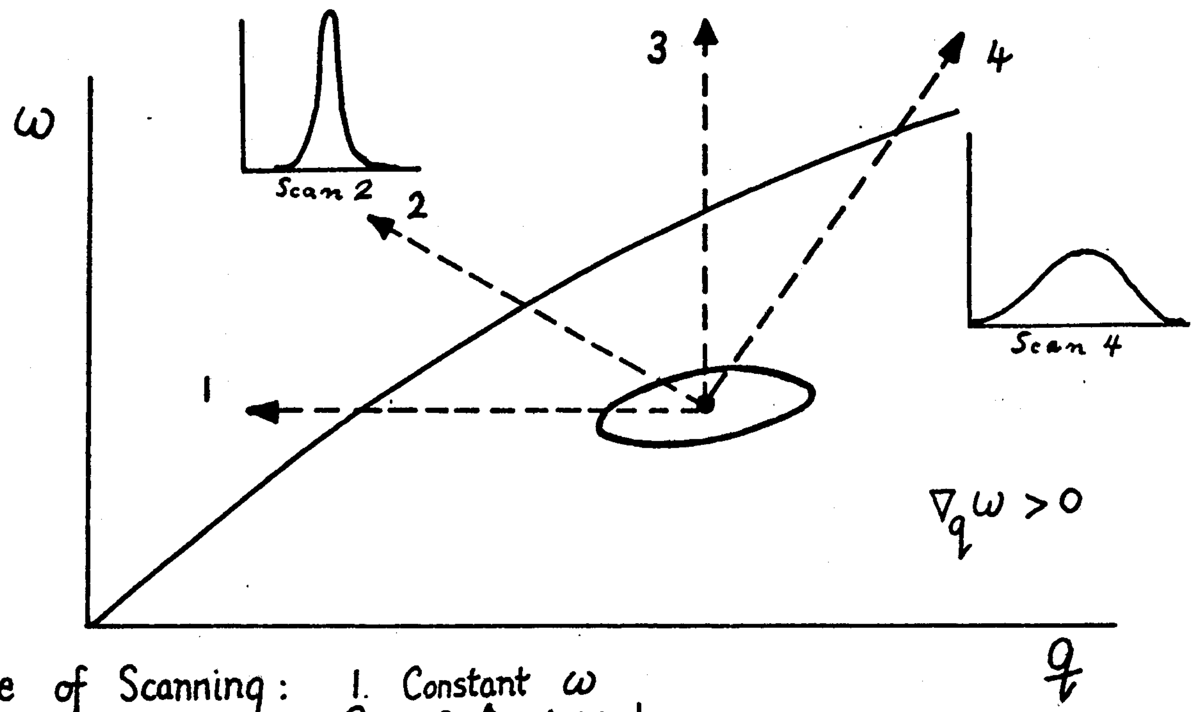

Mode of Scanning :
1. Constant ω
2. $\Delta Q_0 \uparrow$ $\Delta \omega_0 \downarrow$
3. Constant q
4. $\Delta Q_0 \downarrow$ $\Delta \omega_0 \downarrow$

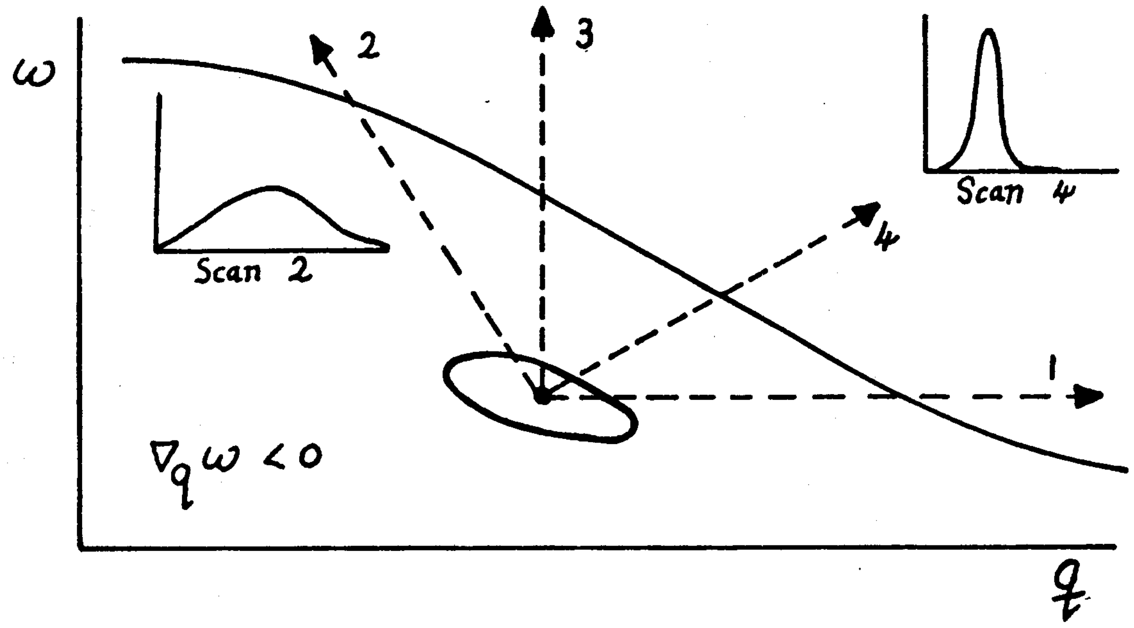

Fig : II - 4 - ii - 2 Different modes of Scanning through the dispersion Surface.

the value Y=0 from the integration. This has no effect on the final result if $(X_1, X_2, X_3, \frac{kTY}{h})$ lies outside of the instrument. If this is not the case, then one is actually detecting a Bragg peak and one must use the appropriate theory. From the form of the expression n(x)/x (See Fig. II-4-i-1), it should be clear that the inclusion of this factor will remove the Gaussian nature of the line shape and at the same time shift the peak position toward lower energies.

II-5- Λ_t Phonons and their unorthodox constant frequency surface.

i) The Λ direction of a cubic lattice (i.e. the $\zeta\zeta\zeta$ direction) shows a peculiar behaviour of the constant frequency surface of phonons of transverse polarization and line shape calculations for Λ_t phonons must be dealt with separately. It turns out that the constant energy surface is a function of the three components of $\underset{\sim}{Q}$ as in the previous case. The difference comes from the functional dependence of this function on the components of $\underset{\sim}{Q}$. Similarly as in the previous section, we will see that the common situation of experiments performed in a symmetry plane in directions other than Λ_t are but a special case of the following treatment.

Consider the case of a crystal with one atom per unit cell. Gilat [69] has shown that the double degeneracy along the Λ direction is removed for displacements perpendicular to the Λ direction and that the constant frequency surfaces form two cones around the (111) direction (i.e. cylindrical symmetry) touching one another at their vertices.

Mathematically, the frequency shift of transverse phonons for a small arbitrary tangential displacement from the Λ direction is given by

$$\delta_{\nu_T} = \pm\frac{\sqrt{6}\ W_\Lambda}{48\pi^2 m\nu_T}\,\eta \qquad (1)$$

where: m is the mass of the atom

ν_T is the transverse phonon frequency on the Λ direction (and of wave vector $\underset{\sim}{q}_\Lambda$)

$\underset{\sim}{\eta}$ is the radial displacement in q-space away from symmetry direction such that the wave vector becomes

$$\underset{\sim}{q} = \underset{\sim}{q}_{\Lambda} + \underset{\sim}{\eta} \quad ; \quad \eta \equiv (\eta_1, \eta_2, \eta_3) \qquad (2a)$$

$$\text{with} \quad \underset{\sim}{q}_{\Lambda} \cdot \underset{\sim}{\eta} = 0 \qquad (2b)$$

$$W_{\Lambda} = \frac{\partial}{\partial \eta_1} D_{11}(q_{\Lambda}) - \frac{\partial}{\partial \eta_1} D_{22}(q_{\Lambda}) + 2\frac{\partial}{\partial \eta_1} D_{23}(q_{\Lambda})$$

$$- 2\frac{\partial}{\partial \eta_1} D_{12}(q_{\Lambda}) \qquad (3)$$

Where $D_{ij}(\underset{\sim}{q}_{\Lambda})$ is the dynamical matrix evaluated at point $\underset{\sim}{q}_{\Lambda}$.

Geometrically, the frequency $\omega(\underset{\sim}{q})$ depends on the parameters $\underset{\sim}{q}_{\Lambda}$ and $\underset{\sim}{\eta}$ so that an iso-frequency surface centered on the point $\underset{\sim}{q}_{\Lambda}$ is defined by the set of wave vectors $\underset{\sim}{q}+\delta\underset{\sim}{q}$ such that $\underset{\sim}{\mathrm{grad}}_q(\omega)\cdot\delta\underset{\sim}{q} = 0$. Because of the conical shape of the constant energy surface, the energy gradient in q-space may be decomposed into two components:

- one along the Λ direction and given by

$$\beta = \frac{\partial}{\partial q_{\Lambda}} \nu_T(q_{\Lambda}) \quad \text{(longitudinal gradient)} \qquad (4a)$$

- another one perpendicular to the Λ direction (i.e. with cylindrical symmetry) and given by equation (1)

$$\alpha = \left.\frac{\partial \nu T}{\partial \eta}\right|_{\eta=0} \quad \text{(tangential gradient)} \qquad (4b)$$

Obviously the previously considered case of the planar dispersion surface in a symmetry scattering plane is a special case of this generalized situation corresponding to putting

$$\alpha = 0$$

In the following, we will consider how this particular topology of the dispersion surface can be taken into account in the calculation of the line shape.

ii) Λ_t phonons and instrumental resolution

The dependence of the dispersion relation frequency on wave vector is given for a small displacement ($\underset{\sim}{\eta}$) in $\underset{\sim}{Q}$-space perpendicular to the Λ direction by

$$\nu_T(\underset{\sim}{q}) = \nu_T(\underset{\sim}{q}_\Lambda) \pm \alpha\eta \tag{5a}$$

where

$$\underset{\sim}{q} = \underset{\sim}{q}_\Lambda + \underset{\sim}{\eta} \qquad (\underset{\sim}{q}_\Lambda \cdot \underset{\sim}{\eta})=0$$

η could be called the radius of the Gilat circle and

$$\alpha = \frac{\sqrt{6}\, W_\Lambda}{48\pi^2 \, M\nu_T} \tag{5b}$$

as was already said.

As in the previous case, the dispersion relation $\omega=\omega(\underset{\sim}{q})$ is implicitly taken into account by expressing the dependence of the frequency in terms of wave vector. We use the same set of axis $\underset{\sim}{i}_Q, \underset{\sim}{j}_Q, \underset{\sim}{l}_Q$ as before to express the energy shift dependence as a function of X_1, X_2, X_3.

In an exactly analogous way, $(\Delta\omega_* - \beta\delta q_\Lambda^o)$ represents the energy separation between the centre of the resolution ellipsoid and its point of intersection with the point $(<\underset{\sim}{q}_\Lambda>, \omega(<\underset{\sim}{q}_\Lambda>))$ on the Λ direction; in a constant-$\underset{\sim}{Q}$ scan, $\delta\underset{\sim}{q}_\Lambda^o = 0$, for exemple.

Define $\Delta\omega$ as the energy separation between the centre of the resolution and the frequency corresponding to the wave vector $<\underset{\sim}{q}_\Lambda> + \delta\underset{\sim}{q}_\Lambda + \underset{\sim}{\eta}$, i.e.

$$\Delta\omega = \Delta\omega_* + \beta(\delta q_\Lambda - \delta q_\Lambda^o) \pm \alpha\eta \tag{6}$$

where $\delta q_\Lambda \parallel \delta q_\Lambda^o \parallel q_\Lambda$ and $\underset{\sim}{\eta} \perp \underset{\sim}{q}_\Lambda$ which is the analog of equation II-4-(9).

In the following, we make two approximations

a) as in the case of the planar dispersion surface, we assume that the dependence of the dispersion relation $\omega(\underset{\sim}{q})$ on wave vector $\underset{\sim}{q}$ is linear in the Λ direction (i.e. the longitudinal energy gradient β is assumed constant in the central region of the resolution ellipsoid).

b) we also assume that the magnitude of the radial energy gradient α which is a functional of dynamical matrix elements is also a constant in that central region.

The relation (2) can now be written in terms of the variables X_1, X_2, X_3 which are a natural choice for performing the integration (II-4-i-1). Refer to Fig. II-5-ii-1 where the scattering plane is parallel with a $(0\bar{1}1)$ plane of the reciprocal lattice.

Evidently, the component of η perpendicular to the scattering plane is

$$\eta_{\perp} = X_3 \tag{7a}$$

The in-plane component of η (i.e. $\eta_{\parallel}$) and the shift along q_{Λ} are related to the vectors $X_1 \underset{\sim}{i}_Q$ and $X_2 \underset{\sim}{j}_Q$ through a rotation of axis

$$\eta_{\parallel} = -X_2 \sin a + X_1 \cos a \tag{7b}$$

$$\delta q_{\Lambda} = X_2 \cos a + X_1 \sin a \tag{7c}$$

where a is the angle between $\underset{\sim}{j}_Q$ and the Λ direction.

Hence equation (6) becomes

$$X_4 = \Delta\omega = -W+\beta(X_2 \cos a + X_1 \sin a) \pm \alpha\{X_3^2+(X_1 \cos a - X_2 \sin a)^2\}^{1/2} \tag{8}$$

where $$W = \beta\delta q_{\Lambda}^{o} - \Delta\omega. \tag{9}$$

The rest now follows by repeating the same procedure as in subsection II-4-ii.

However it is not possible to perform analytic integration and obtain a result equivalent to equation II-4-(15) since the term X_4 contains a square root term and no analog result to that of appendix A-1-iii exists in this case. Numerical integration has to be used.

The validity of this calculation is limited since the eigenvectors do not have simple behaviour except at the zone boundary (fig. II-5-ii-2). However, it illustrates how this particular branch may give rise to double peaks (Cowley [70]) since the double sign in equation (8) effectively results in the observed line shape being the superposition of two peaks, each given by one sign or the other in equation (8). This double peak is more likely to show up above the resolution of the instrument so much the better that the factor α is large ; it disappears completely when $\alpha=0$.

This case where the frequency surface is dependent upon three variables is a more general case of the particular situation previously considered where the energy gradient of a planar dispersion surface was in the scattering plane. This corresponds to putting $\alpha=0$ and equation (8) becomes

$$X_4 = -W+\beta(X_2\cos(a)+X_1\sin(a)) \qquad (10a)$$

$$= -W + C_1X_1 + C_2X_2 \qquad (10b)$$

since

$$\beta \cos a = C_2$$

$$\beta \sin a = C_1$$

which is equivalent with the result of sub-section II-4-ii for the case of a phonon within a mirror plane.

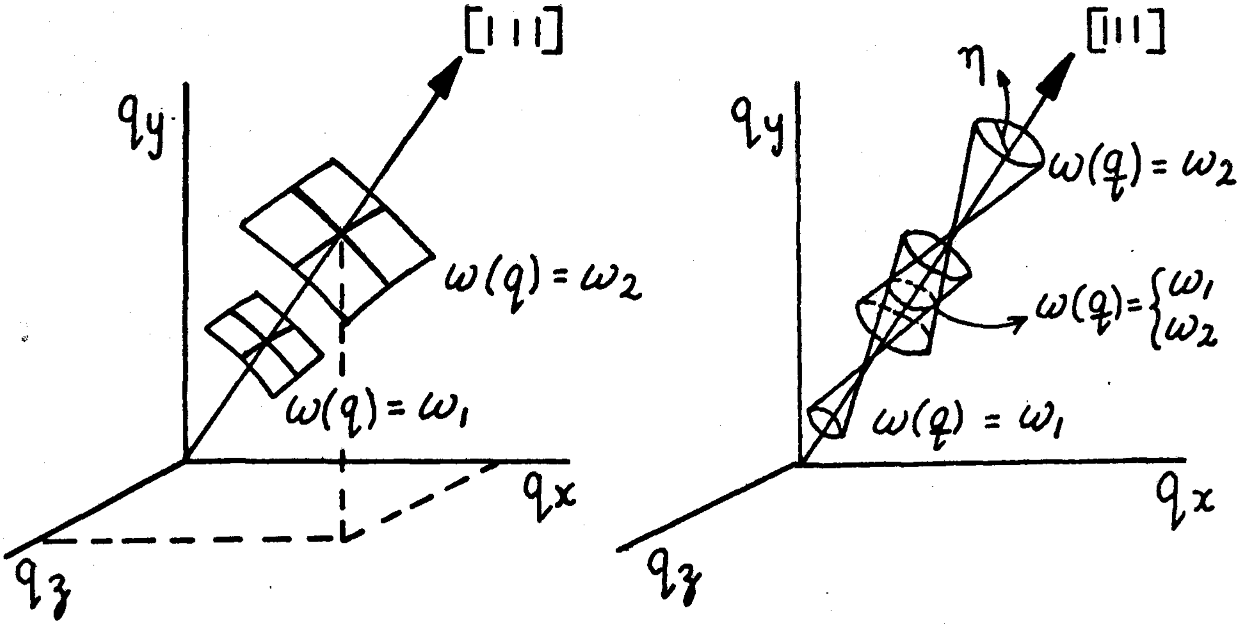

Polarization: Longitudinal, ... Transverse.
Topology of Constant Frequency Surfaces. (exagerated, $\alpha \gg 0$)

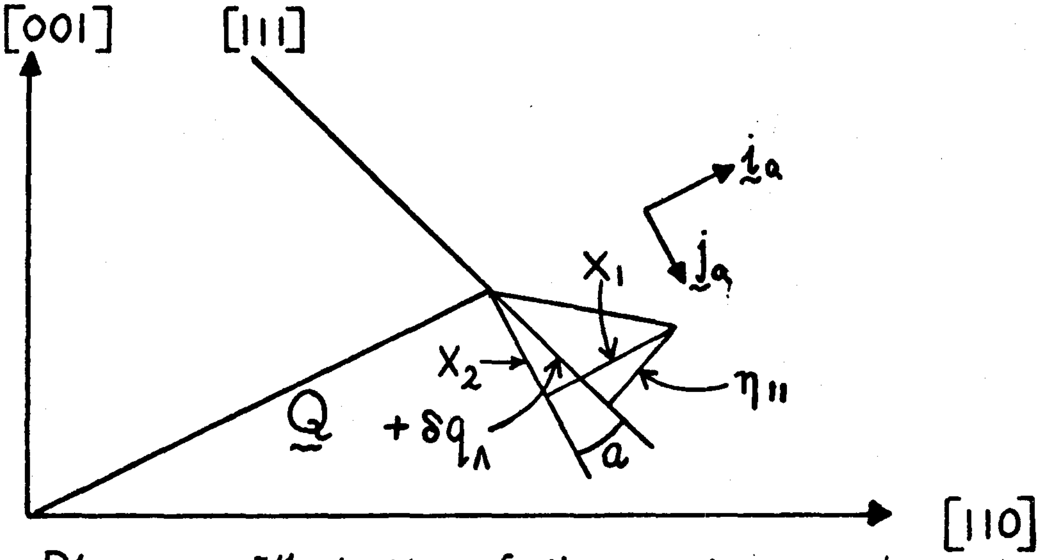

$(0\bar{1}1)$ Plane; Illustration of the vectors components
X_1, X_2, δq_{Λ} and $\eta_{\parallel}$

Fig. II-5-ii-1; Λ Phonons.

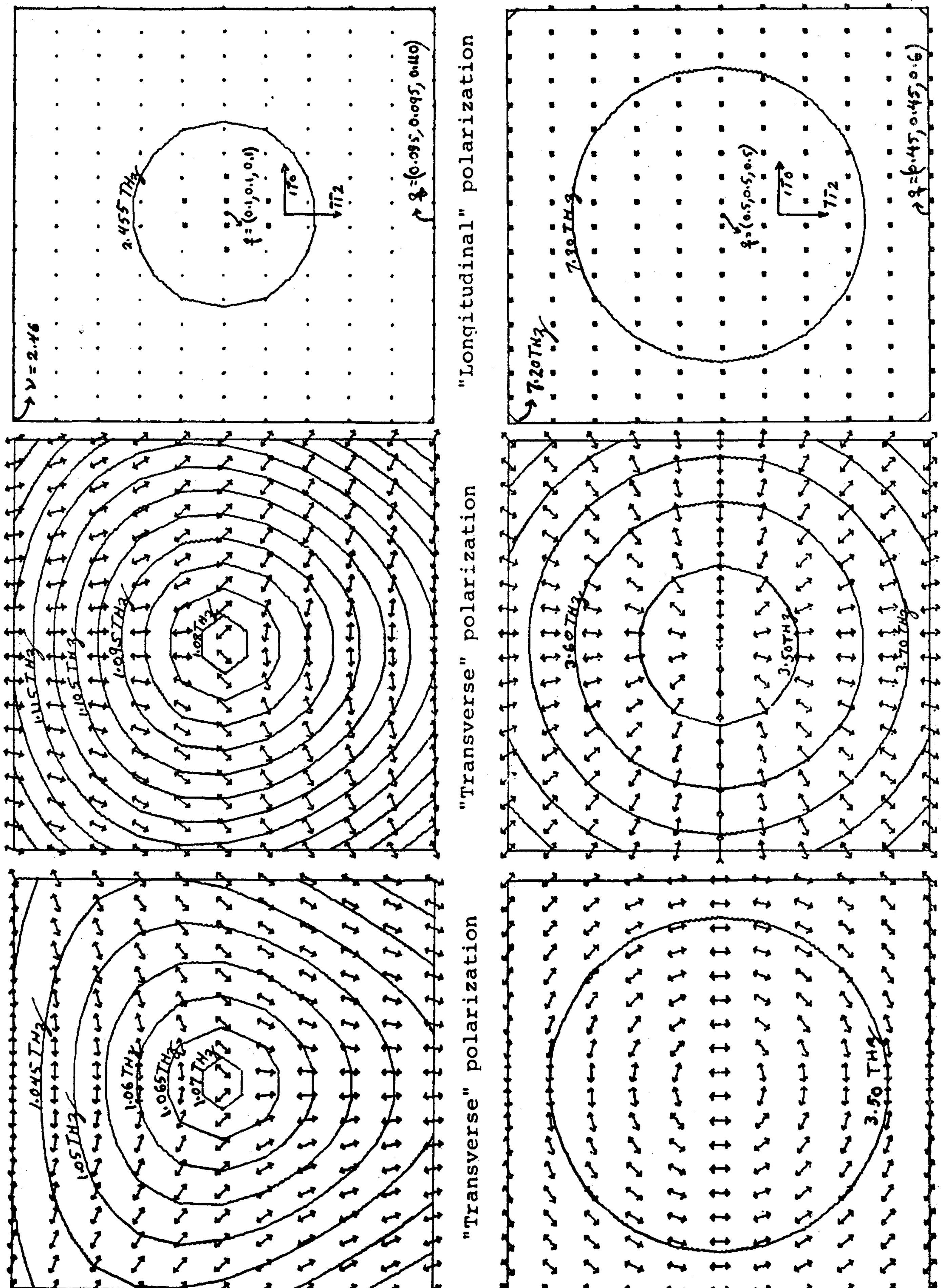

Fig. II-5-ii-2: Calculated constant frequency contours and eigen-vectors in the (111) plane for Cu (FCC structure). The point at the centre of each figure is $\underset{\sim}{q}$=(0.1,0.1,0.1) on the left hand side and $\underset{\sim}{q}$=(0.5,0.5,0.5)

II-6. Effect of the mosaic spread of the specimen on the calculated line shape.

The previous considerations dealt with the case of a perfect crystal in which case the value of the momentum transfer $\underset{\sim}{Q}$ corresponds to a well defined point in the reciprocal lattice of the specimen. However, no crystal actually fits the idealized mathematical picture of a lattice of absolute periodicity.

Suffice to say that real crystals are actually a composite mosaic of micro-crystals which are themselves perfect and are distributed preferentially along the macro-crystal axes. This mosaic distribution has consequences in both elastic (see for example Appendix A-3) and in inelastic scattering. For our present considerations, we may vizualize the effect as a radial smearing of reciprocal space since the mosaic structure, by itself, only affects the orientation of the crystallites and not their plane spacing. We will limit ourselves to considerations of the "smearing" in the scattering plane since the out of the plane component is expected to play a minor role in any crystal with small enough mosaic spread to be usable.

Similarly as the relative orientation between different crystallites varies, so does their respective vectors defining reciprocal space. Hence, a given wave vector has a different orientation in reciprocal space depending on which set of reciprocal space basis vectors if is refered to.

How does this affect the general expression [equation II-4-(15)] for the line shape? This expression is a function of W, α, β and the matrix $\left(M_{rs}\right)$. This matrix is obviously independent of the mosaic spread of the specimen (see section II-3). The terms α and β are functions of the different components of the group velocity [see equations II-4-(13)]; in principle, these components vary since they are defined along the $\underset{\sim}{Q}$-dependent unit vectors $\underset{\sim}{i}_Q$, $\underset{\sim}{j}_Q$ and $\underset{\sim}{l}_Q$. One can easily take this variation into account by adopting a numerical procedure but we will use the fact that a mosaic distribution is at most a few degrees wide in order to assume that the factors α and β are not significantly affected by the mosaic structure and can be taken equal to their central values.

Hence, the main contribution to the line shape from the crystallites distribution comes from the factor W defined by equation II-4-(11) as:

$$W = \underset{\sim}{c} \cdot \Delta \underset{\sim}{Q}_* - \Delta \omega_* \qquad (1)$$

This object was already illustrated in figure II-4-ii-1. Both of the terms $\Delta \underset{\sim}{Q}_*$ and $\Delta \omega_*$ are affected by the mosaic spread. Refer to figure II-6-1* which illustrates a projection of the dispersion surface on the $(\nabla_{\underset{\sim}{q}} \omega, \omega)$ plane. Qualitativly, we see that mosaic spread results in the observed line shape being the superposition of individual neutron groups contributed by each of the crystallites; the smearing of the dispersion curve is increased so much the better that the energy q-gradient of the phonon lies perpendicular to $\underset{\sim}{Q}$ (and in the scattering

*NOTE: figure II-6-1 is on page 60.

plane). In any case, we can say that, in general, the instrumental resolution intersects a "dispersion volume" instead of a surface.

Define $\Delta Q_{\parallel}$ as the component of $(Q\eta)$ parallel to $\underset{\sim}{\nabla}_q \omega$, i.e.

$$\Delta Q_{\parallel} = Q\eta\cos(b) \tag{2}$$

where η corresponds to a particular orientation of mosaic blocks and where b is the central angle between the unit vector $\underset{\sim}{j}_Q$ (see section II-3) and the energy q-gradient. W is a function of η, the angular "smearing" in the scattering plane, and we may write

$$W'(\eta) = c\Delta Q_{\parallel} - \Delta\omega_{*} \tag{3a}$$

$$= C\eta - \Delta\omega_{*} \tag{3b}$$

where

$$C = cQ\cos(b) \tag{4}$$

if we assume a constant-$\underset{\sim}{Q}$ scan for simplicity (i.e. $\underset{\sim}{\Delta Q}_{*}=0$); the generalization is straightforward in the case of an arbitrary scan and is not needed if a numerical calculation is carried out.

We have seen that the general expression II-4-(15) for the intensity distribution is very nearly a gaussian function and may be written as proportional to:

$$I(\hat{\underset{\sim}{Q}},\hat{\omega}) = \frac{1}{\sqrt{\beta}} \exp[-\tfrac{1}{2}\Xi W^2] \tag{5}$$

where Ξ is a complicated function of the instrumental parameters and settings. In the case now under consideration (i.e. constant-$\underset{\sim}{Q}$ scan in an arbitrary plane), the calculated intensity distribution is obtained by integrating the contribution of all the crystallites distributed according to the function $W(\eta)$, i.e.

$$I'(\hat{\underset{\sim}{Q}},\hat{\omega}) = \int_{-\infty}^{\infty} d\eta\, W(\eta)\, \frac{\exp[-\tfrac{1}{2}\Xi(W'(\eta))^2]}{\sqrt{\beta}} \tag{6}$$

Again, the mathematically convenient limits of $(-\infty,+\infty)$ were used instead of the physical ones $(-\pi,+\pi)$. If the mosaic distribution is gaussian, as in equation II-2-(11) , then we have

$$I'(\underset{\sim}{\hat{Q}},\hat{\omega}) = \frac{\exp[-\frac{1}{2}\Xi'(\Delta\omega_*)^2]}{\sqrt{2\pi\beta}\,\sigma} \int_{-\infty}^{\infty} d\eta \, \exp\left[-\frac{1}{2}\left\{\eta^2\left(\frac{1}{\sigma^2} + C^2\Xi'\right) - 2C\Delta\omega_*\Xi'\eta\right\}\right] \tag{7}$$

Using the result of Appendix A-1, this gives

$$I'(\underset{\sim}{\hat{Q}},\hat{\omega}) = \frac{1}{\sqrt{\beta(1+\sigma^2C^2\Xi')}} \exp\left[-\frac{1}{2}\Xi'(\Delta\omega_*)^2 \left\{\frac{1}{1+\sigma^2C^2\Xi'}\right\}\right] \tag{8}$$

where C is defined by equation (4). We repeat that the validity of the result (8) is limited to a constant-$\underset{\sim}{Q}$ scan.

We see that the line shape, as previously, has a nearly gaussian structure. Its width, however, is now larger by the factor

$$\sqrt{1+\sigma^2C^2\Xi'} \tag{9}$$

a quantity which is always greater or equal to unity since the term Ξ' is itself positive as can be seen simply by observing that a physical situation with a well defined peak corresponds to a positive Ξ' in the expression (5). Equation (8) illustrates the fact that the neutron group is narrowest (for a given constant-$\underset{\sim}{Q}$ scan) when the mosaic spread is small ($\sigma \to 0$) and/or the energy q-gradient of the excitation is parallel to $\underset{\sim}{Q}$ ($C = 0$; see equation (4)). This ideal situation corresponds to an identical result as that given by equation (5).

Observing that the term Ξ' corresponds to the inverse of the width in the case where there is no mosaic spread present (equation (5)), then we get the expression for the increased width (at $1/\exp[\frac{-1}{2}]$)

$$2\gamma_* = 2(\gamma^2 + \sigma^2C^2)^{1/2} \; ; \quad \gamma^2 = 1/\Xi' \tag{10}$$

an intuitivly acceptable result.

II-7. Correction on apparent peak position because of the composite effect of the population factor and the widening of the neutron groups.

The previously derived expression for the widening of a neutron group [equation II-6-(10)] is valid so much the better that the correction is small. Such is not the case for phonons of transverse polarization measured on a bad specimen and the widening may be large enough so that a correction for the effect of the population factor needs to be made. We will now derive the expression for this correction, pointing out immmediatly that it is valid so much the better that the widening is large compared with a similar phonon measured on a good crystal.

The expression for the cross-section of a one-phonon process contains a term of the form $(n(x)+\frac{1}{2}\pm\frac{1}{2})/x$, where $n(x)$ is the population factor at the reduced energy x [equation II-4-(2)]. Refering to figure II-4-i-1, it is seen that the functions $n(x)/x$ and $(n(x)+1)/x$ are monotonically decreasing functions; consequently, the presence of this term in the cross-section formula is to give more weight to the low energies. Rigorously, this should be taken into account in the expression for the line shape, but this is only possible if one uses a numerical procedure to evaluate the intensity distribution [equation II-4-(18)] . In what follows, we derive an expression to take into account the fact that the different sections of the"dispersion volume" intersected during a scan have different cross-sections. Obviously, this derivation is only valid if the mosaic spread of the specimen results in a much larger width than that of the resolution of the instrument alone.

The effect of the terms n(x)/x and (n(x)+1)/x on the peak position of groups widened by mosaic spread is estimated in the following way. We write these two terms as a single one

$$G(x) = \left[\frac{1}{(\exp(x) - 1)} + \frac{1}{2} \pm \frac{1}{2}\right]/x \qquad (1)$$

where x stands for the reduced energy ($h\nu/(kT)$) and the $\genfrac{}{}{0pt}{}{\text{(upper)}}{\text{(lower)}}$ signs are to be used for phonon $\genfrac{}{}{0pt}{}{\text{(creation }\quad)}{\text{(annihilation)}}$.

Let the line shape, undistorted by the function G(x) and including the widening caused by mosaic spread, be of the form

$$F(x) = A \exp\left[\frac{1}{2}\left(\frac{\delta}{\gamma}\right)^2\right] \quad ; \quad \delta = x - \langle x \rangle \qquad (2)$$

(a gaussian line shape will be assumed for the rest of this subsection). Let the measured line shape be of the form

$$F_*(x) = A_* \exp\left[\frac{1}{2}\left(\frac{\delta_*}{\gamma_*}\right)^2\right] \quad ; \quad \delta_* = x - \langle x_* \rangle \qquad (3)$$

$\langle x \rangle$ is the peak position of the undistorted curve and $\langle x_* \rangle$ is the peak position of the measured curve. γ and γ_* are the standard deviations of the groups and are related to the FWHM by equation II-1-(8).

Define $\Delta = \langle x \rangle - \langle x_* \rangle$ as the shift between the undistorted and the measured peak central positions. The observed intensity at an energy setting x is approximatly

$$F_*(x) = F(x)G(x) \qquad (4a)$$

$$= A \exp\left[\frac{-1}{2}\left(\frac{\delta}{\gamma}\right)^2\right] \left(\frac{1}{\exp(x) - 1} + \frac{1}{2} \pm \frac{1}{2}\right)/x \qquad (4b)$$

Equating to zero the derivative of this object with respect to x gives the position of maximum intensity of the observed groups. The result is

$$\frac{dF_*(x)}{dx} = \frac{A}{x}\exp\left[\frac{-1}{2}\left(\frac{\delta}{\gamma}\right)^2\right]\left[\frac{1}{(\exp(x)-1)(\exp(-x)-1)} - \left(\frac{\delta}{\gamma^2}+\frac{1}{x}\right)\left(\frac{1}{\exp(x)-1}+\frac{1}{2}\pm\frac{1}{2}\right)\right] \tag{5}$$

This is equal to zero if either $\delta \to \pm\infty$ (trivial case) or if the expression in square brackets is equal to zero. This is true when $x = \langle x_* \rangle$

Then, $$\delta = x - \langle x \rangle = \langle x_* \rangle - \langle x \rangle = -\Delta \tag{6}$$

and $$\Delta = \gamma^2\left\{\frac{1}{x} - \left[\frac{1}{(\exp(x)-1)(\exp(-x)-1)}\right] \Big/ \left[\frac{1}{\exp(x)-1}+\frac{1}{2}\pm\frac{1}{2}\right]\right\} \tag{7}$$

where x is understood to be equal to $\langle x_* \rangle$. We make the approximation that the distortion does not significantly change the width of the group, i.e. $\gamma = \gamma_*$.

The general expression (7) may be simplified:

a) For phonon annihilation

$$\Bigg\| \; \Delta = \gamma^2\left[\frac{1}{x} + \frac{1}{1-\exp(-x)}\right] \tag{8}$$

if $x \ll 1$, $\Delta \to 2\gamma^2/x$ (in reduced units) or (9a)

$\Delta(\mathrm{THz}) \to 0.362\Gamma^2/\nu$ (in THz); (Γ : FWHM) (9b)

if $x \gg 1$, $\Delta \to \gamma^2$ (in reduced units) or (10a)

$\Delta(\mathrm{THz}) \to 8.7\Gamma^2[\mathrm{THz}]/T[^\circ\mathrm{K}]$ (Γ : FWHM) (10b)

b) For phonon creation

$$\Bigg\| \; \Delta = \gamma^2\left[\frac{1}{x} + \frac{1}{\exp(x)-1}\right] \tag{11}$$

if $x \ll 1$, $\Delta \to 2\gamma^2/x$ (in reduced units) or

$\Delta(\mathrm{THz}) \to 0.362\Gamma^2/\nu$ (in THz) (Γ : FWHM) (12a)

if $x \gg 1$, $\Delta \to 0$ (12b)

Thus, for low energies, the shift is the same for both phonon creation and phonon annihilation. For high energies, the shift for phonon creation tends to zero while, for phonon annihilation, it is temperature dependent.

Obviously, the above considerations do not apply if the shift Δ is of similar magnitude as to the energy itself, i.e. $\Delta \sim x$. The condition for $\Delta \ll x$ is found to be

$$\Gamma / \gamma \ll 1.6 \tag{13}$$

Figure II-4-i-1 illustrates the behaviour of the frequency shift as a function of the reduced energy for the cases of neutron energy loss and neutron energy gain. To apply this correction, one should properly use for Γ the true width of the group, i.e. after correction for instrumental width. However, the validity of this correction is limited to the case where the widening is at least comparable in magnitude to the instrumental width so that one can use the uncorrected width in the case of a bad specimen.

III-Crystal dynamics of a disordered alloy: $Cu_{.63}Ni_{.21}Zn_{.16}$

1) Introduction

We now come to the experimental section dealing with the measurements of the phonon spectrum of a disordered ternary alloy of Cu-Ni-Zn. The description of the equipment or the procedure adopted for the measurements will be avoided here since it has been carried out elsewhere by very qualified people (Rowe [66], Brockhouse [68], Hallman [69]).

The recent years have seen work demonstrating the strong influence on the phonon spectrum of metals by the existence of long-range interaction between ions, as in lead (Brockhouse [62]), white tin (Rowe [65]) and zinc (Maliszewski [63]). The study of these complicated metals has brought forward the necessity of taking proper account of electron-phonon interaction. This interaction is always present but the fact of the matter is that the comparative simplicity of the dispersion curves in the case of simple metals like copper and the alloy studied here always permits a description in terms of a short-range interaction with a limited number of interacting neighbours. An excellent recent review article on the subject is to be found in Yu. Kagan [68].

The experiment here described is a logical extension of the work of Hallman [69] on binary solutions of copper where the dependence of the phonon spectrum on electron concentration had been studied in iron-group alloys and our aim was to measure the phonon spectrum of a solid having the same electron concentration as pure copper. The choice of a ternary composition afforded the possibility to obtain a compensated system with a average electron concentration per atom equal to that of pure copper (and with the unavoidable mass disorder). This effect of local mass variation may be minimized to that found in an homogeneous copper specimen from isotopic mass variation by choosing the components of the ternary to be neighbours of copper in the periodic table i.e. nickel and zinc, as was done here. The electronic structure of these three elements is given in Table III-1-(1) and is self explanatory; obviously the average electron concentration per atom will be equal to that of copper if equal atomic concentrations of nickel and zinc are alloyed with the copper.

The particular specimen used had a nominal concentration of 60 at.% for copper and 20 at.% for both nickel and zinc; it was verified by chemical analysis (see next sub-section) that these values were inexact and that the crystal had an electronic concentration per atom 0.95 that of pure Cu.

Hallman had measured the phonon spectrum of $Cu_{.5}Ni_{.5}$ and $Cu_{.75}Zn_{.25}$ and found that their respective average frequency ratios relative to pure copper were 1.107 ± 0.009 and 0.934 ± 0.003 illustrating how the frequencies are inversely related to electron concentration. However in our case the departure from the compensated value of electron concentration is much smaller and the Lindemann criterion defined as

$$\frac{\nu_A}{\nu_B} = [(\frac{T_A}{a_A^2 M_A}) / (\frac{T_B}{a_B^2 M_B})]^{1/2}$$

predicts an average frequency ratio

$$\frac{\nu_X}{\nu_{Cu}} = 1.025$$

using the melting temperatures (T_X), lattice parameters (a_X) and atomic masses (M_X) listed in Table III-1-(1).

This frequency shift is in the same direction as that predicted from the results of Hallman. However, the relative change in frequency lies at the limit of precision of the technique of thermal neutron scattering so that one does not expect any detectable shifts relative to the copper spectrum as measured by Svensson [67].

Table III-1-(1)-a;

Relevant physical quantities for the transition elements Cu, Ni and Zn.

		Cu	Ni	Zn
Z (atomic number)		29	28	30
A (atomic mass in a.m.u.)		63.54	58.71	65.38
Crystal structure (20°C.)		F.C.C.	F.C.C.	H.C.P.
a (lattice parameter:20°C.)		3.6147A	3.52A	2.66A,4.95A
T_m (melting temperature)		1356°K	1728	692
θ_D (Debye temperature)		345°K	476°K	-
θ_C (Curie temperature)		-	635°K	-
Neutron scattering cross-sections: (x $10^{-24}cm^2$)	$\sigma_{coh.}$	7.25	13.2	4.1
	$\sigma_{inc.}$	0.6	4.8	
	$\sigma_{abs.}$	3.8	4.6	1.1

Electron configurations and term type for the ground state

	1s	2s	2p	3s	3p	3d	4s	
Ni	2	2	6	2	6	8	2	$^3F_4$
Cu	2	2	6	2	6	10	1	$^2S_{1/2}$
Zn	2	2	6	2	6	10	2	$^1S_0$

* * * * * * * * * * * *

Table III-1-(1)-b; Properties of the Cu-Ni-Zn specimen.

Chemical composition: [Ni]: 20.67±0.5 at%;
[Cu]: 63.47±0.5 at%;
[Zn]: 15.86±1.0 at%.

Lattice parameter: 3.6229 ± 0.006 A

Melting temperature: circa 1400°K.

Average atomic mass: 62.83 a.m.u.

Dimensions: 6mm. dia. x 10 cm. long.

III-2 Chemical composition of the specimen.

i) The composition of the ternary was measured by performing a chemical analysis on a 2 gram portion coming from one extremity of the crystal which was a cylinder 6 mm. in diameter and 10 cm. long. At the time this was done, it was not thought of to repeat the procedure on a portion coming from the other extremity of the crystal; this would have supplied an indication as to chemical homogeneity. However, measurements of the lattice parameter afforded an estimate of the degree of inhomogeneity averaged over the whole crystal (cf. III-4).

The chemical separation of the three elements was performed using the technique of anion exchange and their concentrations were determined by EDTA (ethylenedinitrilo-tetraacetic acid) titration. The next sub-section (ii) is concerned with a description of the experimental chemical procedure and the result of this analysis is to be found in sub-section (iii).

ii) Chemical analysis

The experimental procedure for this type of analysis is fairly well known [Jones-59, Welcher-58]; it is illustrated in block diagram in fig. III-2-ii-1 and will be briefly described.

A portion of the specimen weighting 1.95110 gr. was dissolved by warming in concentrated HCl and then diluted to 6N HCl, resulting in a solution containing the following ions: Ni^{++}, $[CuCl_4]^{--}$ and $[ZnCl_4]^{--}$.

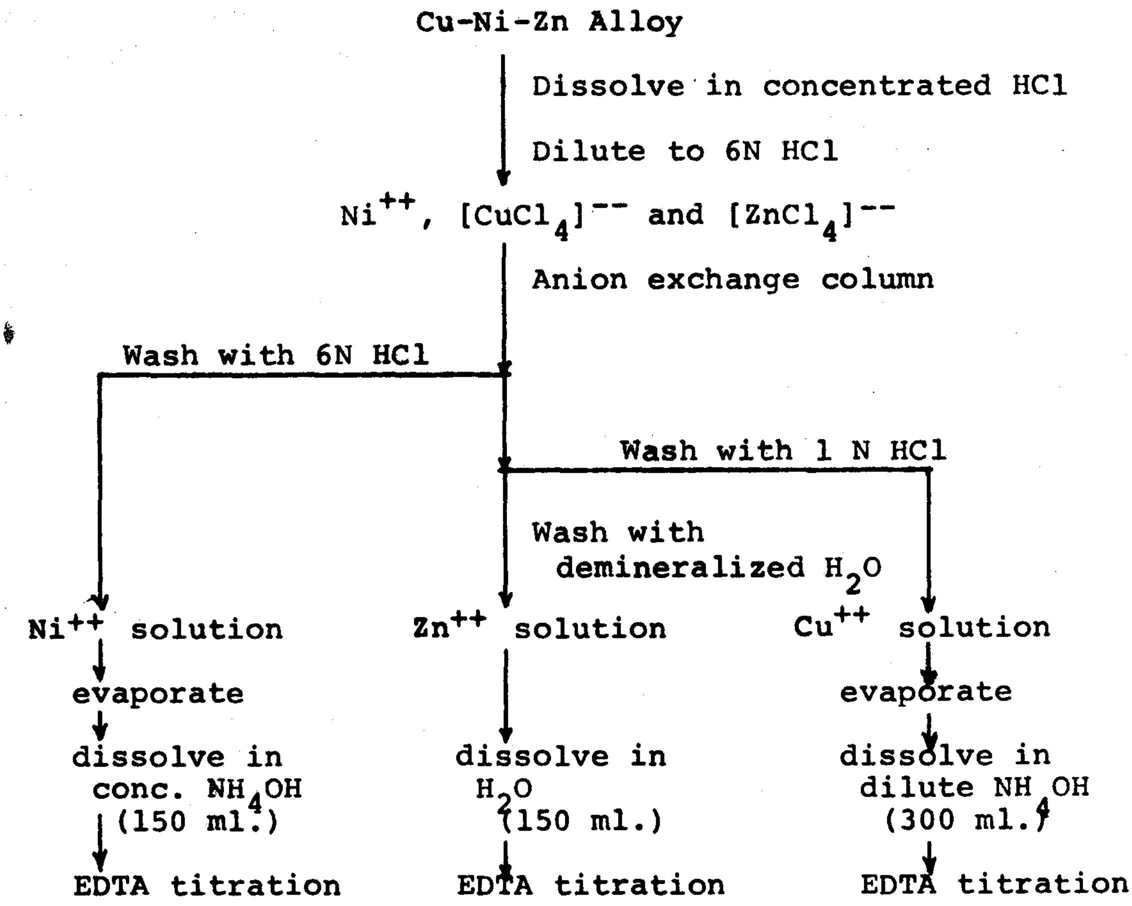

Fig. III-2-ii-1 Block diagram of the chemical procedure for separating the constituents of the alloy.

The principle behind the technique of anion exchange, as the name indicates, is that anions in the solution flowing through the separating column are trapped by the resin packed in this column while the cations are allowed to flow through freely. Consider the particular case of the ternary for exemple. In a 6N HCl solution, Ni is a cation while Cu and Zn react with the Cl ion to form an anion; in 1N HCl, the Cu becomes in turn a cation while the Zn is unaffected and in 0.01N HCl, all three elements are cations.

Thus when the 6N HCl solution containing the dissolved alloy is allowed to flow in the column, the Ni goes through practically unhindered and can be collected. Similarly, washing with 1N HCl liberates the Cu by transforming it to a cation leaving behind only the Zn fraction which may be eluded using 0.01N HCl or plain H_2O.

Obviously the efficiency of the separation depends upon maximizing the ratio surface/volume of the resin making up the column. A resin like Dowex 1-X8, 100-200 mesh, was found to give satisfactory results as compared with the coarser grade 20-50 which did not allow the separation to take place within the length of the column(~30 cm.).

EDTA was used in all three titrations. The indicator used for Ni and Cu was Murexide and that used for Zn was Eriochrome Black T. The solutions containing the Ni and Cu fractions were evaporated to dryness before titration since the Murexide indicator has to be used in a non-acid solution and neutralization would have resulted in the formation of ammonium salts which are particularly deleterious to this indicator. The Ni precipitate was redissolved in concentrated NH_4OH while 4N NH_4OH was used for the Cu precipitate. The Zn fraction did not need to be evaporated since a different indicator was used.

The titration itself was straightforward except in the case of the Zn fraction where, for a yet unexplained reason, no well defined end-point could be observed; a test solution prepared from Zn powder showed no such problem. The Zn concentration was ultimately obtained by subtracting the other two concentrations from unity; this was later justified by doing a qualitative spectroscopic analysis to verify the absence of any other element in any significant concentration.

iii) Results of the titrations are as follows:

[Ni] : 20.67 at.% ± 0.5
[Cu] : 63.47 at.% ± 0.5
[Zn] : 15.86 at.% ± 1.0

This is to be compared with the nominal concentration given as $Cu_{.60}Ni_{.20}Zn_{.20}$. The imbalance between the Ni and Zn concentrations results in the ternary having an electron concentration per atom of 0.95 as compared with 1.0 for Cu.

III-3 Crystallite distribution

Normally there is nothing interesting under this heading, the usual figure of merit of a crystal being the width at half maximum of its mosaic block distribution; it is usually a number smaller than one degree and the perfection of the specimen crystal is a desirable feature in neutron scattering as well as in other branches of solid state physics to make the interpretation of the measurements unambiguous.

A picture of the mosaic distribution may be obtained by rocking the specimen around its orientation for Bragg scattering leaving the scattering angle fixed and the intensity distribution thus obtained is a convolution of the instrumental resolution and the mosaic distribution function.

This function is customarily assumed to be Gaussian in the case where the crystal is relatively good. The convolution of this function with the resolution function of the instrument gives the observed Gaussian line shape and its width is given by the R.M.S. of the widths of the distribution and the resolution function.

The contribution of the mosaic distribution function becomes more prominent **and more similar** to that of the observed intensity distribution when its width becomes superior to the resolution of the instrument.

Such is the case with the particular specimen used here. Fig. III-3-1 illustrates the observed intensity from the four main (200) reflections while the crystal (001) planes were parallel to the scattering plane. Two points first strike the observer. Firstly, the effective width of each distribution varies between 2 and 3 degrees. This is much wider than the contribution from instrumental resolution which may be estimated to be a fraction of a degree using a perfect crystal on the specimen table. This means that resolution introduces but a small correction to the widths of the observed intensity and we may safely assume the above intensity distribution to be faithful representation of the crystallite distribution.

The second point to observe is that the crystal is obviously non-single. Not only is this evident from these intensity distribution curves but also it was possible to observe low intensity parasitic reflections at random positions between the main reflections. This occured in both the (001) and ($0\bar{1}1$) scattering planes used.

This demonstrates the imperfection of our specimen and will be a limiting factor in the accuracy of the measurements of phonons to be described later since the observed intensities are necessarily coming from a smeared out region of reciprocal space. Nevertheless we will use the theory of Chapter II to determine how much this effect contributes to the widening of the lineshapes.

It seems to be a common instance that it is difficult to obtain a good crystal of copper with nickel and zinc. For example, another alloy of nominal concentration $Cu_{.50}Ni_{.25}Zn_{.25}$ also showed a similarly unfavorable mosaic distribution. The two specimens of $Cu_{.5}Ni_{.5}$ and $Cu_{.75}Zn_{.25}$

studied by Hallman and previously referred to also were among his worst crystals having a FWHM of 96' and 66'. From the phase diagram Fig. III-3-2, we see that the particular composition of the ternary specimen and that of Hallman's specimens correspond to a region well within the FCC phase indicating that this difficulty is encountered over a wide range of concentrations in this phase.

After the phonons measurements were completed, it was attempted to anneal the crystal to see if the mosaic distribution could be improved. According to the liquidus diagram of Fig. III-3-1, the melting temperature lies above 1100°C, slightly above that of pure copper. The annealing treatment consisted as follows: the crystal was enclosed in a heat resistant steel pipe which was sealed under an argon atmosphere and contained zinc powder in order to have a high vapour pressure of this element and thereby minimizing the possibility of depletion of the zinc content while the crystal was at high temperature. The treatment consisted in keeping this arrangement during one week at a temperature of 800°C and then gradually cooling down to room temperature over a 3 day period.

This procedure proved to be satisfactory. Although the outside of the pipe was badly corroded, the crystal seemed to have been totally unaffected except for some localized change to a brass-like color (as compared with the initial greyish tint) which extended inside the bulk of the materials. Some sharp edges previously present on the specimen were rounded off, indicating that a high degree of mobility had been reached.

The mosaic distribution was remeasured after annealing and the result is illustrated in Fig. III-3-3. The curve now has less structure than before treatment and the importance of the secondary peak relative to the main one is diminished The width at half height is slightly improved but the tail of the distribution are unaffected and extend as far as that of the untreated crystal.

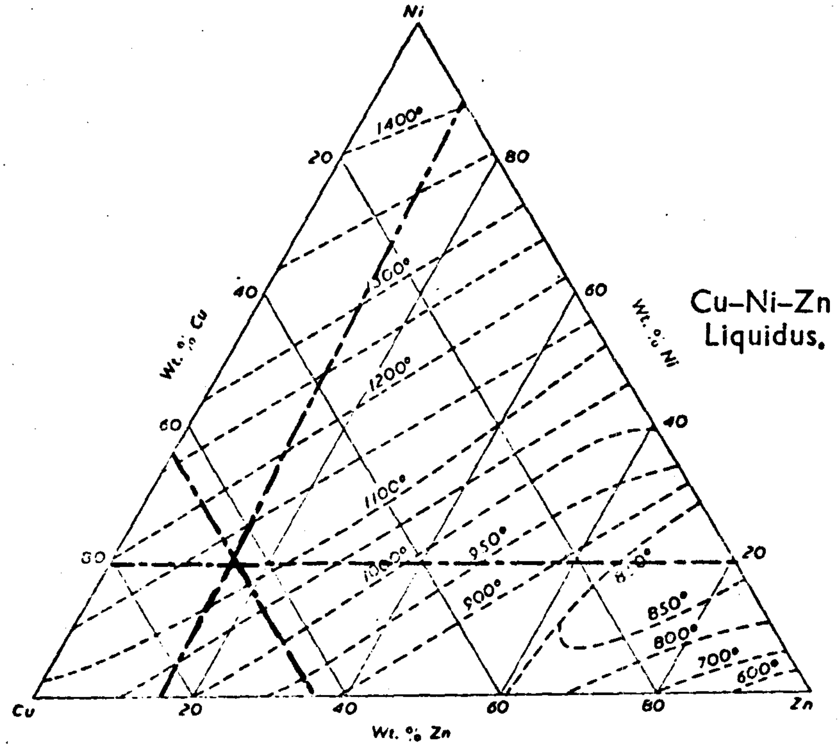

Fig. III-3-1; (taken from Smithells [62])

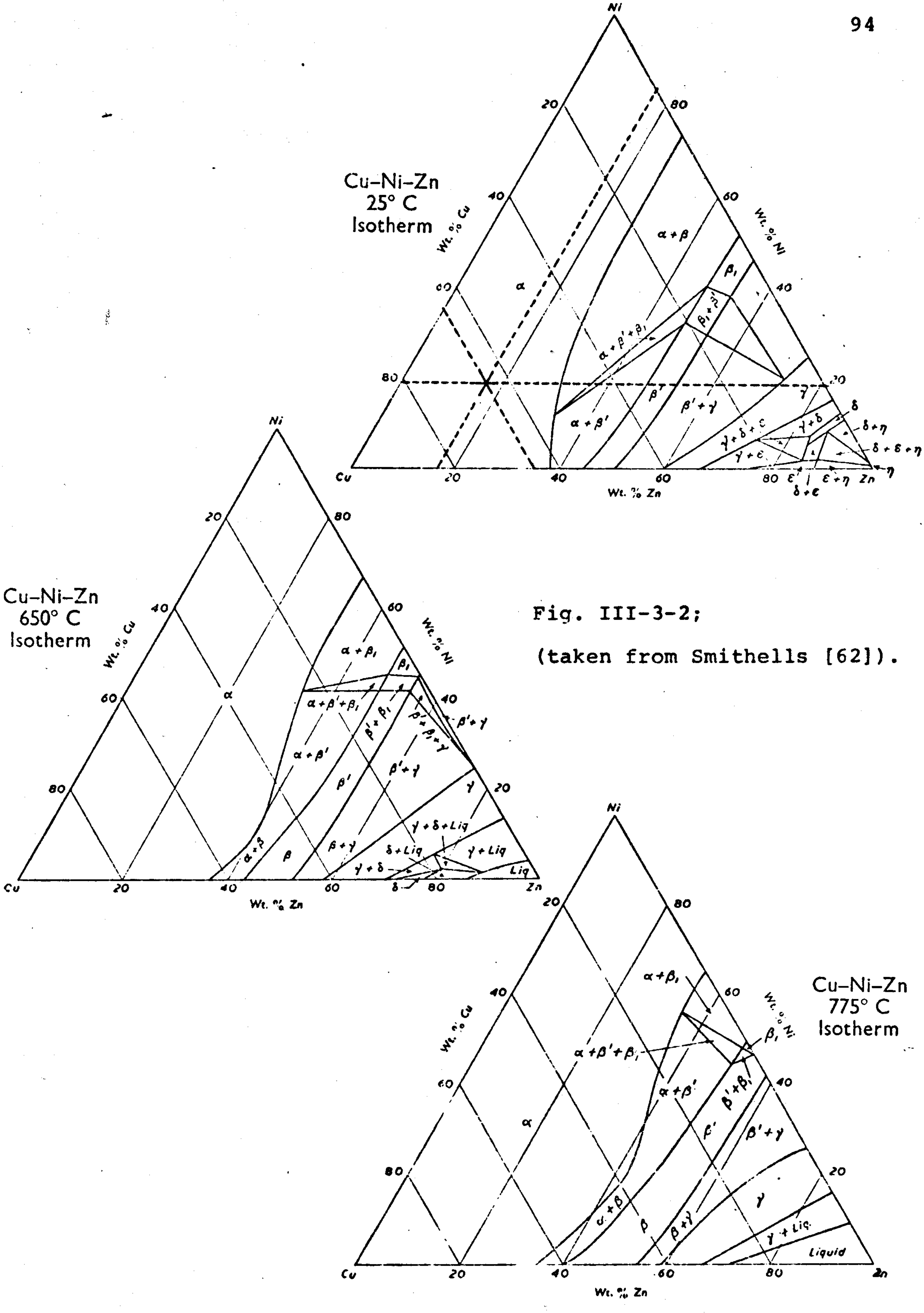

Fig. III-3-2;

(taken from Smithells [62]).

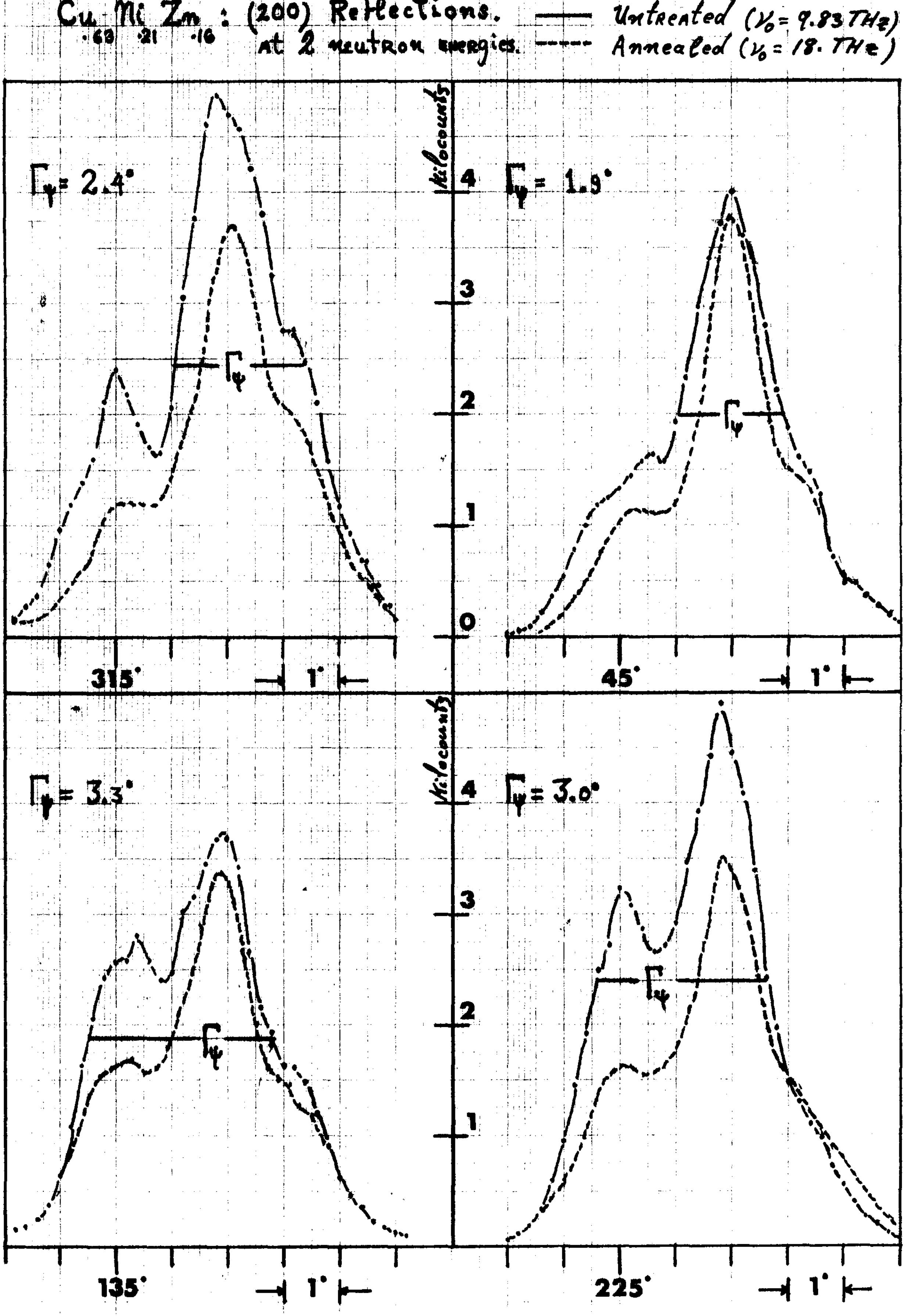

$Cu_{.63}Ni_{.21}Zn_{.16}$: (200) Reflections. at 2 neutron energies.

Fig. III-3-3

4-Measurement of the lattice parameter.

The lattice parameter was measured by neutron diffraction using the method described by Ng[67]. A good copper crystal was used as a standard, and its (220) reflection was compared with that of the specimen, using a neutron wavelength of 2Å.

The resulting family of ψ-rocking curves is shown in Fig. III-4-1; this is very different from the case of a good crystal and a scan of nearly 8° in ψ had to be done in order to detect the contribution from all the mosaic blocks. The envelop of the family of ψ-rocking curves was obtained by taking the peak intensity of each curve and plotting this as a function of the corresponding scattering angle (ϕ). It was verified that little change is obtained in the final determination of the lattice parameter if one takes the intensity at half width instead.

The resultant envelop of the family of curves in Fig. III-4-1 is given in Fig. III-4-2 for the ternary specimen and other crystals of variable content of Cu, Ni and Zn. The curve for the ternary peaks at a value of the lattice parameter:

$$a = 3.6229\text{Å} \; (Cu_{.63}Ni_{.21}Zn_{.16})$$

The same function for the copper crystal measured under the similar conditions may be taken to yield the value of the width contributed from instrumental resolution. From this the true full width at half maximum coming from the specimen's inhomogeneity is estimated to be 0.43° assuming Gaussian functions; this corresponds to a relative variation of the plane spacing throughout the crystal of

$$2\left|\frac{\delta a}{a}\right| = \frac{1}{2}\cot\left(\frac{\phi}{2}\right)\delta\phi = 0.3\%$$

i.e. $a+\delta a = 3.6229 \pm 0.006$ Å.

This is an indication that the plane spacing is fairly homogeneous through the specimen. It is however not sufficient information to conclude that the same is true of the chemical composition. Fig. III-4-3 shows the result of the measurement of the lattice parameter by the method of X-rays for different concentrations of the constituent elements. Since the curve for Cu-Zn (0%Ni) is fairly linear, the available points for a ternary concentration were joined with the points of equal Ni concentration on the Cu-Ni (0%Zn) curve. The procedure is justified by observing that the resulting interpolated constant Ni concentration curves are parallel to the Cu-Zn curve.

This figure illustrates the fact that the small relative plane spacing inhomogeneity does not necessarily imply a strong chemical homogeneity since there is a whole range of concentrations curresponding to a given lattice parameter. However, the good agreement between the value of the lattice parameter corresponding to the chemical composition at one extremity of the crystal (section III-2 and fig. III-4-3) and the measured lattice parameter, necessarily averaged over the whole of the crystal because of the neutron technique used, tend to indicate that the crystal is fairly homogeneous.

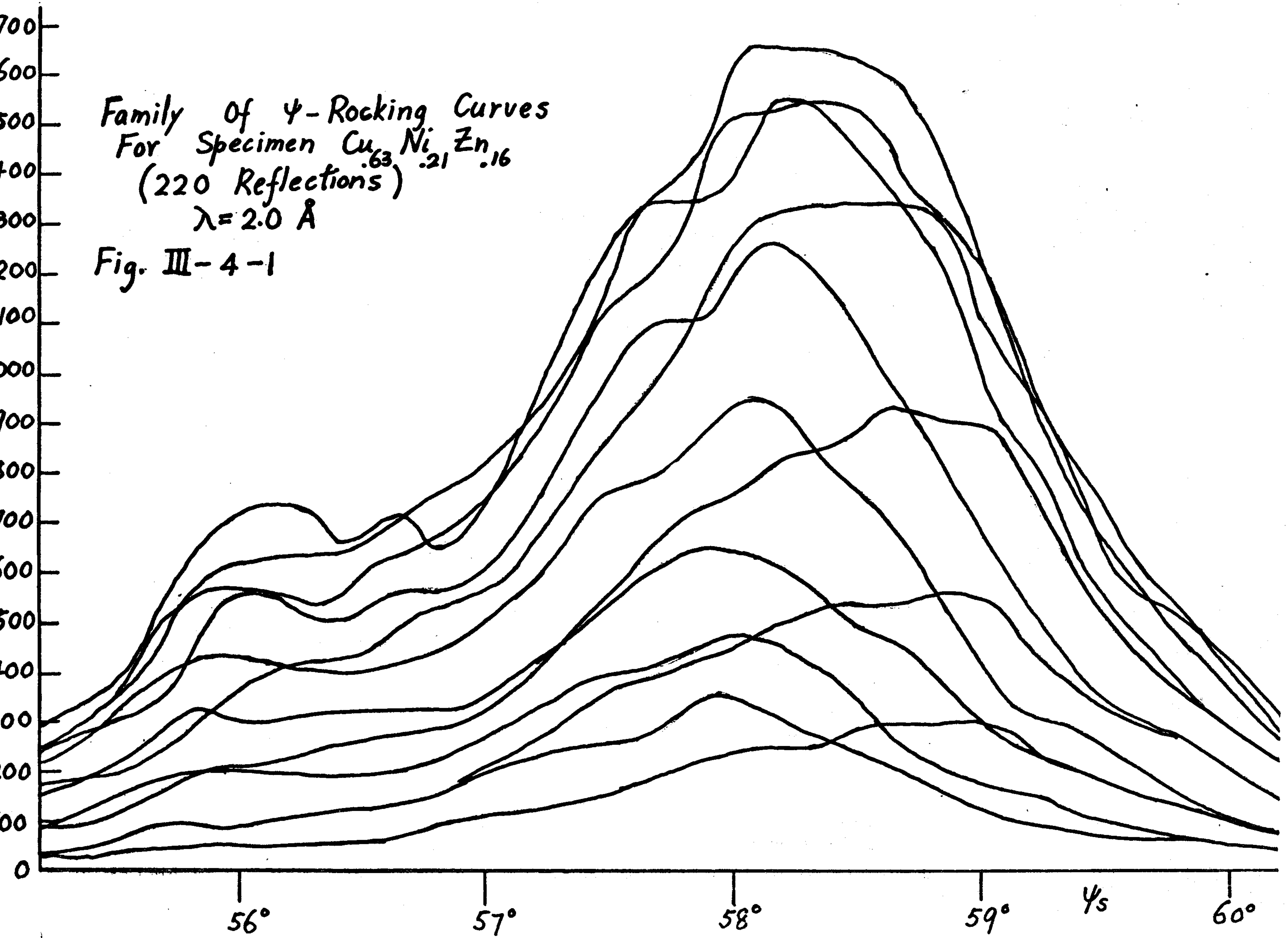
Family Of Ψ-Rocking Curves
For Specimen $Cu_{.63}Ni_{.21}Zn_{.16}$
(220 Reflections)
$\lambda = 2.0$ Å

Fig. III-4-1

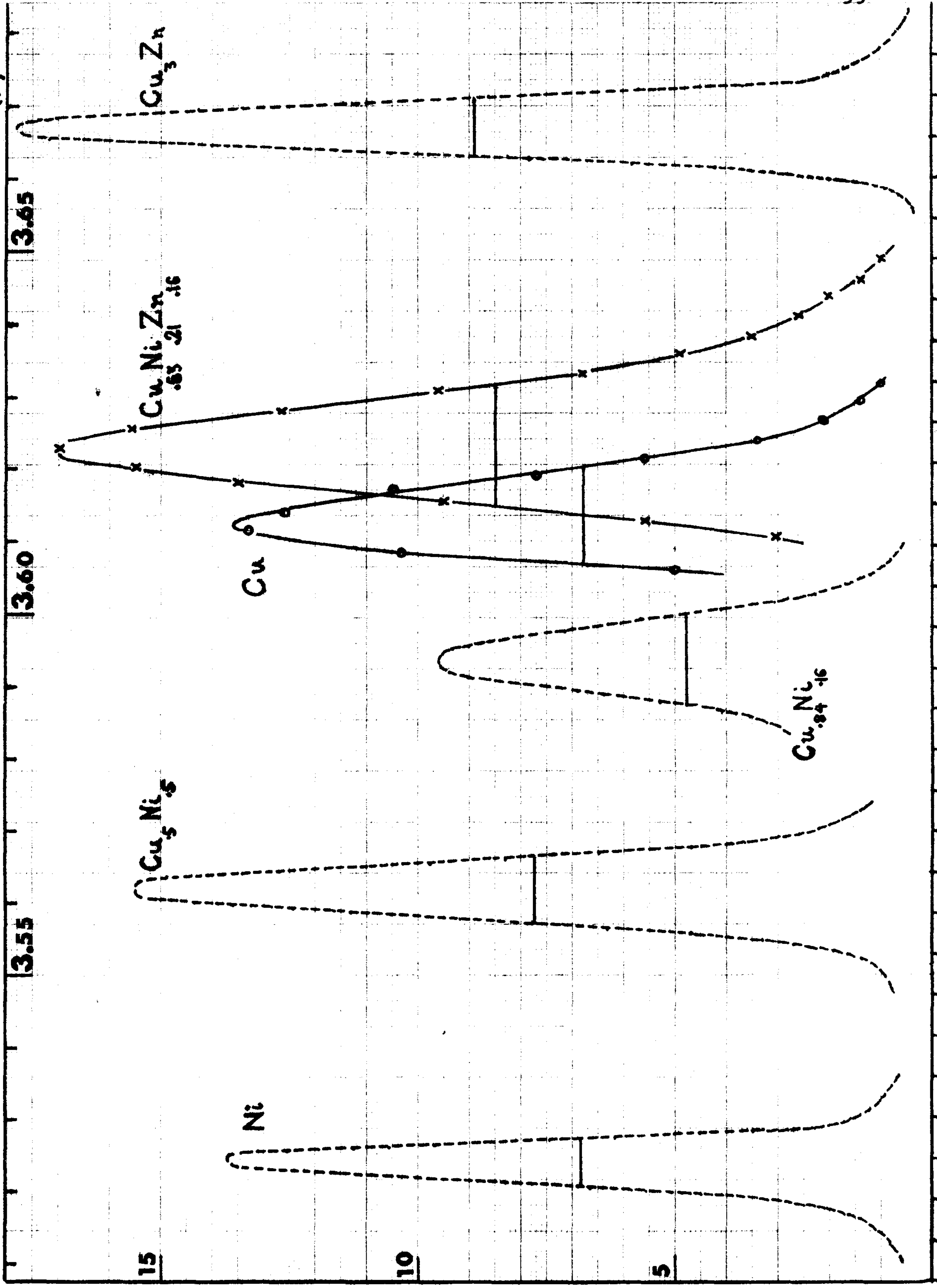

Fig. III-4-2; Variation of the lattice parameter with composition.

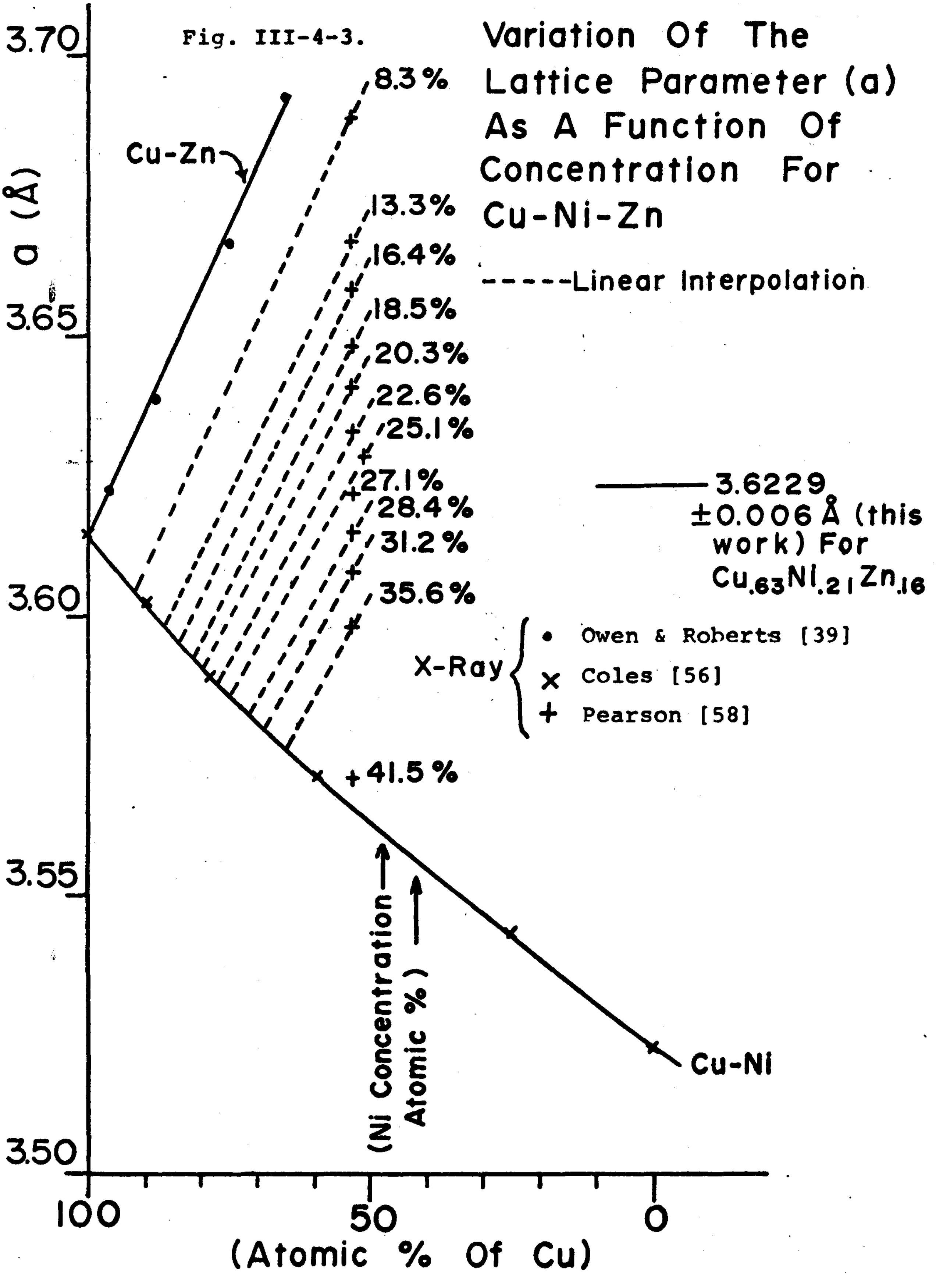

Fig. III-4-3. Variation Of The Lattice Parameter (a) As A Function Of Concentration For Cu-Ni-Zn

5-Phonon Measurement

i) Choice of experimental conditions

Measurements were carried out using a constant incident neutron energy and the choice of this experimental parameter is governed by two main considerations: optimization of the resolution and avoidance of the contaminant.

a) Resolution considerations

The energy and wavevector of neutrons undergoing elastic coherent scattering from a crystal obey the following relation:

$$E = \frac{\hbar^2 k^2}{2M} = \frac{\pi^2 \hbar^2}{2Md^2 \sin^2\theta_S} \qquad (1)$$

where $2\theta_S$ is the scattering angle and d is the scattering plane spacing.

Since the monochromatization of the incident neutron beam and the energy analysis of the scattered beam are carried out by Bragg-reflection, good energy resolution means that a small change in energy corresponds to a large change in angular position of the crystals, in order that the energy of the beams be little sensitive to the divergences resulting from imperfect collimation. Hence one must minimize the ratio

$$\left|\frac{dE}{d\theta}\right| = \frac{\pi^2 \hbar^2}{d^2 M} \frac{\cot\theta}{\sin^2\theta} \qquad (2)$$

and this may be satisfied so much the better that the angle θ is close to $\frac{\pi}{2}$. The ideal situation is one in which this condition is approximated in both the monochromator and the analyzer and their respective plane spacings govern how well this is satisfied in the measurement of a particular phonon.

Fig. III-5-i-1 illustrates the rapidly varying function $\cot\theta/\sin^2\theta$ of equation (2).

Under conditions of phonon energies and temperature such that the phonon reduced energy ($\hbar\omega/kT$) is smaller than one, it is a matter of indifference whether one proceeds under conditions of neutron energy loss or energy gain because the population factor in this domain is a number much larger than unity. (Fig. II-4-i-1). The requirements of a large scattering angle in both monochromator and analyzer means that the plane spacing of the analyser should be larger tha that of the monochromator in the first case (neutron energy loss) and smaller in the other (neutron energy gain). For example, the experiment reported here was done under the condition of phonon creation and the monochromator and analyzer were respectively Cu(220) and Cu(200); Fig. III-5-i-2 illustrates the behaviour of equation (1) as a function of the scattering angle in these two cases.

For lack of the possibility of having an infinitly adjustable plane spacing over a convenient range in order to work at the largest scattering angles in the monochromator and the analyzer, we expect from the analytic expression of equation (1) that, for a given experimental arrangement, the spectrometer energy resolution would be optimized by matching the energy spread in the monochromator (δE_M) and in the analyzer (δE_a).

These energy spread are related to the collimation angles via the relations

$$\delta E_m = \frac{dE_m}{d\theta_m}\alpha_m \quad (3a); \qquad \delta E_a = \frac{dE_a}{d\theta_a}\alpha_a \quad (3b)$$

using the usual notation. The requirement $\delta E_m = \delta E_a$ means that

$$\frac{\alpha_m}{d_m^2} \frac{\cot\theta_m}{\sin^2\theta_m} = \frac{\alpha_a}{d_a^2} \frac{\cot\theta^*_a}{\sin^2\theta^*_a} \tag{4}$$

Assuming that the incident energy (or θ_m), the collimation angles and the plane spacing are known it is possible to obtain $\sin^2\theta^*_a$ satisfying equation (4) either by solving a cubic equation or, more conveniently, by a graphic method which is now briefly described.

A certain value of the incident energy determines the monochromator half scattering angle θ_m (Fig. III-5-i-2) and the corresponding ratio $\cot(\theta_m)/\sin^2(\theta_m)$ (Fig. III-5-i-1). Using equation (4) with $d_a > d_m$ for neutron energy loss and the converse for neutron energy gain

$$\frac{\cot\theta^*_a}{\sin^2\theta^*_a} = \frac{\alpha_m}{\alpha_a} \left(\frac{d_a}{d_m}\right)^2 \frac{\cot\theta_m}{\sin^2\theta_m} \tag{5}$$

is determined from the proper values of the collimation angles α and the plane spacing d. Finally one obtains the analyzer angle θ_a for optimum energy resolution and the energy of the phonon corresponding to this setting by using the relation for the energy transfer under conditions of optimum energy resolution which may be written as

$$\nu^*_p = \pm\left(\frac{E_m - E_a}{h}\right) = \frac{\pm h}{8M} \left(\frac{1}{d_m^2 \sin^2\theta_m} - \frac{1}{d^2 \sin^2\theta^*_a}\right) \tag{6a}$$

$$= \pm\nu_m \left(1 - \frac{d_m^2 \sin^2\theta_m}{d_a^2 \sin^2\theta^*_a}\right) \tag{6b}$$

where the symbols of Table I-1 were used and the relation between θ_m and θ_a^* is given by equation (5). The positive sign and the condition $d_a > d_m$ are to be taken for neutron energy loss and the converse for neutron energy gain.

The value of ν_p^* depends on the incident frequency ν_m and on the experimentally adjustable prarmeters d and α which determine θ_a^* through equation (5)

Let us consider the case of neutron energy loss. The minimum value of the function ν_p^* is zero (for all value of the incident frequency ν_m) when $d_m = d_a$ and $\theta_m = \theta_a^*$ (i.e. $\alpha_m = \alpha_a$ from equation (5)). It increases progresively as the ratio

$$\frac{d_m^2}{d_a^2} \, \frac{\sin^2\theta_m}{\sin^2\theta^*{}_a}$$

is made smaller by decreasing the ratio α_m/α_a (equation 5) for a given value of the ratio d_m^2/d_a^2.

Fig. III-5-i-3 illustrates the behaviour of the function ν_p^* for commonly used ratios d_m^2/d_a and α_m/α_a.

Two remarkable cases are those where $d_a = d_m$ and $\alpha_a = \alpha_m$ which gives $\nu_p^* = 0$ for all values of the incident energy ν_m. This is the case relevant to elastic scattering. Another interesting situation occurs when

$$d_a^2 = 2d_m^2 \text{ and } \alpha_a = 2\alpha_m$$

in which case, equation (6b) simplifies to

$$\nu_p^* = \frac{1}{2}\,\nu_m$$

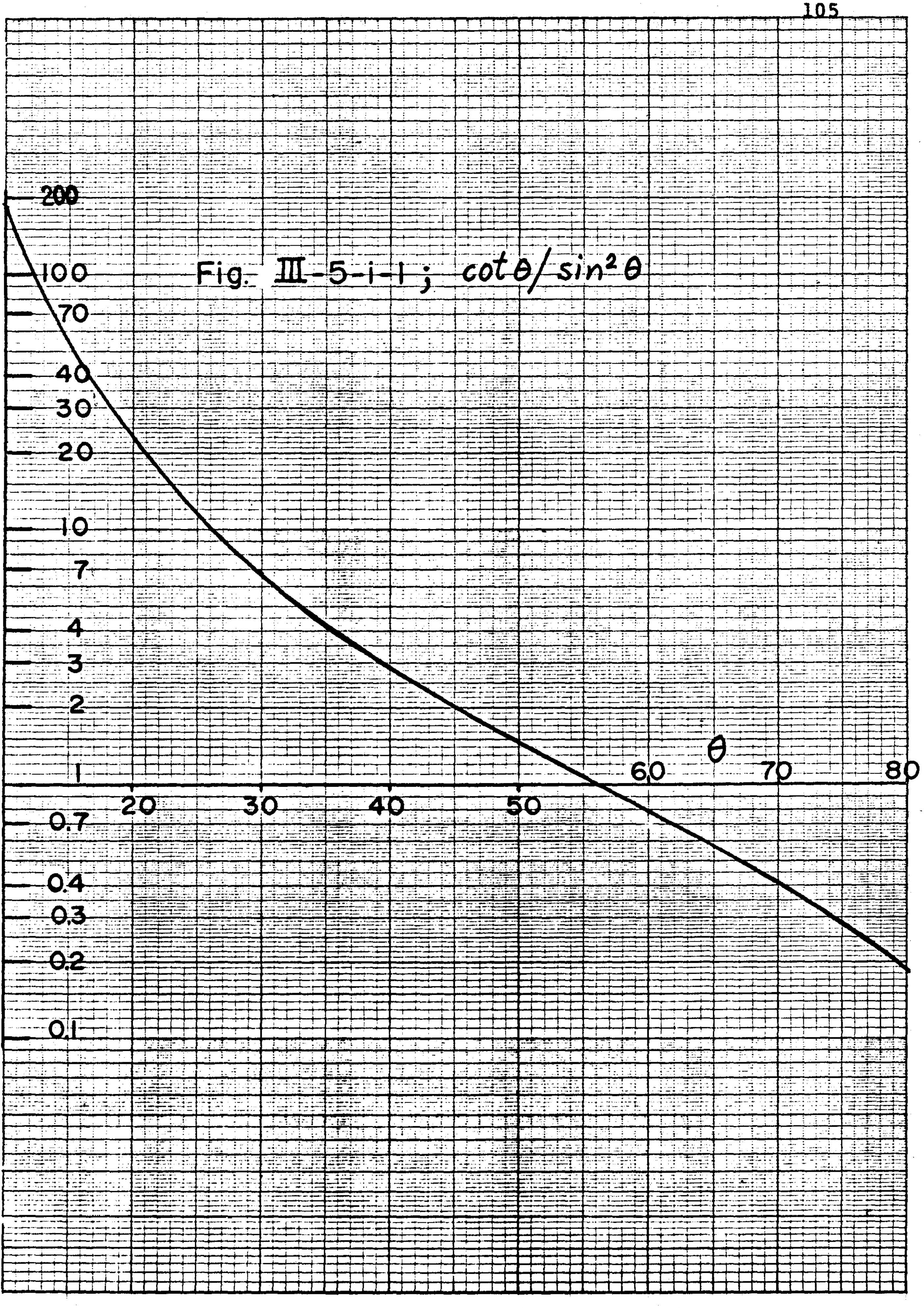

Fig. III-5-i-1; $\cot\theta/\sin^2\theta$

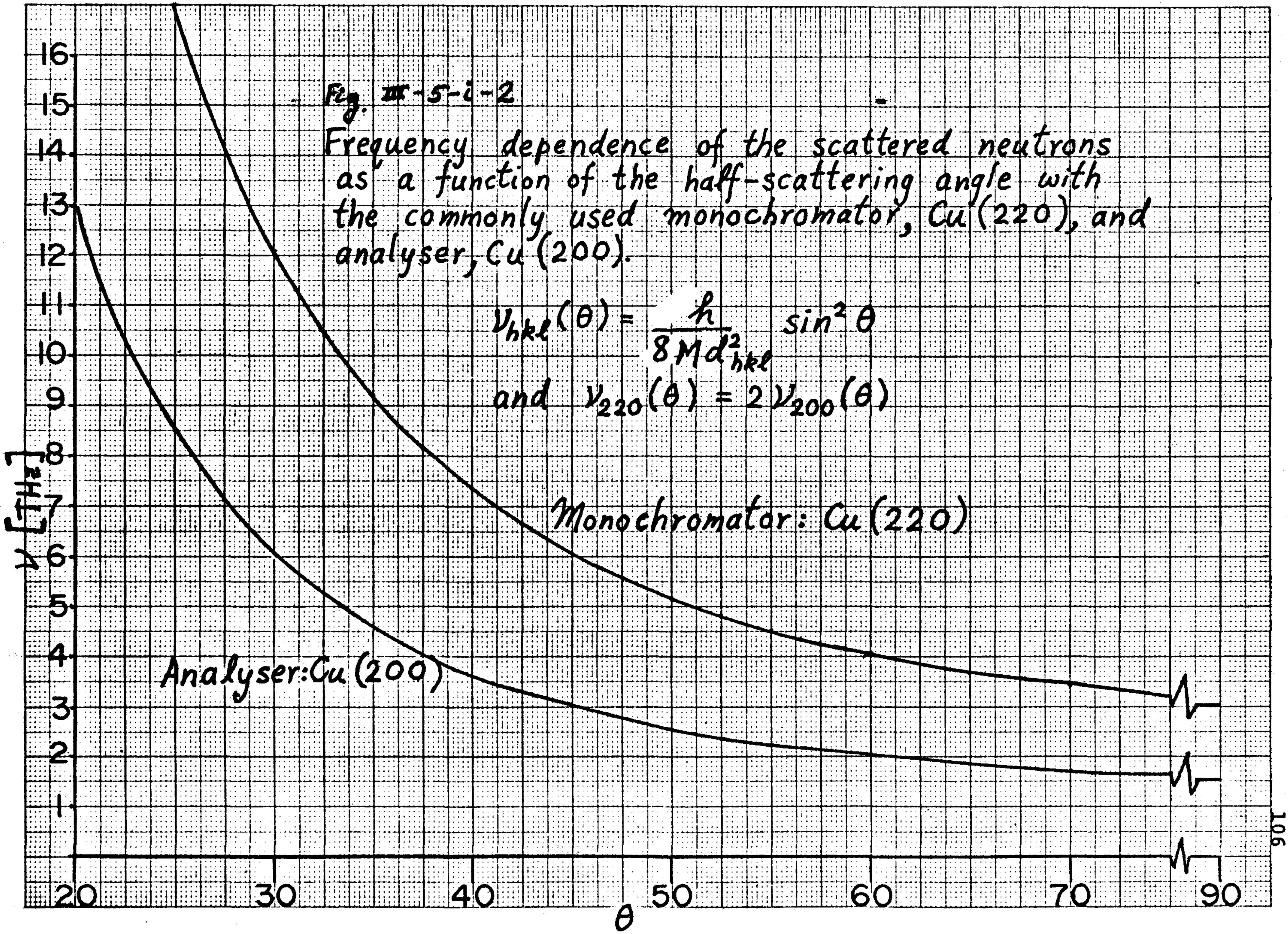

Fig. III-5-i-2

Frequency dependence of the scattered neutrons as a function of the half-scattering angle with the commonly used monochromator, Cu (220), and analyser, Cu (200).

$$\nu_{hkl}(\theta) = \frac{h}{8Md^2_{hkl}} \sin^2\theta$$

$$\text{and} \quad \nu_{220}(\theta) = 2\nu_{200}(\theta)$$

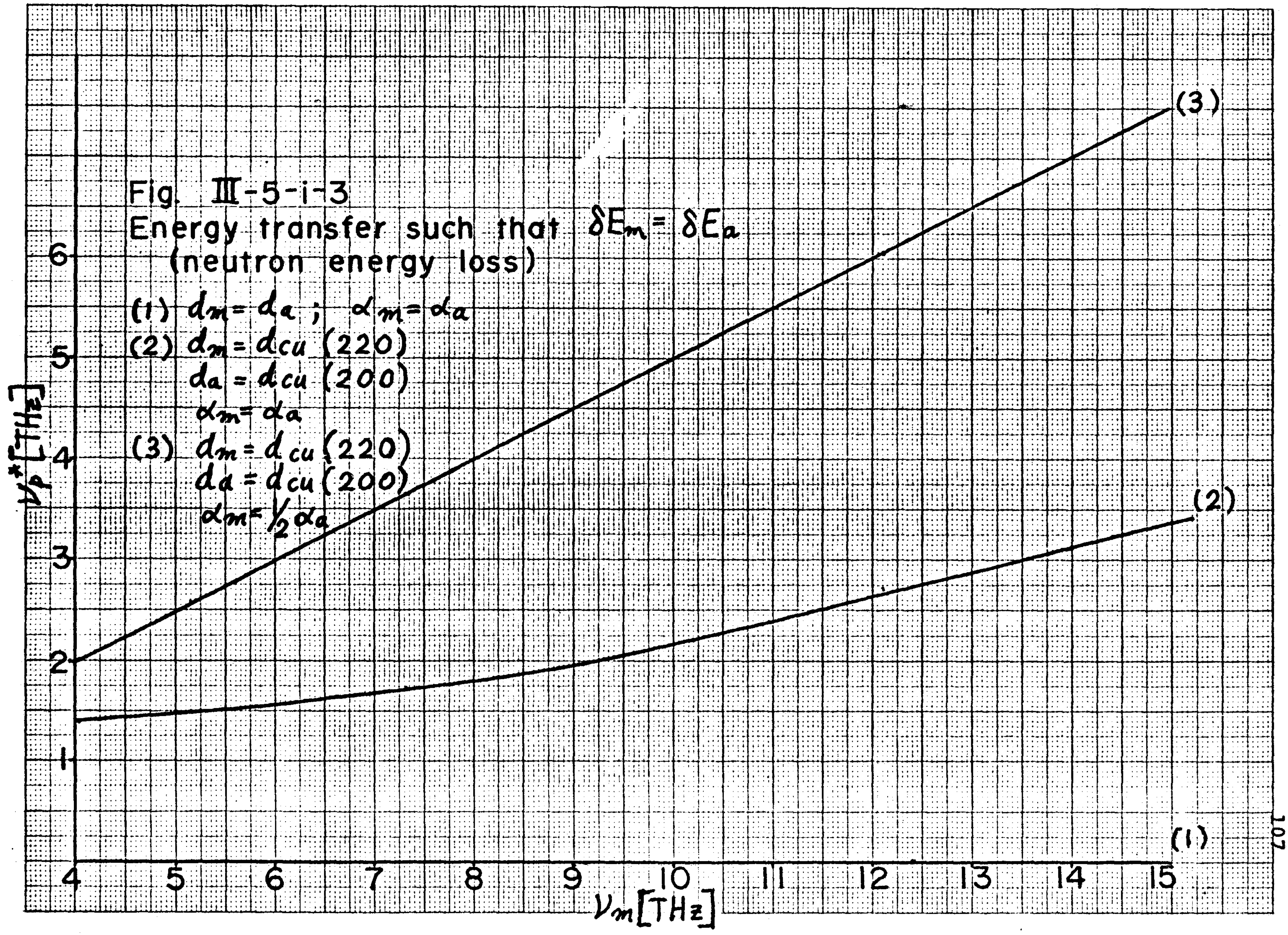

Fig. III-5-i-3
Energy transfer such that $\delta E_m = \delta E_a$
(neutron energy loss)

b) Considerations of the contaminant

The incident beam does not only contain first and higher orders of the main (220) component but also a series of contaminant energies of which the main one is (331). (Hallman [69]) The composition of the beam as measured by Hallman is illustrated in Fig. III-5-i-4.

Obviously the presence of the contaminated may hinder the interpretation of experimental results if proper care is not taken. To prevent any ambiguity, it is necessary to avoid the case where the contaminant is going through an elastic incoherent scattering process from the specimen and through a second order scattering process in the analyzer, that is

$$\nu_c \neq 4\nu_a = 4(\nu_m - \nu)$$

$$\text{i.e. } \nu \neq \nu_m - \nu_c/4$$

Using the data of Fig. III-5-i-4, the function $\nu_m - \nu_c/4$ was plotted in Fig. III-5-i-5. It gives the apparent position of the contaminant during a phonon scan. Using this graph, it is thus possible to select phonons which lie in an energy range where the contaminant will not be detected during the whole of the scan.

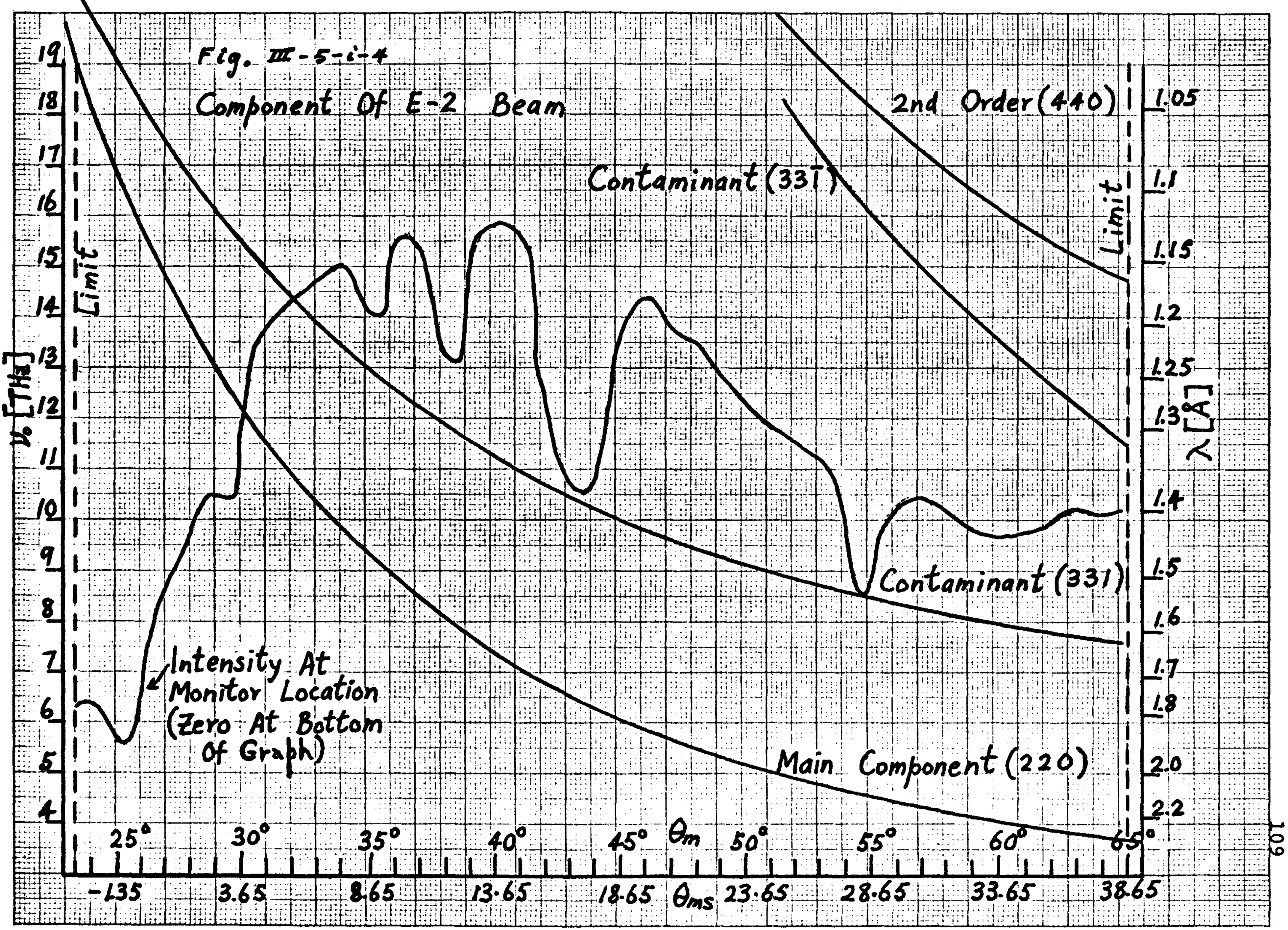

Fig. III-5-i-4

Component Of E-2 Beam

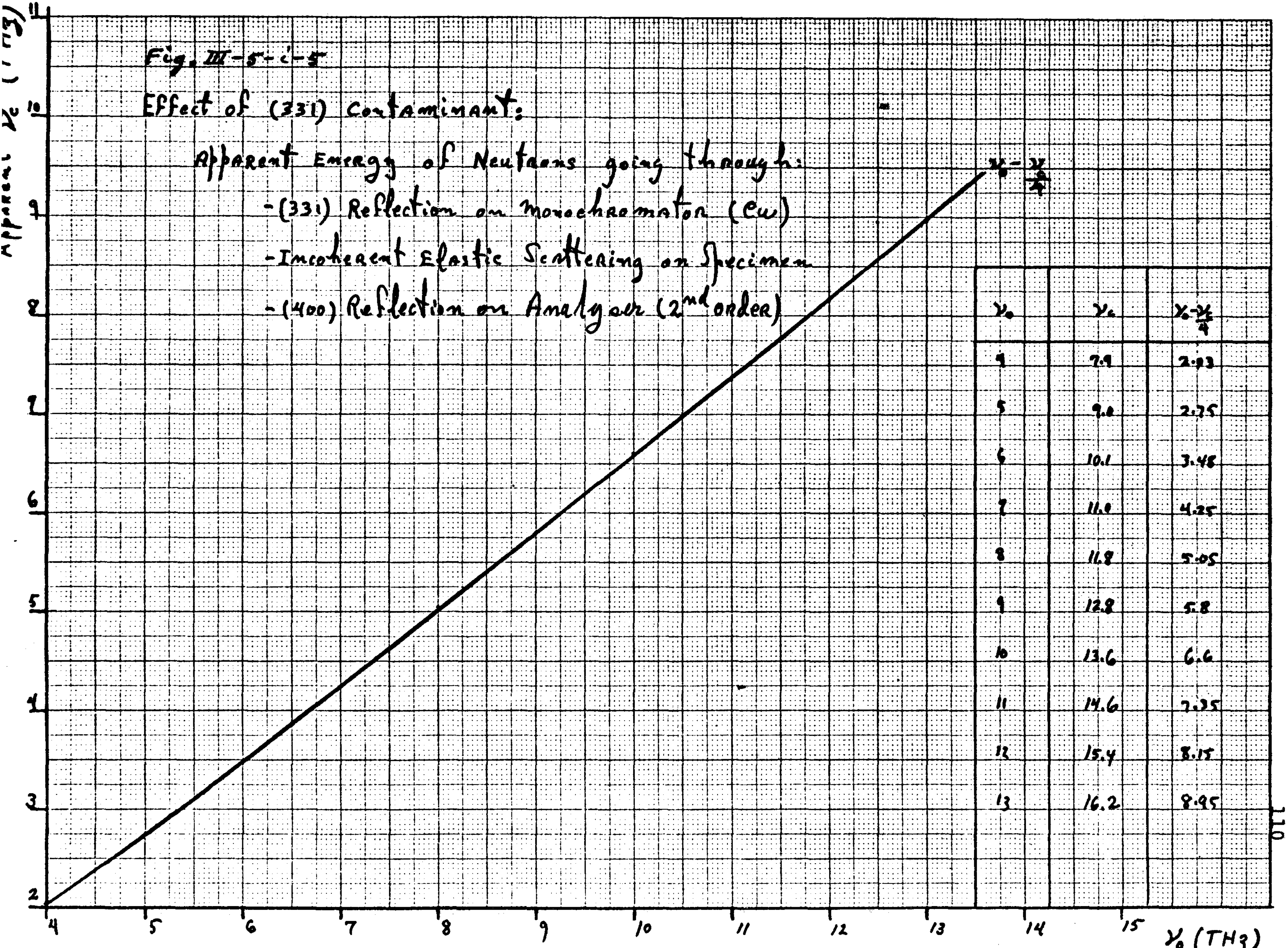

Fig. III-5-i-5

Effect of (331) contaminant:

Apparent Energy of Neutrons going through:

- (331) Reflection on monochromator (Cu)
- Incoherent Elastic Scattering on Specimen
- (400) Reflection on Analyzer (2nd order)

ν_0	ν_c	$\nu_0 - \frac{\nu_c}{4}$
4	7.9	2.03
5	9.0	2.75
6	10.1	3.48
7	11.0	4.25
8	11.8	5.05
9	12.8	5.8
10	13.6	6.6
11	14.6	7.35
12	15.4	8.15
13	16.2	8.95

ii) Resolution function: calculated and measured.

We have made in sub-section II-4-iii some theoretical considerations on the relation between the calculated and measured isoprobability contours and it was pointed out that a comparison between these two objects illustrates the worsening of the resolution from the specimens mosaic spread. Physically, this is because of the resulting tangential smearing of the reciprocal lattice points.

The resolution function of the spectrometer was measured with the specimen in position and the result is illustrated in figure III-5-ii-1 for the region in reciprocal space around the point $\underset{\sim}{Q}=(0,2,0)$. The function for the transverse polarization is very different from what is commonly encountered and it resembles strongly to a juxtaposition of two ellipses which may each be tought as being contributed from either peaks of the mosaic distribution (sub-section III-3). Besides this structure in the function, the presence of mosaic spread also results in a widening of the contour comparatively to that corresponding to a good crystal; this later case is approximated by the calculated curve which is also included in the figure. The difference between these two is very pronounced but a certain amount of confidence for the result of the calculations may be obtained by comparing the prediction with the actual measurements from a good crystal as was done for example by Mr. A. P. Roy [70] who found consistent agreement.

The effect of mosaic distribution on the isoprobability contour (transverse polarization) may be estimated in a simple way by calculating the resulting value of the perpendicular component to the momentum transfer $\underset{\sim}{Q}$. Taking $\Gamma_\psi = 2°$ (i.e. 0.035 radiant) as a representative value of the full width at half maximum of the central peak of the mosaic distribution, one gets:

$$\frac{a\delta Q_\perp}{2\pi} = \frac{aQ}{2\pi}\Gamma_\psi = 0.07$$

This is in excellent agreement with the width in ζ of the main ellipse if one adds the intrinsic width in ζ of the ellipse, i.e. 0.01.

The case of the longitudinal polarization does not have such a straightforward explanation. The reason for the widening in energy relative to the calculated curve may be best understood by observing that the intercepts on the energy axis must be the same for both polarizations when $\zeta=0$, whether the mosaic spread is present or not, since they correspond to the same two points on the resolution ellipsoid in $(\underset{\sim}{Q}-\omega)$ space, but projected on two orthogonal planes, i.e. $(Q_x-\nu)$ and $(Q_y-\nu)$ planes.

Fig. III-5-ii-1 $\mathrm{Cu}_{63}\mathrm{Ni}_{21}\mathrm{Zn}_{16}$: Resolution function in (001) plane around the point $\frac{a\underset{\sim}{Q}}{2\pi} = (0,2,0)$

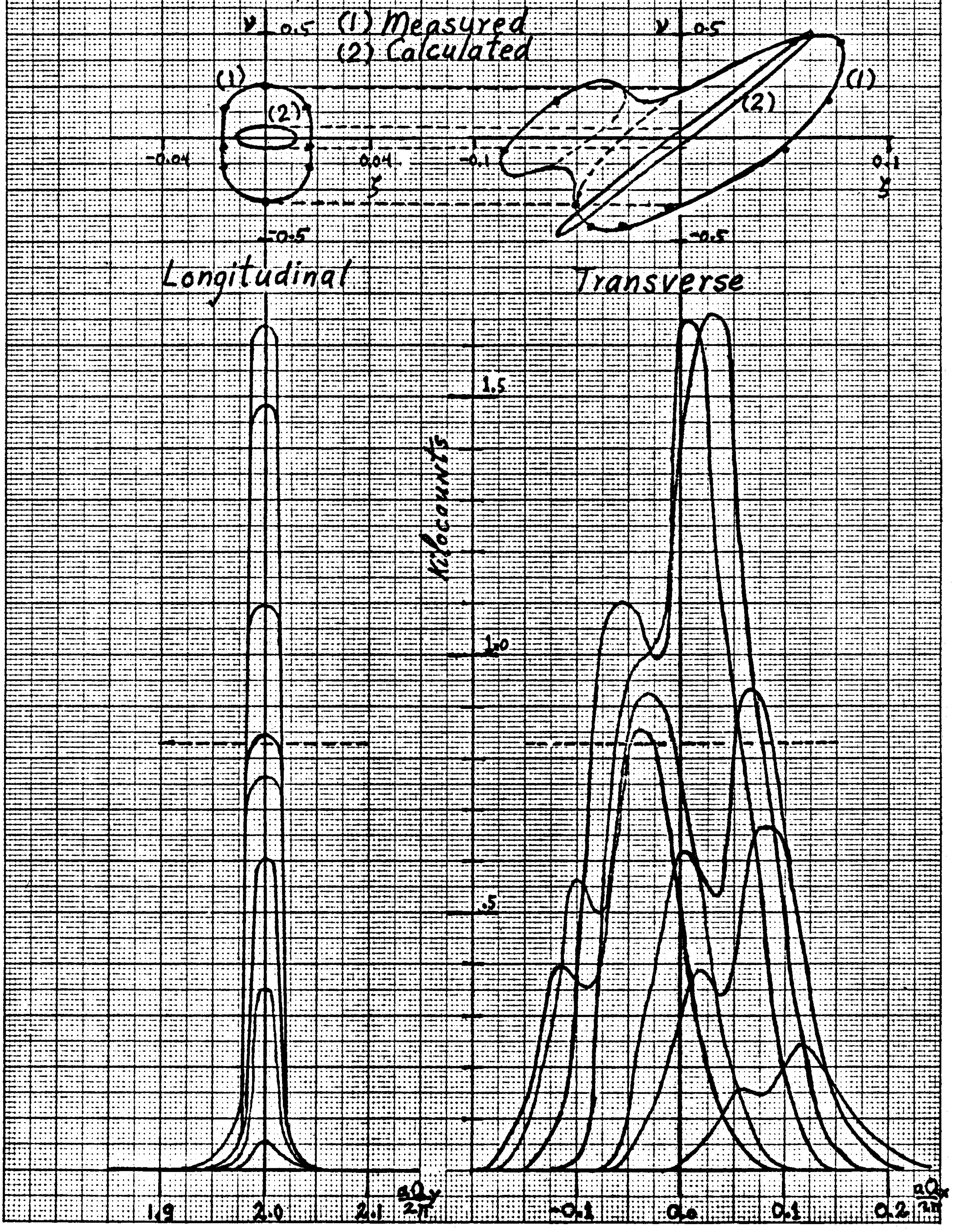

iii) Phonons and their measurement.

This final sub-section dealing with the results of the measurements of the phonon spectrum of the alloy may be divided into three parts: a) Experimental considerations

b) Line shapes

c) Discussion.

the results are summarized in table III-5-iii-1.

a) Experimental considerations.

The specimen had the geometry of a cylinder 10 cm. long and 6 mm. in diameter with a (001) crystallographic very nearly parallel to its axis; it was mounted on a support which allowed the changing of its orientation as a relativly simple procedure. The measurements of the phonons were made at room temperature, in which conditions the crystal has a face centred cubic structure (fig. III-3-1) and correspondingly, its reciprocal lattice has a body centred cubic structure. Two different crystal alignments suffice to observe phonons propagating in the principal symmetry directions of the Brillouin zone and these are obtained respectivly by making the (001) and (0$\bar{1}$1) planes parallel to the scattering plane of the spectrometer; figure III-5-iii-1 represents these two planes with a typical wave vector arrangement.

The experimental procedure consisted in keeping the neutron incident energy and the momentum transfer fixed while varying the energy transfer (Brockhouse [61]). Considerations

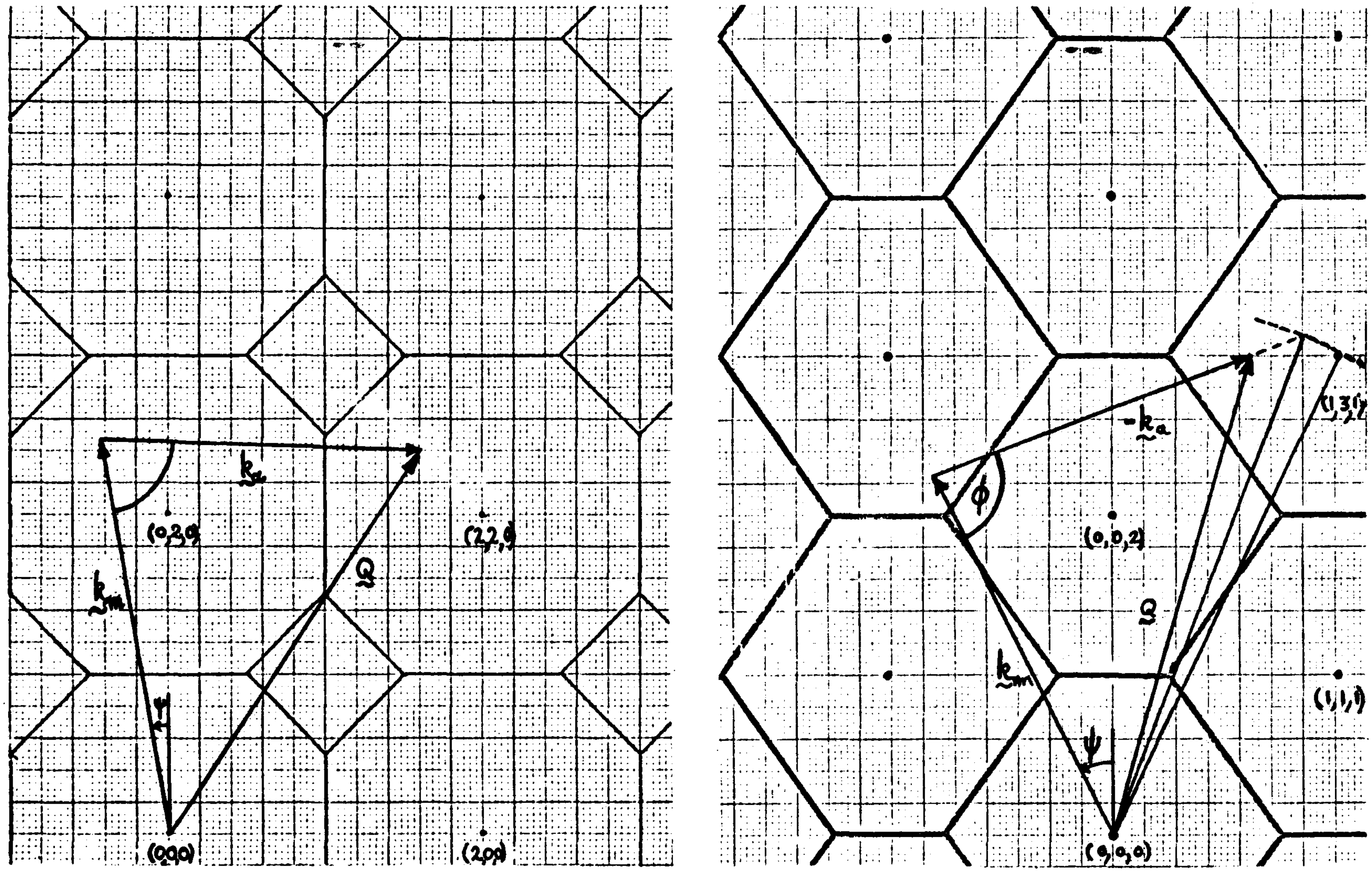

Fig. III-5-iii-1 a) (001) plane b) (0$\bar{1}$1) plane

The two major symmetry planes of the B.C.C. lattice.

of the factor $(\underset{\sim}{Q}\cdot\underset{\sim}{\xi})$ in equation II-4-(4) governs the choice of the region in reciprocal space where a given phonon may be observed; ideally, the momentum transfer should be parallel to the phonon eigen-vector for a twofold reason: to maximize the factor $(\underset{\sim}{Q}\cdot\underset{\sim}{\xi})^2$ in the expression for the cross-section and to minimize the possibility of interference with phonons of other polarizations whose eigen-vectors might show a large component along $\underset{\sim}{Q}$ and whose energies lie in the range of the scan. The first requirement may also be satisfied by taking a large value of the vector $\underset{\sim}{Q}$ but this has other consequences which may not be desirable since a large value of $\underset{\sim}{Q}$ increases the relative importance of multi-phonons processes (Sjolander [58]) and this becomes objectionable in the case where the Debye-Waller factor is large, which is not the case here. Also, a small value of $\underset{\sim}{Q}$ is desirable in the case of an imperfect crystal since the previously discussed smearing of the reciprocal lattice points is more pronounced for large values of this wave vector.

This last consideration was important with the ternary but measurements made at large values of the momentum transfer proved to be more practical because the gain in intensity is proportional to the square of the vector $\underset{\sim}{Q}$ while the price paid in terms of the widening of the lineshape is only proportional at most to the first power in $\underset{\sim}{Q}$.

b) Line shapes: calculated and measured.

The neutron groups, althought much widened by the imperfect mosaic distribution, were surprisingly well defined in most cases. The theory of chapter II was put to the test in this particular case and figures III-5-iii-4 and 5 show a sampling of the results obtained for different phonons. The theoretical width was calculated by assuming a gaussian mosaic distribution whose width was given by that of the intensity distribution of a nearby Bragg reflection without taking into account the double peak nature of the distribution which was less proeminent in the (0$\bar{1}$1) plane where most of the measurements were carried than in the (001) plane corresponding to the situation depicted in figure III-3-3. For comparison purposes, the instrumental width can be obtained either by calculation or by repeating the experiment using a good specimen of a crystal having a prononced similarity with the bad one In our case, copper met these requirements (table III-1-(1)-a and fig. III-4-2). The phonons shown in the above mentioned figures were measured under identical experimental conditions as those found on the adjoining transparencies which were taken from the work of Dr. A.P. Miiller on a copper specimen having a mosaic width of 0.5° and it was also verified that these groups are in good agreement with the ones calculated using the proper value of the mosaic spread.

Comparison of the neutron groups from the two materials confirms that the widths of longitudinal phonons are much less affected than the transverse ones. However, figure III-5-iii-5 shows a case of some zone boundary phonons where both the transverse and longitudinal branches are similarly widened relativly to copper and to the calculated curve. Since the energy q-gradient is zero, one does not expect any effects from the presence of mosaic spread and the observed groups should be similar to those of copper, as predicted by the calculations. Since it is not so, the extra width could be a manifestation of atomic force constants disorder on short wavelenght phonons which are a sensitive probe to local variations as compared with those of long wavelenght which see more of the continuum aspect of the crystal.

Besides increasing the error in the energy determination of the phonons by increasing the line width, the mosaic spread also caused two other difficulties. The first of these was encountered in the measurement of the T_2 branch and this is illustrated in figure III-5-iii-1-b). In this geometry, a fraction of the crystallites turns out to be properly oriented for elastic coherent scattering into the analyser. The large number of counts accumulated in both the signal and background counters indicates that the neutrons reach the detectors through an elastic incoherent scattering process off the analyser crystal thus burying the weak phonon signal. This difficulty was circumvened by measuring this branch with a low incident energy thereby maximizing the resolution in energy (sub-section III-5-ii) and in momentum transfer by making the scattering angle larger.

The second difficulty relates to the measurement of the small wave vector region of the dispersion curves where the signal of transverse phonons would be lost in the Bragg-scattered neutrons at a larger phonon wave vector than would have been otherwise the case if a good crystal had been used.

We have seen in section II-7 how the apparent peak position of the neutron groups of transverse polarization differs from the true peak position in the case where the mosaic spread is important. The correction, of the form:

$$\Delta = 0.362\Gamma^2/\nu$$

was made here on the apparent energy of phonons in the $[00\zeta]T$, $[0\zeta\zeta]T_1$ and $[0\zeta\zeta]T_2$ which showed considerable widening compared with those found in copper; hence the correction is justified. The $[\zeta\zeta\zeta]T$ phonons were not similarly corrected since they were not as much affected by the mosaic spread because of the particular topology of their dispersion surface (section II-5).

The term Γ in the above expression should appropriatly be the true width, i.e. the width after correction for instrumental resolution. Assuming a gaussian line shape and resolution, this correction rapidly becomes less important when the wideoning is significant and one may take Γ as the width of the observed group; this will obviously overcorrect but the error is typically a small fraction of the uncertainty in the peak position.

Table III-5-iii-1 and figure III-5-iii-2 illustrate this correction on two particular branches which were each measured in the same region of reciprocal space and with the same incident neutron energy all along the branch. The continuous lines in the figure is simply an eye-ball fit to the calculated points and does not represent any fitting procedure. Note that in this case the term Γ was corrected for instrumental width from the available results on copper which had been measured under identical conditions; also that the correction at the zone boundary has to be identically zero because of the zero q-gradient of the energy of the phonon.

c) Discussion.

As expected, the frequency spectrum is practically identical with that of pure copper. Table III-5-iii-2 shows our results compared with those of Svensson [67] whose work on copper was used as a standard in the search for possible energy shifts. There is a general trend for the spectrum to be moved toward higher frequencies, as expected from the value of the electronic concentration. However, the fact that the two measurements give energies which are within the estimated errors does not allow any definite conclusions altought the fact that the shifts are generally in the same direction tends to indicate that the effect is real. The reliability of the measurements was obviously affected by the presence of poor mosaic spread and, using the usual physically plausible rule of thumb which assigns to a phonon an uncertainty of one tenth of its observed width, the values of the uncertainties listed in the above mentioned table were determined; these values were made larger in the case where the neutron group was not perfectly defined. Most of the phonons were measured twice with different incident neutron energies and in a different scattering plane; good agreement was obtained and table III-5-iii-1 contains the most reliable results of these multiple measurements.

Table III-5-iii-1;

Correction to the peak position of phonons of transverse polarization from the term (n(x)+1)/x.

Branch	ζ	ν (THz)	Γ (THz)	Δ (THz)	$\nu+\Delta$ (THz)
$[00\zeta]$T	0.4	3.05	0.82	0.0741	3.12
	0.6	4.08	0.92	0.0725	4.15
	0.8	4.76	0.80	0.04	4.80
	1.0	5.12	0.74	0.00	5.12
$[0\zeta\zeta]T_1$	0.2	1.27	0.87	0.1828	1.45
	0.4	2.62	0.93	0.11	2.73
	0.6	3.87	0.90	0.0674	3.94
	0.75	4.60	0.80	0.04	4.64
	0.80	4.84	1.04	0.0733	4.91
	1.00	5.05	0.76	0.00	5.05
$[0\zeta\zeta]T_2$	0.6	5.72	0.95	0.043	5.76
	0.8	6.75	1.22	0.0566	6.81
	1.00	7.28	0.85	0.00	7.28

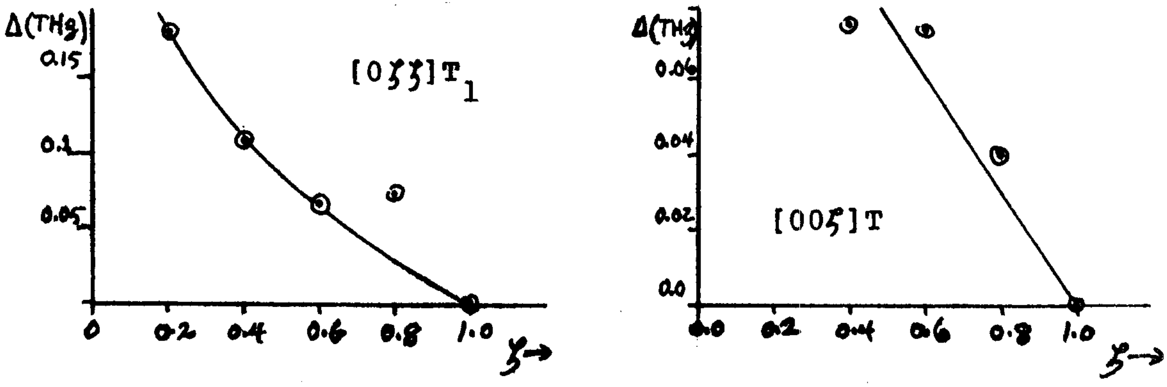

Fig. III-5-iii-2; Graph of above correction.

Table III-5-iii-2;

Comparative table of phonon frequencies

in Cu and $Cu_{.63}Ni_{.21}Zn_{.16}$.

		Cu	$Cu_{.63}Ni_{.21}Zn_{.16}$	
Branch	ζ	ν(THz)	ν(THz)	Γ(THz)
$[00\zeta]T$	0.2	1.56±0.04	1.64±0.07	0.70
	0.4	3.01±0.04	3.12±0.09	0.82
	0.6	4.15±0.05	4.15±0.10	0.95
	0.8	4.86±0.07	4.80±0.08	0.80
	1.0	5.08±0.08	5.12±0.08	0.74
$[00\zeta]L$	0.2	2.42±0.07	2.56±0.07	0.70
	0.4	4.47±0.07	4.58±0.06	0.60
	0.6	6.05±0.08	6.05±0.04	0.30
	0.7	6.60±0.08	6.76±0.09	0.90
	0.8	6.99±0.13	7.12±0.07	0.62
	0.9	7.17±0.12	7.12±0.09	0.88
	1.0	7.19±0.12	7.28±0.09	0.85
$[0\zeta1]\pi$	0.2	7.07±0.14	6.95±0.11	1.02
	0.4	6.44±0.09	6.49±0.11	1.08
	0.6	5.77±0.08	5.82±0.09	0.85
	0.8	5.27±0.08	5.13±0.12	1.20
$[0\zeta1]\Lambda$	0.2	4.99±0.07	5.14±0.09	0.85
	0.4	4.89±0.09	4.90±0.09	0.86
	0.5	4.89±0.08	5.04±0.09	0.87
$[0\zeta\zeta]T_1$	0.2	1.35±0.04	1.45±0.09	0.87
	0.4	2.70±0.04	2.73±0.10	0.93
	0.6	3.89±0.05	3.94±0.09	0.90
	0.75	4.55±0.05	4.64±0.08	0.80
	0.8	4.75±0.07	4.91±0.11	1.04
	1.0	5.08±0.08	5.05±0.08	0.76
$[0\zeta\zeta]L$	0.1	2.03±0.10	2.00±0.06	0.45
	0.2	3.70±0.08	3.86±0.07	0.7
	0.3	5.11±0.07	4.97±0.09	0.9
	0.4	5.97±0.08	6.23±0.1 (?)	0.85
	0.6	6.38±0.12	6.81±0.11	1.02
	0.75	5.73±0.08	5.66±0.08	0.8
	0.8	5.51±0.07	5.42±0.13	1.3
	0.9	5.19±0.07	5.26±0.08	0.80
	1.0	5.08±0.08	5.05±0.09	0.90

Table III-3-iii-2 (continued).

		Cu	$Cu_{.63}Ni_{.21}Zn_{.16}$	
Branch	ζ	ν(THz)	ν(THz)	Γ(THz)
$[0\zeta\zeta]T_2$	0.1	1.11±0.03	1.18±0.05	0.50
	0.2	2.27±0.04	2.56±0.03	0.30
	0.6	5.71±0.06	5.76±0.10	0.95
	0.8	6.80±0.11	6.81±0.13	1.22
$[\zeta\zeta\zeta]T$	0.1	1.01±0.05	1.14±0.05	0.5
	0.2	1.87±0.06	1.90±0.10	1.0
	0.3	2.66±0.06	2.68±0.06	0.6
	0.4	3.17±0.07	3.06±0.07	0.65
	0.5	3.37±0.07	3.34±0.09	0.84
$[\zeta\zeta\zeta]L$	0.1	2.46±0.07	2.51±0.03	0.30
	0.2	4.54±0.06	4.63±0.07	0.62
	0.3	6.14±0.07	6.08±0.08	0.75
	0.4	7.06±0.10	7.17±0.07	0.70
	0.5	7.40±0.13	7.40±0.10	1.00

Experimental results of the dispersion relation measurements made on the alloy $Cu_{.63}Ni_{.21}Zn_{.16}$; the bars represent the F.W.H.M. of the neutron groups. Uncertainty is typically 1/10th of this value.

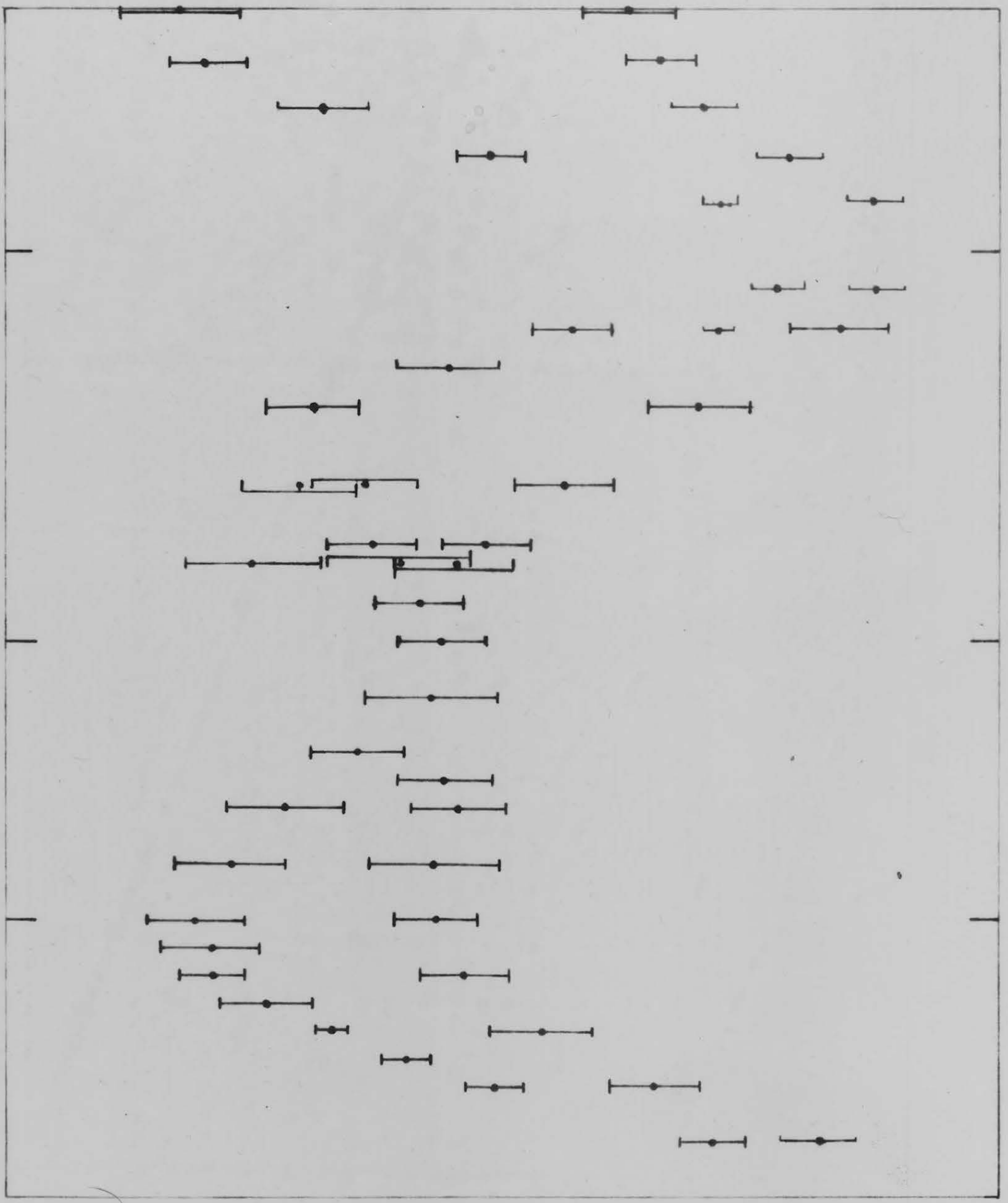

Experimental results of the dispersion relation measurements made on the alloy $Cu_{.63}Ni_{.21}Zn_{.16}$; the bars represent the F.W.H.M. of the neutron groups. Uncertainty is typically 1/10th of this value.

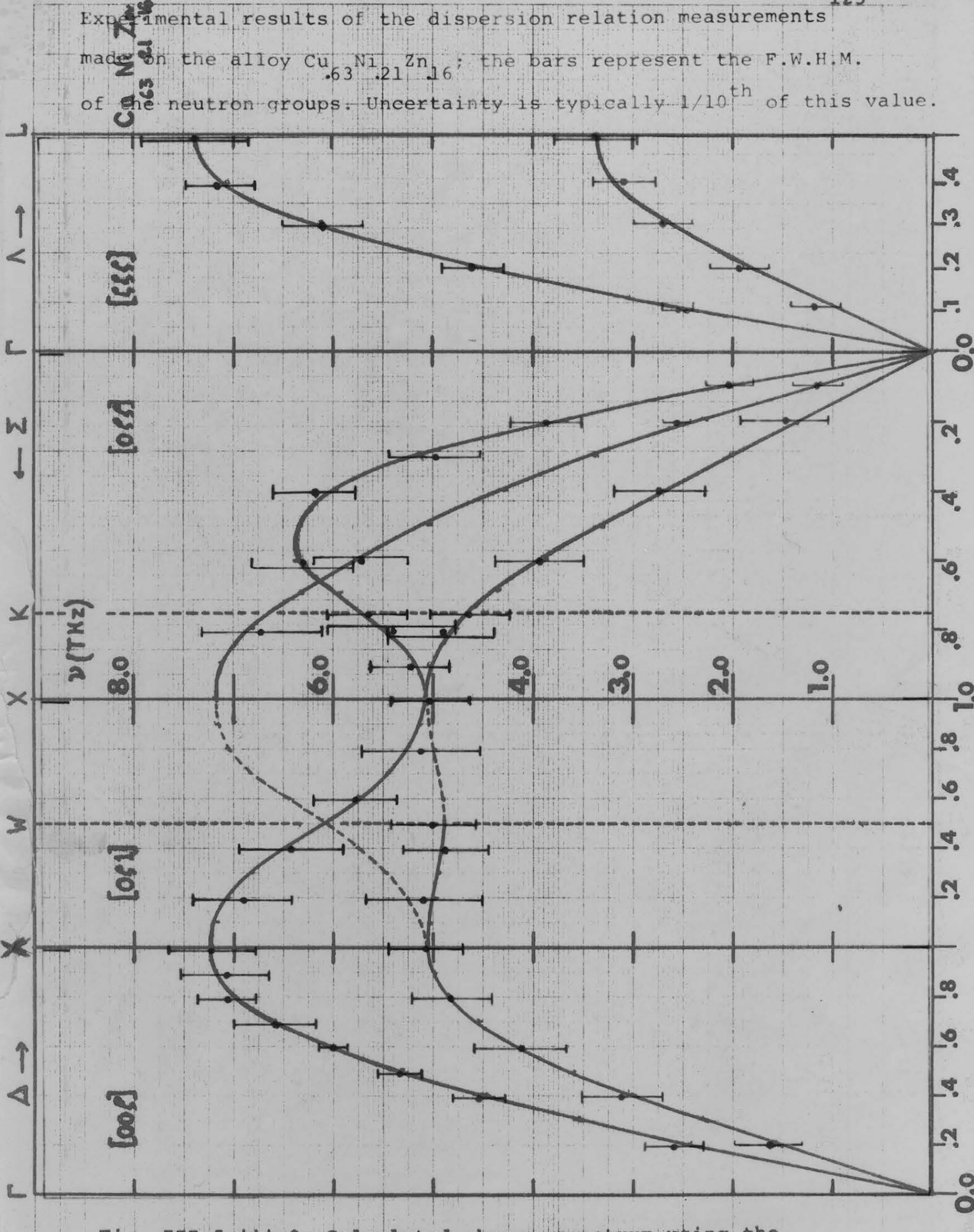

Fig. III-5-iii-3; Calculated phonon spectrum using the force constant of copper (Svensson [67]).

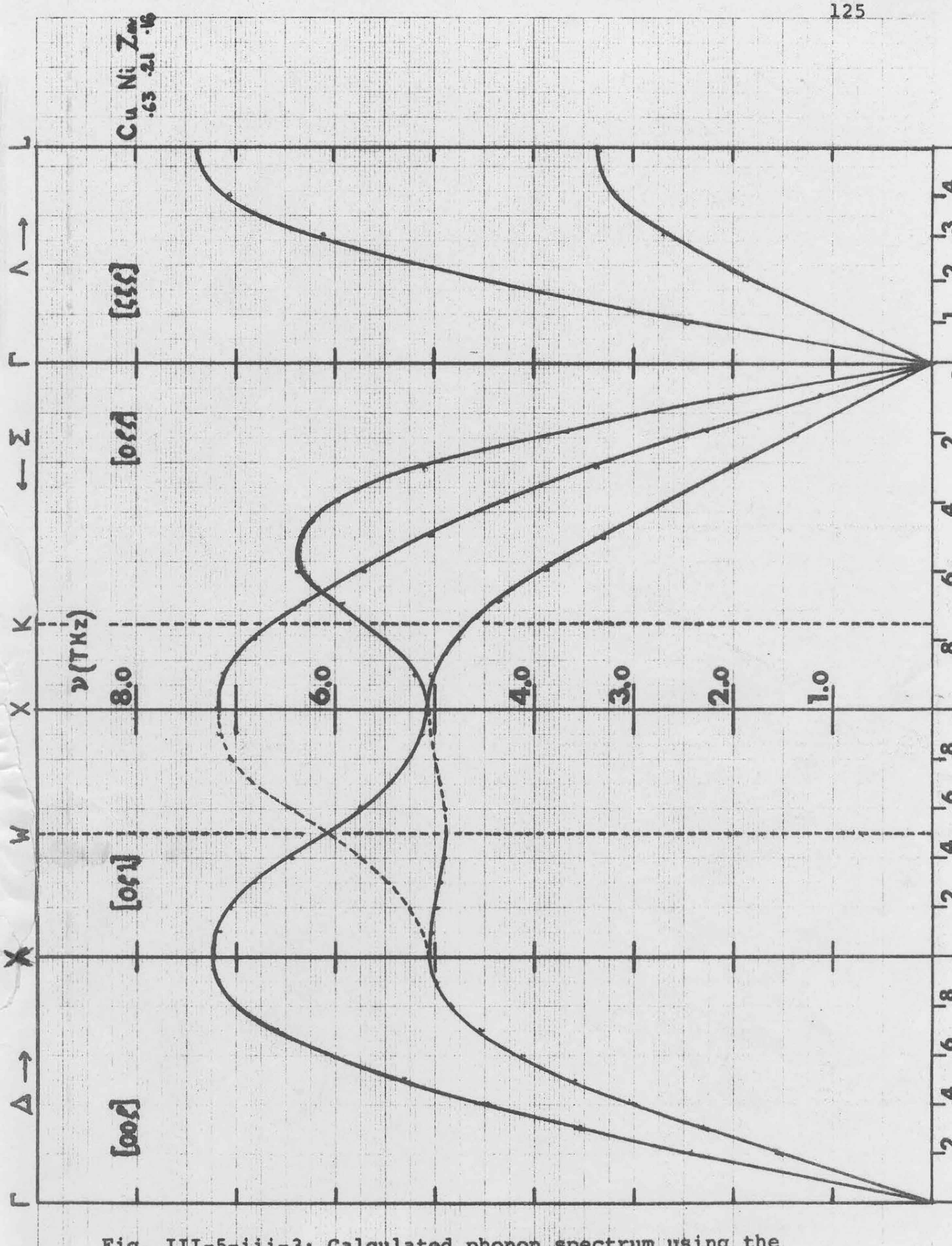

Fig. III-5-iii-3; Calculated phonon spectrum using the force constant of copper (Svensson [67]).

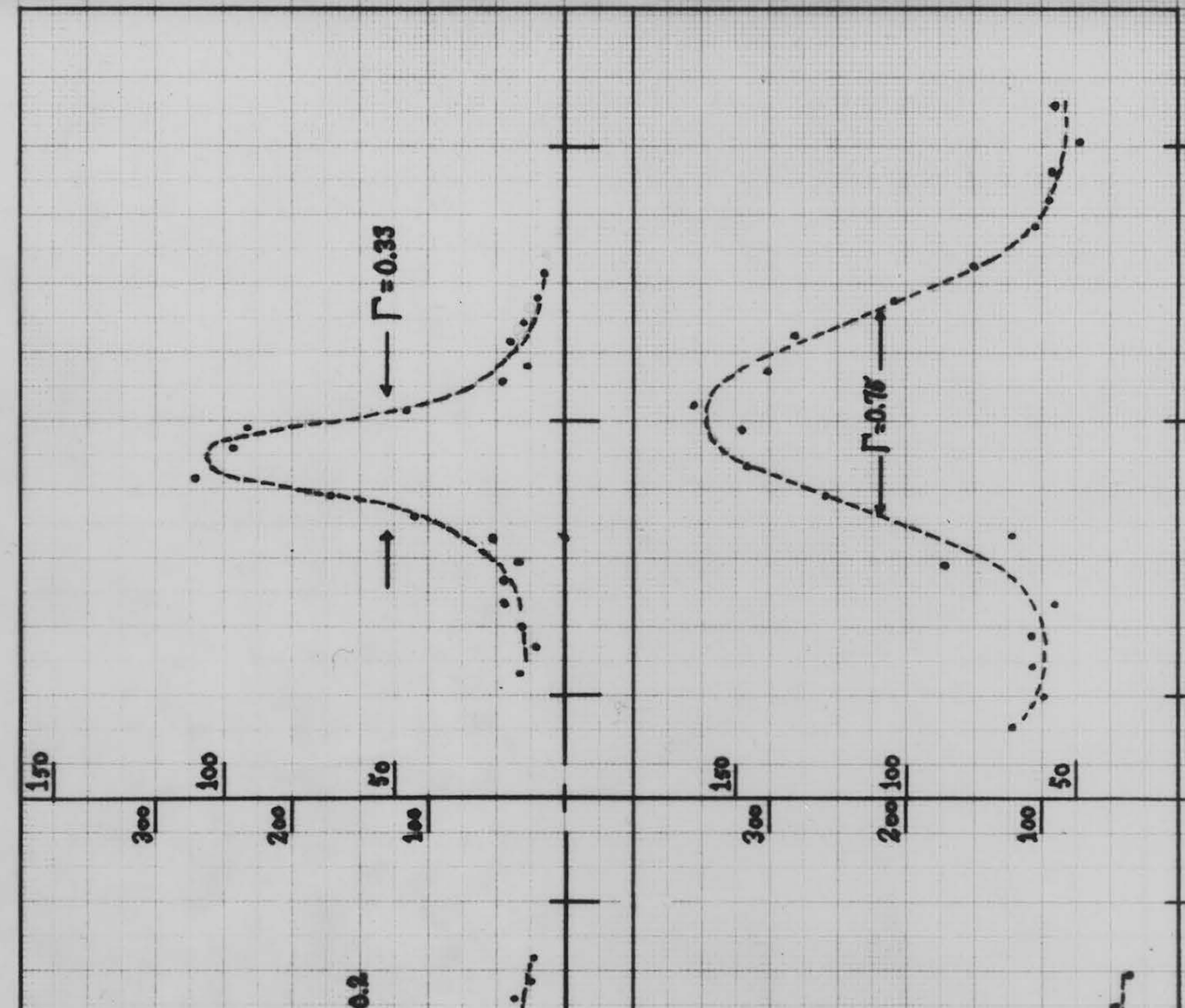

Phonons measured at the same momentum transfer (Q) as on fig. III-5-iii-4, but using a good Cu specimen (by Dr. A.P. Miiller)

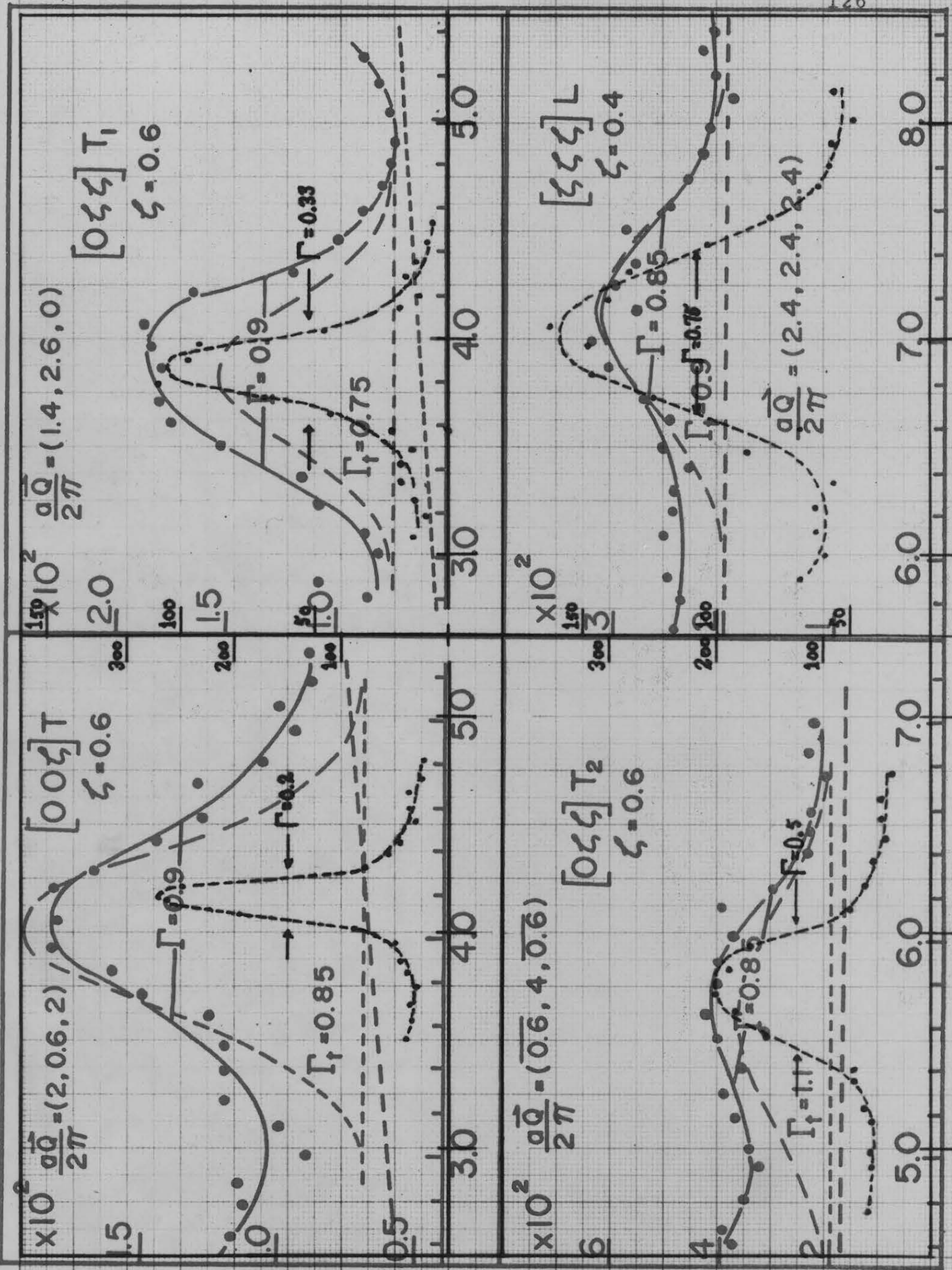

Fig. III-5-iii-4. Some typical neutron groups in $Cu_{.63}Ni_{.21}Zn_{.16}$

Phonons measured at the same momentum transfer (Q) as on fig. III-5-iii-4, but using a good Cu specimen (by Dr. A.P. Miiller)
(—— : experimental; ---- : calculated)

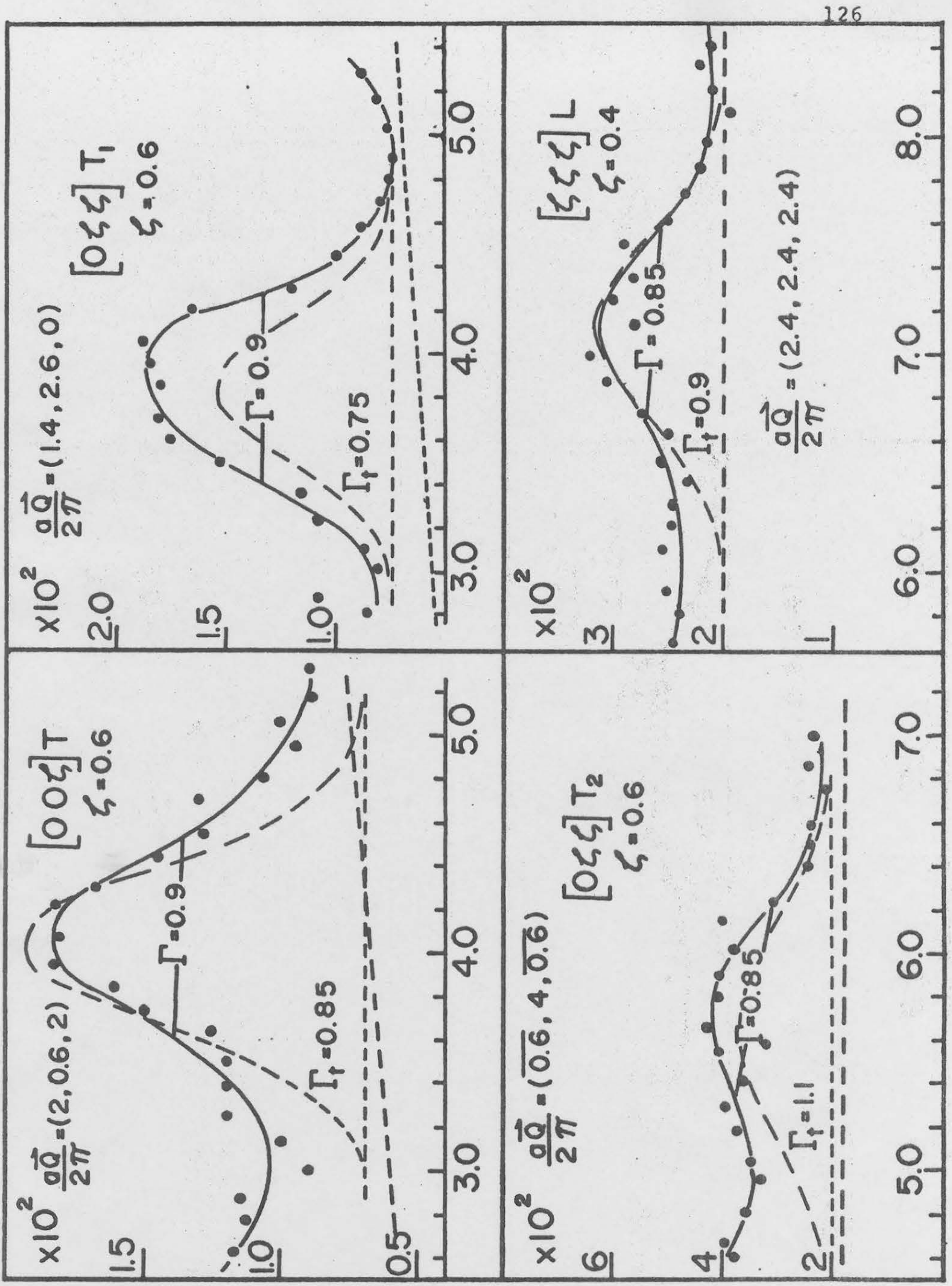

Fig. III-5-iii-4. Some typical neutron groups in $Cu_{.63}Ni_{.21}Zn_{.16}$

(—— : experimental; ---- : calculated)

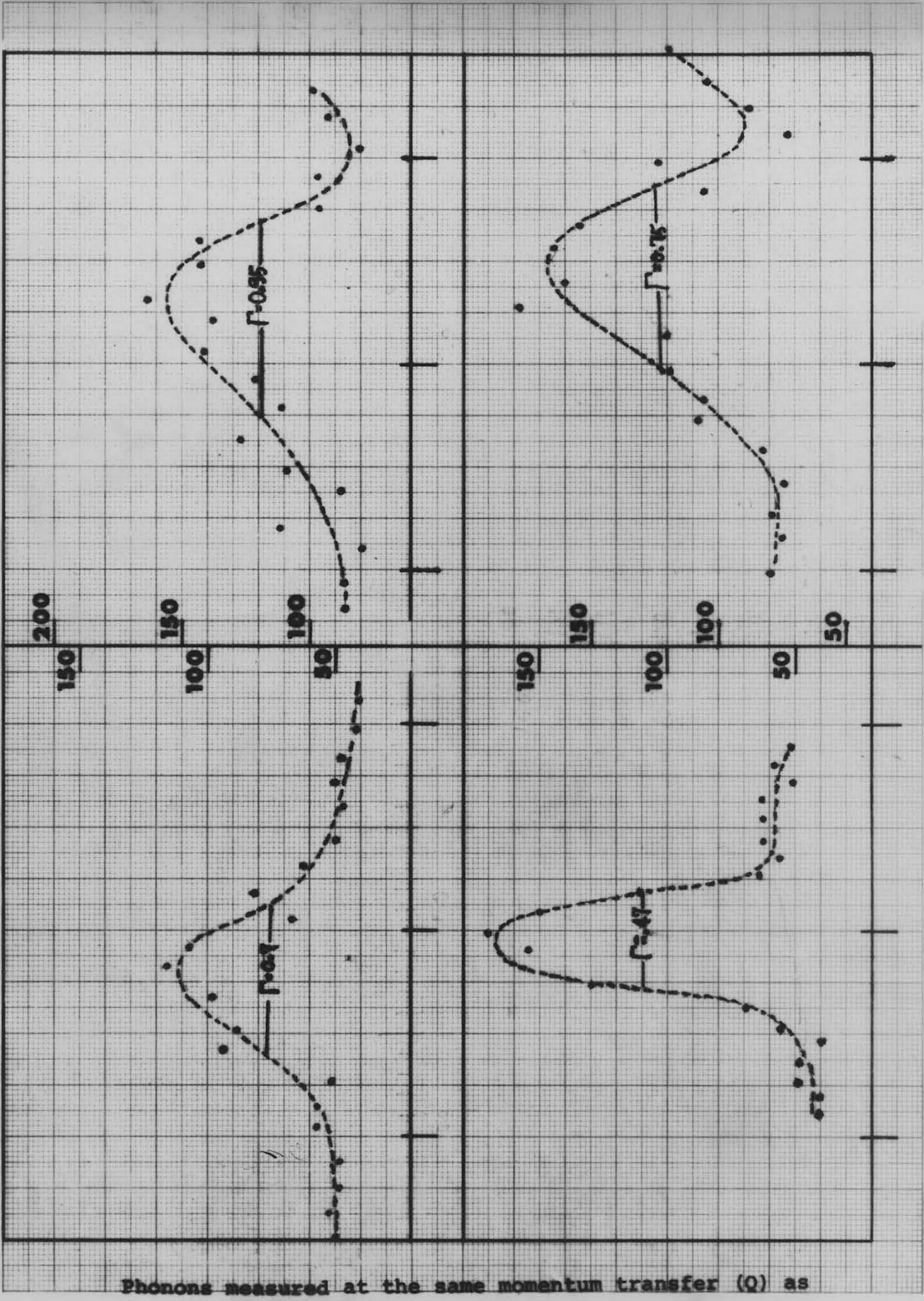

Phonons measured at the same momentum transfer (Q) as on fig. III-5-iii-5 but using a good Cu specimen (by Dr. A.P.Miiller

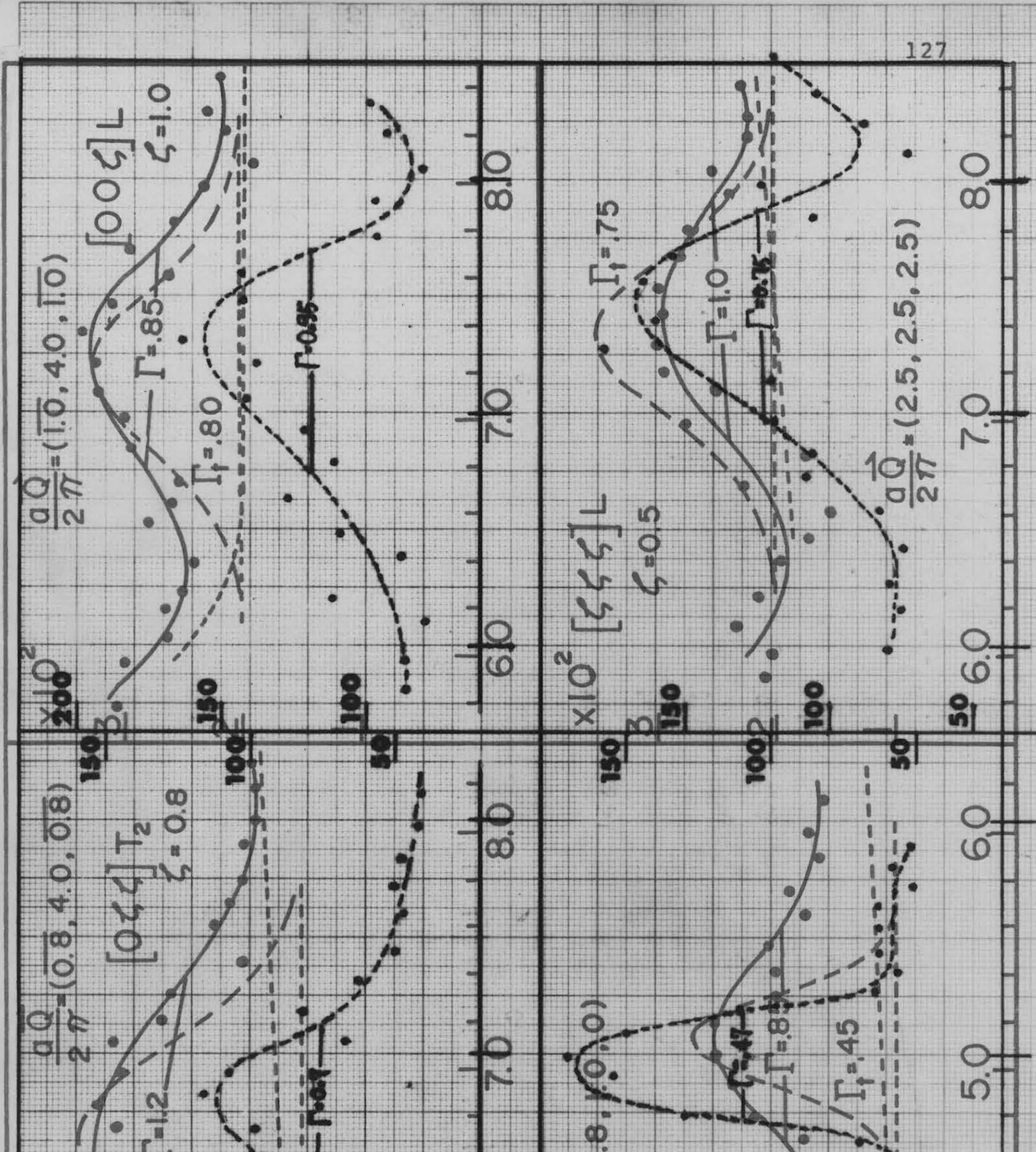

Phonons measured at the same momentum transfer (Q) as on fig. III-5-iii-5 but using a good Cu specimen (by Dr. A.P.Miiller

Fig. III-5-iii-5. Some neutron groups from phonons with zero or non-zero energy q-gradient (——: experimental; ----: calculated)

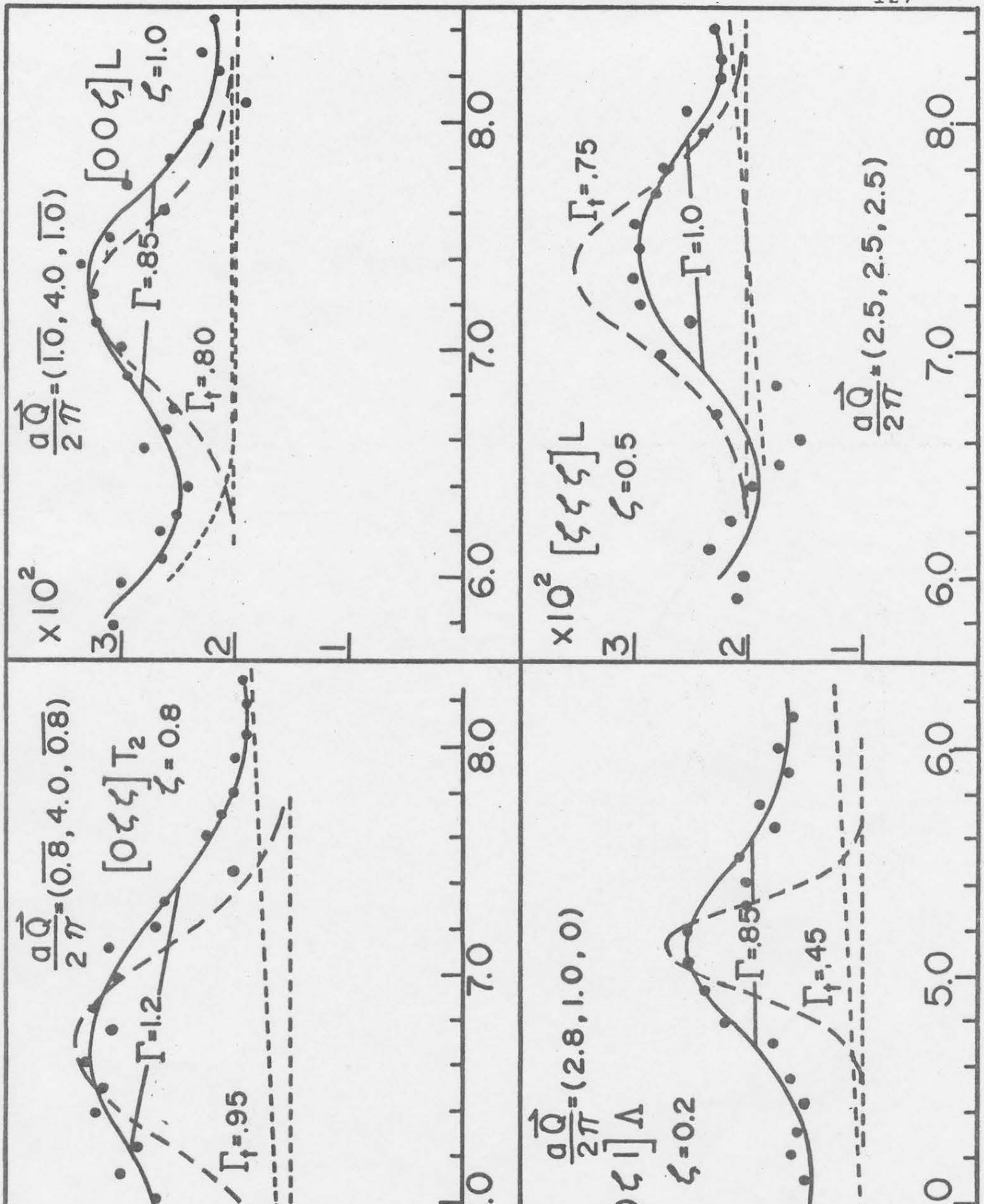

Fig. III-5-iii-5. Some neutron groups from phonons with zero or near-zero energy σ-gradient. (—— : experimental; ---- : calculated)

Appendix A-1; Evaluation of three integrals

i)
$$\int_{\infty}^{\infty} dx\ \exp\{-\tfrac{1}{2}(Ax^2 + Bx)\} \tag{1}$$

Define

$$I_1(a,b) = \int_a^b dx\ \exp\ \{-\tfrac{1}{2}(Ax^2 + Bx)\} \quad (b \geqslant 0,\ b \geqslant a) \tag{2}$$

$$= \exp(\tfrac{X^2}{2}) \int_a^b dx\ \exp\{-\tfrac{1}{2}(\sqrt{A}\ x + X)^2\} \tag{3}$$

where
$$X = B/(2\sqrt{A}) \tag{4}$$

Changing variable to $y = \sqrt{A}\ x + X;\ dy = \sqrt{A}\ dx$

we get

$$I_1(a,b) = \frac{1}{\sqrt{A}} \exp(\tfrac{X^2}{2}) \int_{\sqrt{A}\ a+X}^{\sqrt{A}\ b+X} dy\ \exp(\tfrac{-y^2}{2}) \tag{5}$$

$$= \sqrt{\frac{2\pi}{A}} \exp(\tfrac{X^2}{2}) [\underset{2}{\underline{\mathrm{erf}}}(\sqrt{A}\ b + X) - \underset{2}{\underline{\mathrm{erf}}}(\sqrt{A}\ a + X)] \tag{6}$$

the object $\underset{2}{\underline{\mathrm{erf}}}(y)$ stands for

$$\frac{1}{\sqrt{2\pi}} \int_0^y dx\ \exp(\tfrac{-x^2}{2}) \tag{7}$$

Obviously $\mathrm{erf}(0) = 0$ and $\lim_{M \to \pm\infty} \underset{2}{\underline{\mathrm{erf}}}(M) \to \pm\frac{1}{2}$

Hence we have the desired integral

$$I(-\infty,\infty) = \sqrt{\frac{2\pi}{A}} \exp\ (\tfrac{B^2}{8A}) \tag{8}$$

ii)

$$I_2 = \int_{-\infty}^{\infty}\!\!\int dx_1 dx_2 \exp\{-\tfrac{1}{2}(Ax_1^2 + Bx_2^2 + Cx_1 + Dx_2 + Ex_1x_2)\} \quad (1)$$

$$= \int_{-\infty}^{\infty} dx_1 \exp\{-\tfrac{1}{2}(Ax_1^2 + Cx_1)\} \int_{-\infty}^{\infty} dx_2 \exp\{-\tfrac{1}{2}[Bx_2^2 + (D+Ex_1)x_2]\} \quad (2)$$

we use the result of the previous page and get

$$I_2 = \sqrt{\frac{2\pi}{B}} \int_{-\infty}^{\infty} dx_1 \exp\{-\tfrac{1}{2}(Ax_1^2 + Cx_1)\} \exp\{\tfrac{1}{2} \frac{(D+Ex_1)^2}{4B}\} \quad (3)$$

$$= \sqrt{\frac{2\pi}{B}} \exp(\frac{D^2}{8B}) \int_{-\infty}^{\infty} dx_1 \exp\{-\tfrac{1}{2}[(A-\frac{E^2}{4B})x_1^2 + (C-\frac{DE}{2B})x_1]\} \quad (4)$$

$$= \frac{4\pi}{\sqrt{4AB-E^2}} \exp\{\tfrac{1}{2}[\frac{AD^2 + BC^2 - CDE}{4AB - E^2}]\} \quad (5)$$

as a verification, note that this result is invariant under the transformation $A \leftrightarrow B$
$C \leftrightarrow D$

iii)

$$I_3 = \iiint_{-\infty}^{\infty} dx_1 dx_2 dx_3 \ \exp\{-\tfrac{1}{2}[(Ax_1^2+Bx_2^2+Cx_3^2)+(Dx_1x_2+Ex_1x_3+Fx_2x_3) + (Gx_1+Hx_2+Jx_3)]\} \qquad (1)$$

$$= \iint_{-\infty}^{\infty} dx_1 dx_2 \ \exp\{-\tfrac{1}{2}[Ax_1^2+Bx_2^2)+(Gx_1+Hx_2)+Dx_1x_2]\}$$

$$\int_{-\infty}^{\infty} dx_3 \exp\{-\tfrac{1}{2}[Cx_3^2+(Ex_1+Fx_2+J)x_3]\} \qquad (2)$$

From the first result of this appendix, we get

$$I_3 = \sqrt{\frac{2\pi}{C}} \int_{-\infty}^{\infty} dx_1 dx_2 \ \exp\{-\tfrac{1}{2}[(Ax_1^2+Bx_2^2)+(Gx_1+Hx_2)+Dx_1x_2]\}$$

$$\times \exp\{\tfrac{1}{2}[\frac{(Ex_1+Fx_2+J)^2}{4C}]\} \qquad (3)$$

$$= \sqrt{\frac{2\pi}{C}} \exp(\frac{1}{8}\frac{J^2}{C}) \iint_{-\infty}^{\infty} dx_1 dx_2 \ \exp\{-\tfrac{1}{2}[(Kx_1^2+Lx_2^2)+(Mx_1+Nx_2)+Px_1x_2]\}$$

where $K = A - \frac{E^2}{4C}$ (5a); $L = B - \frac{F^2}{4C}$ (5b)

$M = G - \frac{EJ}{2C}$ (5c); $N = H - \frac{FJ}{2C}$ (5d)

$P = D - \frac{EF}{2C}$ (5e)

Using the second result of this appendix, we get

$$I_3 = \frac{4(2\pi)^{3/2}}{\sqrt{4C(4KL-P^2)}} \exp\{\tfrac{1}{2}[\frac{J^2}{4C} + \frac{LM^2+KN^2-MNP}{4KL-P^2}]\} \qquad (6)$$

If we carry out the substitution of the indentities (5), the final result is:

$$I_3 = \frac{4(2\pi)^{3/2}}{\sqrt{\beta}} \exp\{\frac{1}{2}\frac{\alpha}{\beta}\} \qquad (7)$$

where

$$\beta = 4(4ABC-AF^2-BE^2-D^2C+DEF)$$

$$\alpha = 4(ABJ^2+BCG^2+ACH^2) \qquad (8a)$$

$$-(D^2J^2+F^2G^2+H^2E^2)$$

$$+2(DHEJ+DGFJ+GHEF)$$

$$-4(CDGH+BEJG+AFJH) \qquad (8b)$$

As a verification, observe that both α and β obey the 3 symmetry operations

1) $B \leftrightarrow A$ $H \leftrightarrow G$ $E \leftrightarrow F$ (9a)

2) $B \leftrightarrow C$ $H \leftrightarrow J$ $D \leftrightarrow E$ (9b)

3) $A \leftrightarrow C$ $G \leftrightarrow J$ $D \leftrightarrow F$ (9c)

Appendix A-2; In-pile collimation and vertical divergence.

The general expression for the transmission function of a collimator, i.e. equation II-2-(21), is also valid for vertical divergences. However, the dependence upon the monochromator (or analyser) vertical mosaic spread does not show any (first order) correlation between the magnitude of the scattered wave vector and the vertical angular divergence as was the case in equation II-2-(22) for angular divergences in the scattering plane.

Instead, the reflection probability to go from the vertical angles δ_o to δ_1 is governed by the distribution of properly oriented crystallites whose normal lies in the vertical plane containing Q_m, the momentum transfer in the monochromator, Hence, the contribution to the transmission probability from vertical divergences is proportionnal to

$$\exp[-\frac{1}{2}(\frac{\delta_o^2}{\beta_o^2} + \frac{(\delta_1 + \delta_o)^2}{4\eta'^2\tan^2(\theta_m)})] \qquad (1)$$

For a given value of δ_1, the total contribution from all vertical angles δ_o is obtained by integrating the above expression over δ_o.

Using the result of appendix A-1, this is found to be equal to

$$p_o\exp[-\frac{1}{2}\delta_1^2/(4\eta'^2\tan^2\theta_m + \beta_o^2)\ ] \qquad (2)$$

where $$p_o = [2\pi/(\frac{1}{\beta_o^2} + \frac{1}{4\eta_m'^2\tan^2\theta_m})]^{1/2} \qquad (3)$$

η_m' is the vertical mosaic spread. A similar result applies for the counter collimation.

APPENDIX A-3

Effect of heat and pressure treatments on the neutron reflectivity of germanium monocrystals.

1)-Introduction. It is nowadays an established technique to grow large crystals of germanium and silicon to a high degree of perfection. If the crystal is to be used as monochromator or analyser, a high reflectivity is desired (Dymond[70]).This figure of merit depends on two forms of extinction (Bacon[48], Bacon[62]).

Primary extinction is the effective attenuation taking place from coherent elastic scattering processes as a neutron beam propagates through a perfect crystal. Assume that the beam contains some wavelenght satisfying the Bragg relation for a given direction of propagation of the neutron beam with respect to the crystal (hkl) planes. Each unit cell of the crystal contributes to the scattered amplitude a relative quantity equal to F_{hkl}, the square of its modulus being the structure factor for the unit cell. James[48] calculated the diffracted amplitude from an extended crystal by considering the contributions from each of the successive (hkl) planes; This quantity is equal to

$$q_{hkl}/2 = N_c d^2 F_{hkl}$$

N_C being the number of cells per unit volume,
and d being the interplanar (hkl) spacing.
The value of q_{hkl} is independant of the neutron energy and is typically of the order of 10^{-4} - 10^{-5}. Thus, each plane contributes to the resultant scattered amplitude a quantity of this order relative to the incident amplitude and after n planes, the amplitude of the wave propagating in the forward direction is given by the $(n-1)^{th}$ term of the geometrical progression: $(1 - 10^{-4})^{n-1}$ (neglecting multiple scattering). Here are a few values to illustrate.*

n	penetration distance	$(1 - 10^{-4})^{n-1}$
500	~1000 A	0.986
5000	~ 1 μ	0.89
50000	~ 10 μ	0.32

It is seen that for penetration depth of the order of 1 μ or less, the attenuated beam does not markedly have a different amplitude from the incident beam. In this case, we say that there is negligible primary extinction.

On the contrary, for penetration distances much larger than 1 μ, the incident beam is significantly attenuated and the planes far removed from the crystal surface contribute proportionnaly less to the scattering amplitude; it must also be remembered that the same argument apply to the scattered beam in its propagation toward the external surface of the crystal. Thus, the diffracted intensity effectively comes from

*NOTE: Consideration of multiple scattering should decrease the penetration depth because of destructive interference, in the case of a perfect crystal.

a region within 1 μ of the crystal boundary and any increase in thickness from this value has but little effect on the scattered intensity. The value of this penetration depth is much smaller than that obtained from considerations of true absorption processes; for material of interest in diffraction from crystals, the linear absorption coefficient is of the order of 0.2 cm^{-1}. Thus, nuclear capture processes are negligible compared to elastic scattering processes.

The other form of extinction, i.e. secondary extinction, arises from the fact that single crystals are not usually perfect on a scale much larger than 1 μ, because of the presence of dislocations. The crystallites, as they are called, are small regions of the crystal with no imperfections; the above considerations about perfect crystal structures hold within these regions. This microscopic structure has two consequences of interest for our topic. Firstly, by effectivly reducing primary extinction, the penetration depth within the crystal is increased. This does not mean however that the effects of extinction may be made arbitrarily small just by decreasing the size of mosaic blocks. Successive attenuation of the neutron beam by the sequence of properly oriented crystallites takes place and is known as secondary extinction. Secondly, the fact that the crystallites are distributed in a given angular range results in the width of the scattered intensity distribution being larger than the calculated values for a perfect crystal which are typically of the order of a few seconds of arc (Bacon [62]).

It is known that crystal reflectivities may be improved by decreasing primary extinction through heat and pressure treatments of the crystal. (Hallman-69, Konstantinović-68, Nikotin-69). This appendix refers to the results of such work made on germanium. This is an interesting candidate for monochromator or analyser since its (111) reflection lacks a second-order component. (Barrett [63], Dolling [67]).

2)-Experiments. The crystals that were treated were in the form of thin discs approximatly 70 mm. dia. x 0.38 mm. These were all cut from the same boule and all had a (220) axis nearly perpendicular to their flat face. The figure of merit in the appreciation of the treatment was the integrated reflectivity (at a fixed position, 2Θ, of the counter) defined by

$$R_\Theta = \frac{\int_{-M}^{M} I(\psi)\, d\psi}{I_o}$$

where the interval of integration is extended to contain all contributions to $I(\psi)$ from coherent elastic scattering. Note that I_o is the intensity of the incident beam whose cross-section entirely intercepts the crystal. In practice, a "pinhole" (6 mm. dia.) was used to obtain a pencil-type beam falling entirely on the specimen.

The results of the treatment of the crystal are presented in table A-3-1. The numbers given in that table for the reflectivity are not the absolute reflectivities but correspond to a pseudo-reflectivity value as obtained by putting the same collimation (1/80 horizontally) in $\underset{\sim}{k}_o$ and $\underset{\sim}{k}'$;true reflectivities are measured without any collimation in the scattered beam. Measurements made on the standard with both types of collimations indicate that the true reflectivity is approximatly 50% larger with the proper collimation arrangement than with the special arrangement used. This correction should be the same for all treated slices since their F.W.H.M. is very similar in all but one case; thus the numbers given should be a true picture of the relative efficiency of different treatments in improving the reflectivity

3)-Technique. A germanium single crystal is an extremely hard material and different combinations of heat and pressure treatments were tried in order to facilitate the plastic flow which would increase the mosaic spread of the crystals. The table of results show a continuous increase in the efficiency of the treatments as higher pressures and temperatures were reached, i.e. as the degree of plastic flow was made larger.

For these treatments, a set of flat plates were made that could hold the crystal in the press and at the same time act as a heat reservoir to minimize the rate of cooling while the crystal was brought up to the desired pressure. (Fig. A-3-1). The two parts were arranged to fit into one another so as to shield the crystal from the oxidating atmosphere. The grooves on the sides served as slots for the handling fork used in transfering the plates from the oven to the hydraulic press. The material used was mild steel since it was easier to machine than stainless steel. Mild steel did not resist very well to the high temperatures encountered (circa 900°C); corrosion and pitting occurred on all surfaces after repeated use. This was more objectionable on the inside surfaces (in contact with the crystal) and was compensated by putting the crystal between clean stainless steel shim stocks instead of directly in contact with the steel plates. This gave effective protection from the oxidation and prevented contamination of the specimen by the corroded plates.

4)-Results. The results of table A-3-1 show that a combination of both high temperature and high pressure is necessary in order to see any improvements. Note that the given temperatures do not correspond to the temperatures at which the crystal was being pressed but rather they are the maximum temperatures attained when the steel plates were transfered to the press. The time required for this transfer and to build up the pressure is of the order of one minute. During this time, the inside cavity containing the crystal will have started to cool down but this temperature variation was not measured.

The crystal slice # B-2 was used as a standard; its characteristics are identical to that of any of the other slices before treatment. The value of the F.W.H.M. for the standard may be considered as being contributed exclusively by instrumental resolution since the mosaic width of the untreated crystal is zero for all practical purposes.

The treatment received by slice #C-1 was a sudden cooling from 600° C to 77° K. Sudden cooling is used in X-ray work to increase the mosaic width of too perfect crystals but it had no observable effects in this case.

The treatment made on slices # C-11 and B-3 shows that high pressure or high temperature alone has no effect. In one case, the material is not plastic enough while in the other case, there is no significant external forces to create dislocations. In fact, high temperature alone should decrease rather than increase the density of defects, since the relatively slow cooling rate might effectivly have resulted in an annealing treatment.

Heat/pressure treatments are more spectacular in the case where the upper limits are reached both in temperature (T_{melt}-30°) and in pressure (maximum pressure of the press: 166 atm.).

The crystals withstood these treatments very well from the mechanical point of view. No sign of oxidation was visible, except perhaps as a slight change in colour. Some microscopic cracks, extending a few millimeters, were generally observed but they were not objectionable. This could probably have been avoided by remachining the plates when the internal surfaces became uneven from corrosion.

Results of heat and pressure treatment of germanium monocrystals

(measurements made on (220) reflections, thickness of crystals 0.38 mm.)

Slice no.	R_θ (min.)	F.W.H.M. (deg.) (note 2)	Pressure (Atm.)	Temp. (°K.)	
B-2	0.35	0.3	---	---	Standard
C-1	0.3	0.32	1	875 →77	sudden cooling
C-11	0.36	0.28	166	298	
B-3	0.32	0.33	1	1200	
B-5	0.38	0.34	83	900	
B-7	0.6	0.52	83	1100	
B-8	1.3 1.1	1.0 1.6	155	1200	
B-9+B12	2.2	0.7	83	1200	stack of 2 slices.

1) Note: the 2 sets of data for slice B-8 refer to the two faces of the crystal.

2) Note: F.W.H.M. are uncorrected for instrumental resolution.

3) Note: Melting temperature of germanium: 1227°K (954°C)

Table A-3-1

FLAT PLATES for the HEAT/PRESSURE TREATMENT of GERMANIUM Slices.

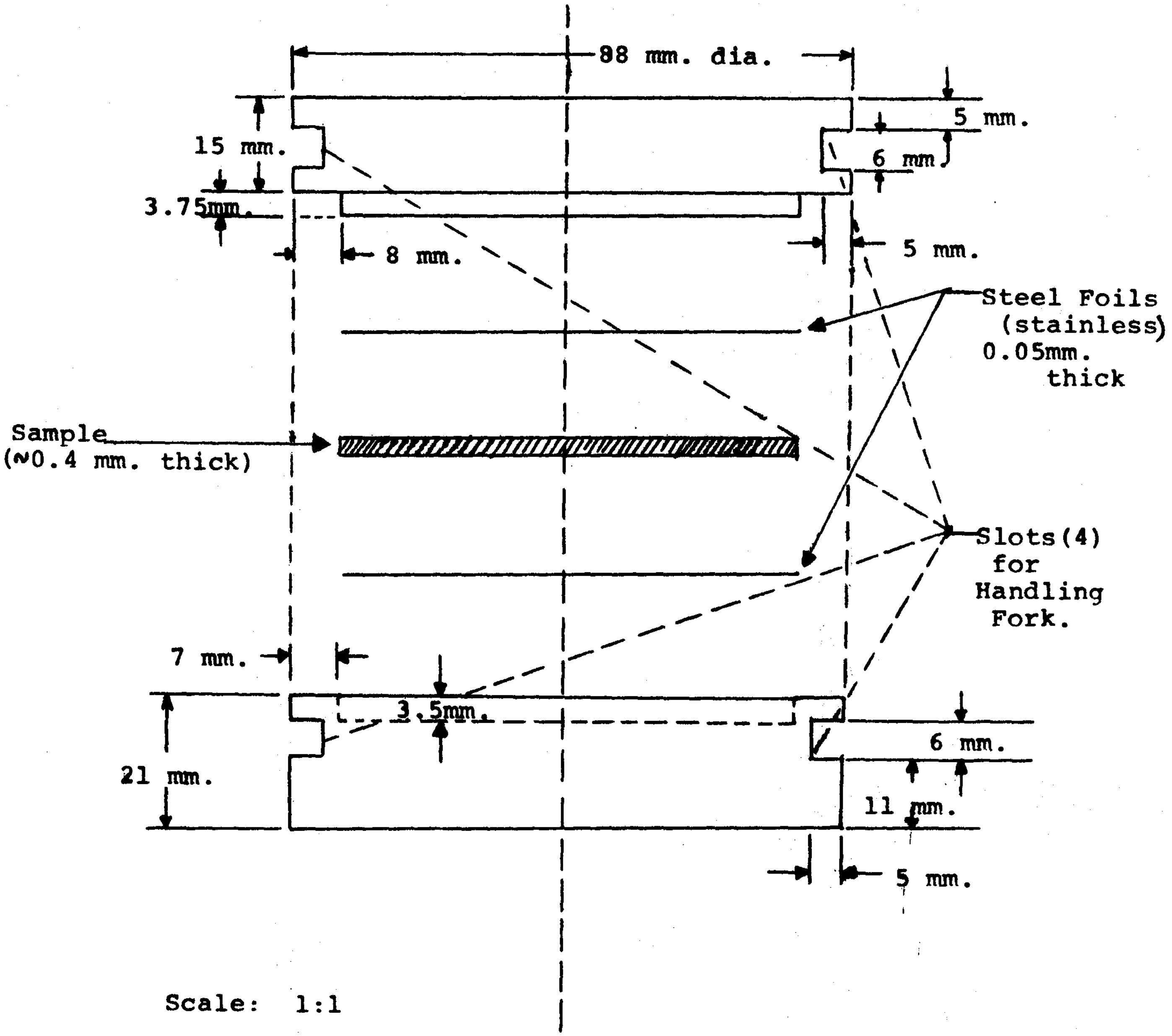

Scale: 1:1

Material: Mild Steel.

Fig. A-3-1

Appendix A-4: Automation of the spectrometer by paper tape; construction of a A.S.C.I.I. decoder.

I - Introduction

The construction of a second McMaster spectrometer at the NRU reactor has motivated an investigation into the possible improvements that could be incorporated in the new instrument. The study described here was concerned solely with the input-output channels portions of the system, mainly for the reason that the judicious design of the control unit and related equipment proper proved to be most satisfactory.

In this appendix, the principle behind a paper tape decoder designed and built in the summer of 1969 is exposed. But before going to this topic proper, it may be appropriate to rapidly describe the system presently used; a detailed description is to be found in Rowe's thesis. (Rowe-66)

II - The Present System

The system presently used on the McMaster Spectrometer is illustrated in block diagram in fig. A-4-1. It consists basically of:

- a main control unit which electromechanically performs logical operations through the use of fast response time (10 ms.) relays.
- an input station which makes use of a IBM card punch (Model 026) and the built-in card duplicator.
- an output station, i.e. a teletype model T-33, fed from a solid state scanner.

- counting circuits and related electronics for the incident beam monitor counter and the analyser signal and background counters.

III - The Problem and a Solution

The general design as described in II proved to be most satisfactory despite the relatively low capital investment involved. However, the use of cards for controlling the instrument suffers from severe drawbacks:

- a card reader is required which adds an important contribution to the cost of the instrument.
- the input and output channels are completely independent so that alphanumeric identifiers cannot be automatically printed with the experimental data.

The basic idea behind the circuit described here is to combine in a single unit the input and output stations. This turns out to be feasible by the fact that the Model T-33 teletype which is needed anyhow on the output section has a duty cycle which never comes in conflict with that of the reader and that it can be simply modified to serve at the same time as an input station. Besides the economy being realized by getting rid of the card punch altogether, it is now possible to couple the input and output channels in a simple way. A block diagram, fig. A-4-1, illustrates the idea.

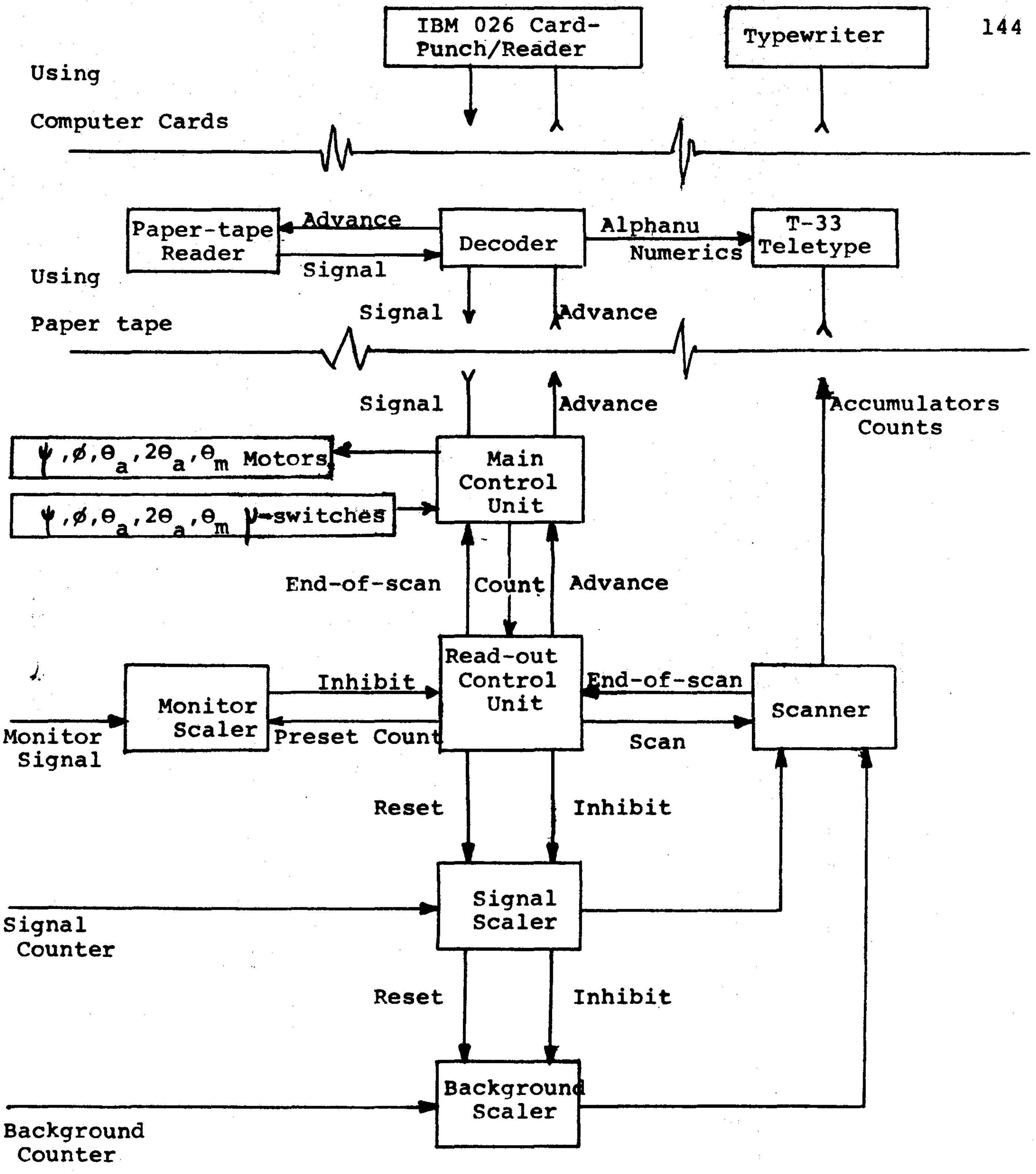

Fig.A-4-1. Block diagram of the Control Section and the Electronics of McMaster Spectrometers (with the two different modes of control: Computer Cards and Paper Tape.)

The heart of the new input-output system is a model T-33 teletype which comes equipped for reading and punching A.S.C.I.I. (American Standard Code for Information Interchange) code paper tape. Actually the punch itself plays a minor role with respect to the circuit described here in the sense that it is used only

a) for manually punching spectrometer commands, the punching task being normally performed by a computer programme.

b) when it is desired to interface the output to a computer via paper tape.

Basically Fig. A-4-1 shows that the card reader is replaced by the paper tape reader. The information punched on the tape can now be used to write on the printer or to control the spectrometer according to the two modes described below. In the case of the control mode, the coded information read from the tape goes through the decoding circuit where it is translated into the proper combination of spectrometer commands.

The need for a decoder arises from the fact that although 7 bits code contains more than enough channel capacity that will ever be needed (2^7 7 bits words) it still does not allow to assign a motor increment (positive or negative) to one and only one perforation, as is possible using 12 bits/column computer cards.

Hence the need for a decoder. As the name indicates, the decoder deciphers the punched information and energizes the appropriate relays in the control unit which now takes over until the desired function is accomplished and an "advance" pulse is sent back to the reader. The cycle is then repeated.

V - Coding

The choice of the actual code corresponding to the different combinations of spectrometer commands was governed by the following considerations.

a) in a general scan in $(\underset{\sim}{Q}-\omega)$ space, three independent angles need to be varied: ψ, ϕ, $\theta_a (2\theta_a)$ or θ_m. Since the efficiency of the spectrometer depends on minimizing the time lost during motor moves, it is of utmost importance to simulataneously vary all three angular positions. The total number of possibilities is thus $3\times3\times3 - 1 = 26$ where one is subtracted corresponding to the case where none of the angles are varied.

b) The spectrometer commands could be punched directly from the teletype keyboard for obvious reasons. (For a list of Standard ASCII characters, please refer to Table A-4-1).

c) The ASCII symbol corresponding to a spectrometer command should be limited to those 64 available on CDC computers, since it might sometimes be desired to check for agreement between the calculated and perforated values. Since, as will be seen, the decoder allows the codes corresponding to each spectrometer command to be written, it is also possible to check for agreement of the written code symbols with those that are to be expected. This eventually would prove a useful diagnosis in cases of technical difficulties affecting the control circuit by allowing the possibility to monitor the behaviour of the front end.

The above consideration suggests to use the letters of the alphabet and the combination of motor moves in a one-to-one correspondence. The truth table corresponding to spectrometer commands, including non-motor-moves is given in table A-4-2.

VI - Alpha Mode and Control Mode

Obviously the above arguments would be poor if it resulted in the loss of the possibility of writing alphanumerics. In order to differentiate between codes corresponding to alphanumeric information and spectrometers commands, it is necessary to define two operating modes, as determined by the position of the bi-stable K-13:

a) The alpha modes where all ASCII characters can be read and printed at the rate of 10 characters/second (Table A-4-1), except ASCII code 074_8, which is used for switching from alpha to control mode.

b) The control mode where a limited number of characters corresponding to spectrometer commands may be read as illustrated in Table A-4-2.

Referring to the circuit diagram, it is seen that the alpha mode corresponds to K-13 being de-energized while the control mode corresponds to K-13 being locked energized. Within the control mode itself, there is yet two other submodes: (as determined by the bi-stable K-23). (fig. A-4-3)

b1) The θ_a mode where ψ, ϕ, $\theta_a(2\theta_a)$ may be simultaneously moved. This corresponds to K-23 being de-energized.

b2) The θ_m mode where ψ,ϕ,θ_m may be simultaneously moved. This corresponds for K-23 being locked energized.

VII - Manual and Computer Programmed Operation.

1. Manual Operation

Using the truth table, it is possible to manually program a spectrometer scan. The procedure is as follows:

i) in the alpha mode, any keyboard character except code 074_8 may be punched. This may be called the editing section.

ii) immediately preceding the first spectrometer command, ASCII character 074_8 (i.e."bra"<) is punched.

iii) Spectrometer commands are punched according to the truth table, table A-4-2.

iv) when it is desired to return to the alpha mode, the ASCII code 276_8 (i.e."ket">) is punched. The punched information is now as per i), and the cycle may repeat.

The resulting tape is now fed into the tape reader and automatic operation takes over.

Besides the bra and ket symbols, there exists others which are not related to motor moves and which are now explicitly defined.

a) Space: the detection of the corresponding code by the decoder results in no spectrometer commands. It is to be used in cases where the direction of the motor is reversed and where a time delay of the order of 15 seconds is desired before receiving the next advance pulse.

b) Rub-out: This serves the same purpose in both the alpha and control modes i.e. by perforating all 8 channels, it results in the same effect as in a). This is to be used in mistake correction.

c) $: Reactor time is precious and this symbol represents the "count" command.

d) •: at this end of a scan, this symbol releases the line counter.

e) 1: it signifies a change from moving θ_m to moving $\theta_a (2\theta_a)$
2: it is the reciprocal of the previous code

Note: the meaning of these codes is as above only in the control mode. Otherwise they are alphanumeric characters having no influence on the spectrometer.

2. Computer programmed operation.

The spectrometer may be controlled automatically to perform an arbitrary scan in $(\underset{\sim}{Q},\omega)$ space by reading a tape punched by a computer programme which does the necessary calculations to move any of the four angular variables in the appropriate way. The adopted procedure is the following: calculations are performed on a C.D.C. computer (either at McMaster or at Chalk River) since these are the fastest machines in both locations. Neither of these gives a punched output though. The interfacing between the C.D.C. machines and the Bendix G-20 (Chalk River) which does give a punched output is done through punched cards. A simple translation programme (named PAPYRUS) was written for the G-20 to convert to the appropriate A.S.C.I.I. code. The tape then contains both the coded angular increments and the editing section to be written besides the experimental data.

The characters given in table A-4-3 (part 1) are all legal in A.S.C.I.I. and may be used freely. They correspond to the standard characters available on a card punch and they have the same Hollerith representation in both the C.D.C. and Bendix machines.

Those given in table A-4-3 (part 2) are special characters which are not all legal in A.S.C.I.I. and which have a different Hollerith representation in both types of computers.

Table A-4-4 lists those which may be converted to A.S.C.I.I. via a different representation in G-20 display code (compare with table A-4-3 part 2). This table A-4-4 also includes the internal representations of the special purposes characters, i.e. bra <, ket >, line feed ↑ and carriage return →. Thus the editing section may contain any of the characters listed in tables A-4-3 (part 1) and A-4-4 excluding the followings:

→ : Hollerith code 0-8-5
↑ : "" " 11-8-5
< : " " 12-8-2

(The ket > is allowed as an ordinary alphanumeric character).

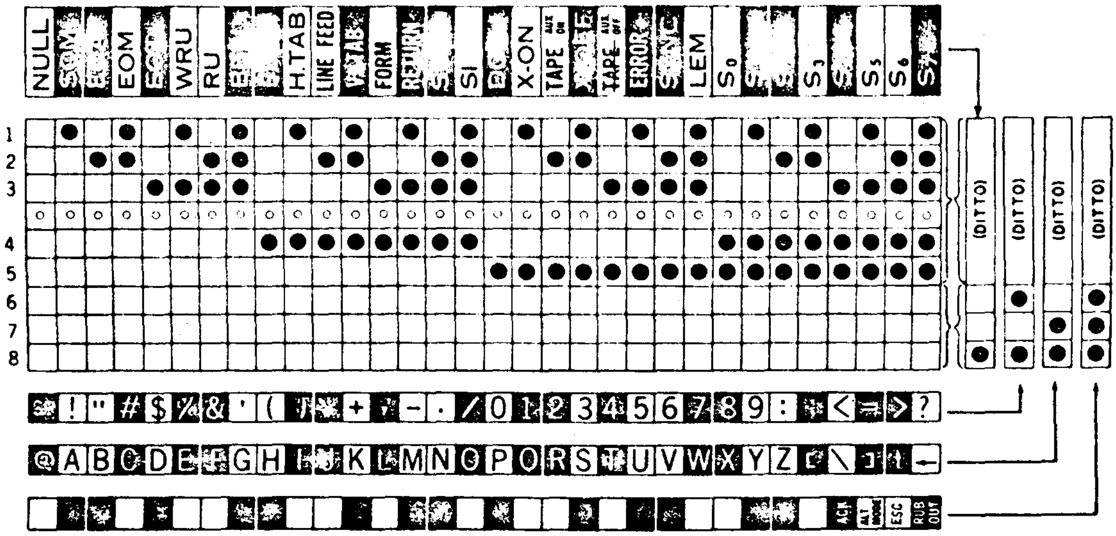

Table A-4-1: CHARACTER ARRANGEMENT (ASCII CODE)

VIII- Truth Table for Paper Tape Coding (Control mode).

Table A-4-2.

a)-Motor-moves symbols

ψ	ϕ	θ_a/θ_m		Coding									Symbol
				1	2	4	Sprocket holes	1	2	4	1	2	
0	0	+		x							x		a
0	0	−			x						x		b
0	+	0				x					x		d
0	−	0						x			x		h
+	0	0							x		x		p
−	0	0		x	x						x		c
0	+	+		x		x					x	x	e
0	−	+		x				x			x	x	i
0	+	−			x	x					x	x	f
0	−	−			x			x			x	x	j
+	0	+		x					x		x	x	q
−	0	+		x	x				x		x		s
+	0	−			x				x		x	x	r
−	0	−		x	x	x			x		x	x	w
+	+	0				x			x		x	x	t
−	+	0		x	x	x					x		g
+	−	0						x	x		x	x	x
−	−	0		x	x			x			x		k
+	+	+		x		x			x		x		u
−	+	+				x		x			x	x	L
+	−	+		x				x	x		x		y
+	+	−			x	x			x		x		v
−	−	+		x		x		x			x		m
−	+	−			x	x		x			x		n
+	−	−			x			x	x		x		z
−	−	−		x	x	x		x			x	x	o

b)-Non motor-moves symbols

	1	2	4	Sprocket holes	1	2	4	1	2	Symbol
Change from alpha-mode to control-mode . . .			x		x	x	x			< (Bra)
Change from control-mode to alpha-mode		x	x		x	x	x		x	> (Ket)
Skip							x		x	Space
Skip(alternate).	x	x	x		x	x	x	x	x	Rub-out
Count.			x				x			$
Release Line Counter . .		x	x		x		x			.(Full Stop)
θ_a Mode.	x				x	x		x		1
θ_m Mode.		x			x	x		x		2

Table A-4-3 (part 1)

X)- Representation of characters in different codings.

Character	C.D.C. display code (Octal)	G-20 display code (Octal)	(Octal) A.S.C.I.I.		Hollerith card
			7-bits	8-bits (even-parity)	
A	01	01	101	101	12-1
B	02	02	102	102	12-2
C	03	03	103	303	12-3
D	04	04	104	104	12-4
E	05	05	105	305	12-5
F	06	06	106	306	12-6
G	07	07	107	107	12-7
H	10	10	110	110	12-8
I	11	11	111	311	12-9
J	12	12	112	312	11-1
K	13	13	113	113	11-2
L	14	14	114	314	11-3
M	15	15	115	115	11-4
N	16	16	116	116	11-5
Ø	17	17	117	317	11-6
P	20	20	120	120	11-7
Q	21	21	121	321	11-8
R	22	22	122	322	11-9
S	23	23	123	123	0-2
T	24	24	124	324	0-3
U	25	25	125	125	0-4
V	26	26	126	126	0-5
W	27	27	127	327	0-6
X	30	30	130	330	0-7
Y	31	31	131	131	0-8
Z	32	32	132	132	0-9
0	33	40	060	060	0
1	34	41	061	261	1
2	35	42	062	262	2
3	36	43	063	063	3
4	37	44	064	264	4
5	40	45	065	065	5
6	41	46	066	066	6
7	42	47	067	267	7
8	43	50	070	270	8
9	44	51	071	071	9
+	45	54	053	053	12
-	46	55	055	055	11
*	47	56	052	252	11-8-4
/	50	57	057	257	0-1
(	51	70	050	050	0-8-4
)	52	73	051	251	12-8-4
$	53	65	044	044	11-8-3
=	54	60	075	275	8-3
blank/space	55	00	040	240	blank
,	56	37	054	254	0-8-3
.	57	53	056	056	12-8-3

Note: All these characters have the same Hollerith Card representation in both the C.D.C. and G-20 computers.

X)- Representation of characters in different codings.

Table A-4-3 . (part 2).

Character	C.D.C. display code (Octal)	Hollerith card (C.D.C.)	G-20 display code (Octal)	Hollerith card (G-20)	(Octal) A.S.C.I.I. 7-bits (octal)	8-bits (even-parity)
≡	60	0-8-6			007	207
[	61	8-7	71	0-8-5	133	333
]	62	0-8-2	72	0-8-6	135	335
:	63	8-2	76	0-8-2	072	072
≠	64	8-4	62	11-8-2		
→ **	65	0-8-5	35	11-8-7	015**	215**
∨	66	11-8-2	61	12-8-7		
∧	67	0-8-7	63	12-8-6		
↑ **	70	11-8-5	75	12-8-2	012**	012**
↓	71	11-8-6	74	8-7		
< **	72	12-8-2	64	11-8-5	074**	074**
> **	73	11-8-7	66	11-8-6	076**	276**
≤	74	8-5				
≥	75	12-8-5				
¬	76	12-8-6	36	12-8-5		
;	77	12-8-7	67	8-4	073	273

1) Note: These characters have different Hollerith card representations in the C.D.C. and G-20 computers.

2) Note: The 4 symbols followed by a double asterisk are special purposes characters:

-C.D.C. display code 65 is translated into carriage return of the teletype (code 215)

-C.D.C. display code 70 is translated into line feed of the teletype (code 012)

-C.D.C. display codes 72 and 73 (bra and ket) respectively preceeds and follows a series of spectrometer commands.

XI)- Intermediate representation for characters having different Hollerith codings in C.D.C. and G-20 systems.

This table gives the G-20 display code corresponding to Hollerith card coding in C.D.C. system for symbols listed to the left.

The final A.S.C.I.I. code obtained by table look-out is given to the right.

Character	C.D.C. display code (Octal)	Hollerith card (C.D.C.)	G-20 display code (Octal)	(Octal) A.S.C.I.I.	
				7-bits	8-bits (even-parity)
≡	60	0-8-6	72	007	207
[	61	8-7	74	133	333
]	62	0-8-2	76	135	335
:	63	8-2	33	072	072
→**	65	0-8-5	71	015	015
↑**	70	11-8-5	64	012	012
<**	72	12-8-2	75	074	074
>**	73	11-8-7	35	076	076
;	77	12-8-7	61	073	073

Note: Concerning the starred symbols, please refer to note 2) in table A-4-3.

Table A-4-4

XII- Modification to the wiring of the teletype;

Paper tape reader circuit. (fig. A-4-2)

S: On/off/end-of-tape switch

C1: Connector to decoder

C6: Teletype connector no. 6

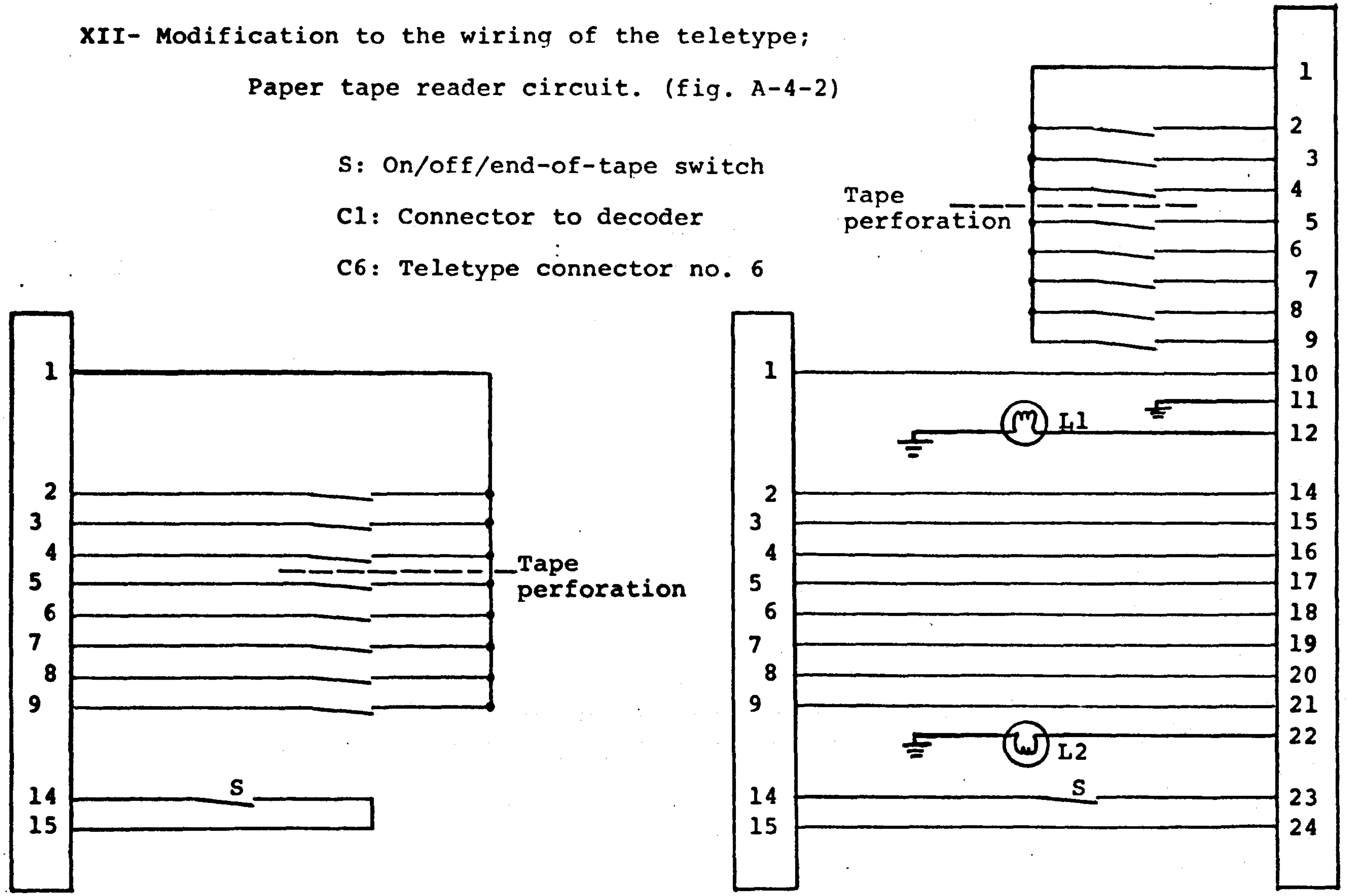

(C6) Initial circuit

(C6) Modified circuit (C1)

XIII- Circuit diagram of the decoder (fig. A-4-3)

Pins of connector C1

1: +24 V. to reader contacts (8)
2-9: From reader contacts (8)
10: Teletype write-inhibit
12+22: To incandescent lamps (2)
14-21: Teletype write signal
23-24: Teletype advance

Pins of connector C-2

1-2: Analyser motors
3-4: Phi-motor
5-6: Psi-motor
7-8: Monochromator motor
9: skip)
10: Count) 9&10: Release
14: Advance pulse

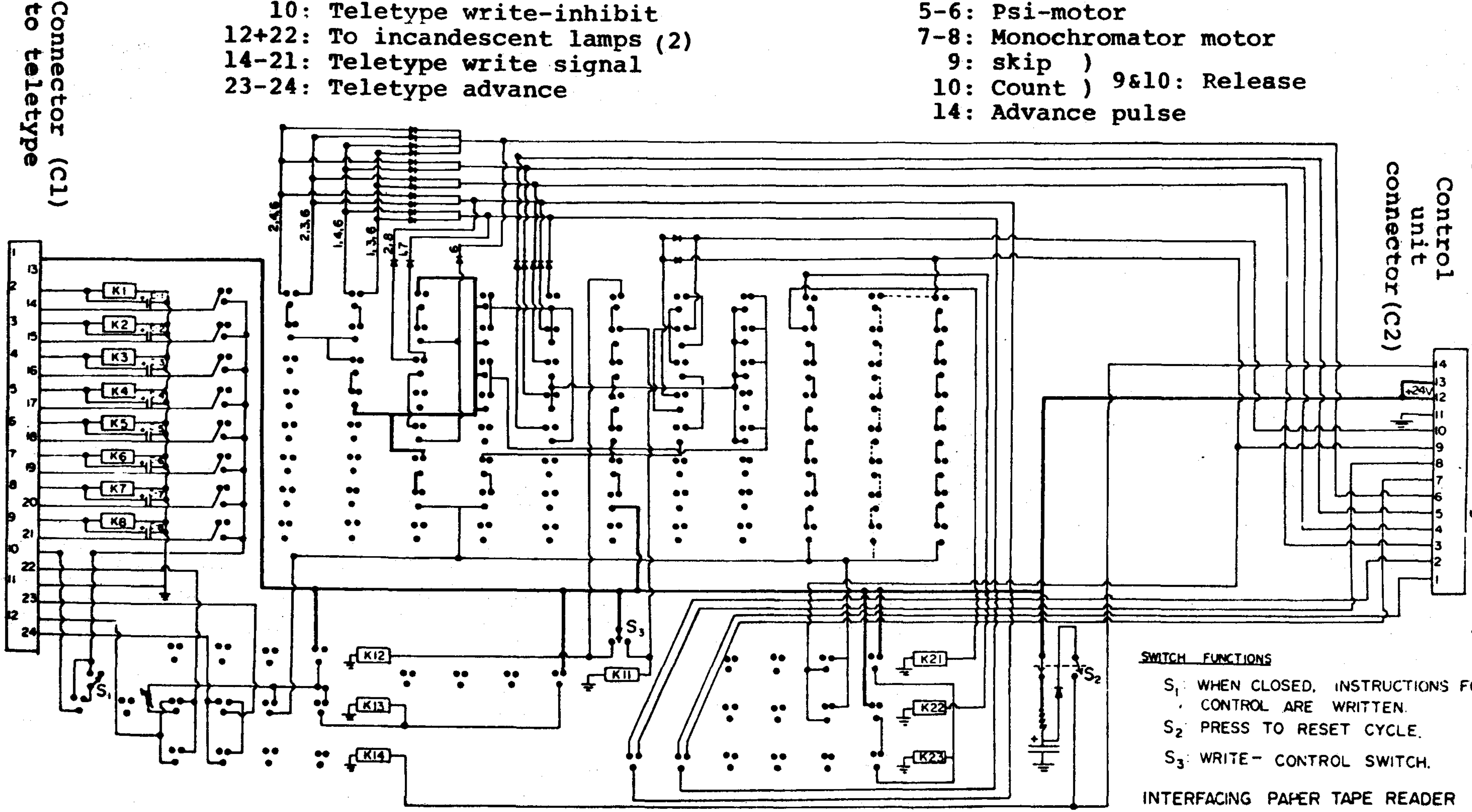

SWITCH FUNCTIONS

S_1: WHEN CLOSED, INSTRUCTIONS FOR CONTROL ARE WRITTEN.

S_2: PRESS TO RESET CYCLE.

S_3: WRITE- CONTROL SWITCH.

INTERFACING PAPER TAPE READER TO CONTROL UNIT.

A.S.C.I.I. DECODER

21-OCT-1969, A.L

Appendix A-5

Design of a self-protected motor/clutch control circuit

Purpose: i) to allow the motors to be energized continuously during an angular scan instead of being pulsated as is presently the case, resulting in:

- an increase in average angular speed
- reduced heating of the motor
- higher torque

ii) to allow a certain dead time (τ) sufficient for the motor to stop completly before reversing direction.

iii) to protect the system against jamming of the moving parts (especially the 0 arm).

The circuit is illustrated in fig. A-5-1. Basically it can be divided in 3 parts: the motor-control (part 1), the self-protection (part 2) and the cut-off relay (part 3).
Part 1 contains a bistable made up of relays A-1 and A-2 which can be locked in two configurations,"forward" or "reverse", depending whether points P-3 or P-4 have a voltage level. After locking in either configuration, a thermal delay relay (of time constant τ) is energized to delay the application of power to the motor; this time lapse is sufficient to allow the motor to stop if it was previously turning in the opposite direction. Once the motor is started, it will be continuously energized

unless the direction of motion is reversed or a counting period is started.

Part 2 is a protection circuit which would energize the relay D-1 should the spectrometer jam against an obstacle. Then the clutch and relay A-3 would be energized for a longer time than the time constant of the delay circuit and relay D-1 would become energized, thus cutting power to the motor and the clutch, until manually resetted by temporarily opening the switch S-2. This feature is intended to be used only on the Ø motor where obstacles may be encountered along a scan; for the other motors, this part may be avoided completly by connecting directly point P-1 to point P-2.

Part 3 is a relay which turn the power off during a count period, thus stopping the motor. Obviously only one such relay is needed if this circuit is installed on more than one motor.

This appendix was included for future reference since the circuit has not been built yet. Installation should be simple since it is only a straightforward insertion between the control unit and the motor without modifying either of these.

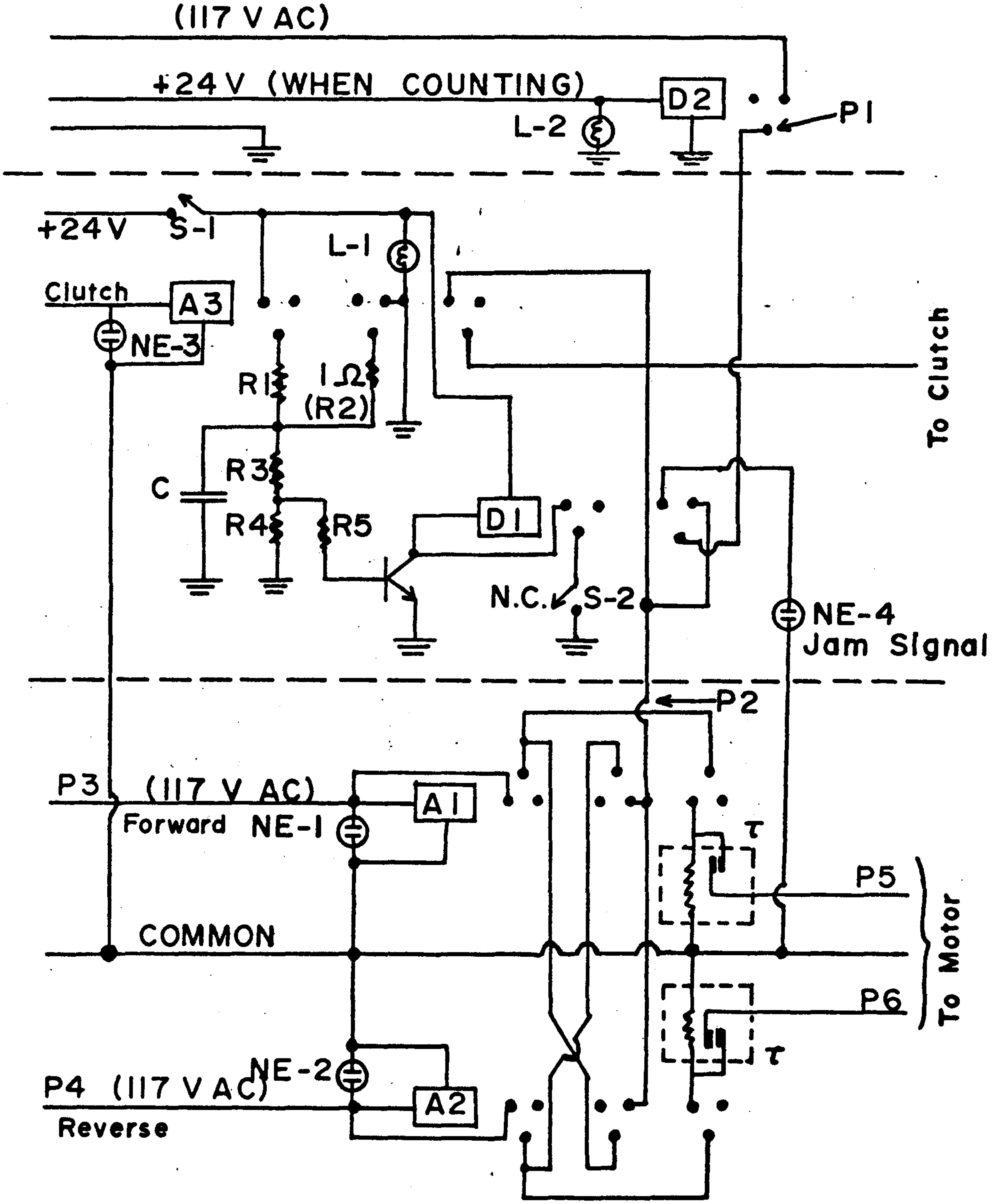

Fig. A-5-1; Motor/Clutch Control (Self-Protected)
Legend: A1,2,3: AC Relays; D1,2: DC Relays.
L-1,2: 24 V Lamps; NE-1,2,3,4: Neon Lamps
τ: Thermal Delay Relay

Appendix A-6

Bibliography of papers relevant to the scattering of thermal neutrons.

A search was done through the scientific litterature in order to collect in a bibliography papers relevant to the scattering of thermal neutrons. The earliest year surveyed was arbitrarily set as mid-1962 and the search covered the journals listed in table A-6-2. Most of the title collecting was done in cooperation with R. Dymond but recent updatings were done more fairly by requiring all people in our group to cooperate.

Up to the beginning of 1970, we have 1828 references relevant to experimental work and 649 relevant to theoretical and technical subjects; these numbers include cross-references. This amount of data has created a certain handling problem which was finally solved, after trying other unsatisfactory methods, by the present procedure which is now briefly described.

Individual references are stored on computer cards according to the format listed in table A-6-1. This format is compatible with that required by the computer library program KWIC (Key Words In Context) which is a general SCOPE programme to do alphabetical sorting. The duplication of columns 201-240 from columns 41-80 initially stems from this reason. It also serves as a check that each reference record is complete.

Since the programme KWIC is not presently working reliably, a computer programme (named BARBARA) was written which could serve our own special purpose since the sorting of chemical formulae is not stricly an alphabetical sorting as a moment reflection shows. Every time that an updating is performed, two copies of a magnetic tape are obtained as a safeguard against accidental erasure.

It is hoped that this work will be annually distributed to interested research groups.

Table A-6-1; Format for reference records as adopted for computer programme BARBARA

I) Experimental papers.

(3 cards per reference records)

Col.	1-40	Journal reference using standard abbreviation
	41-72	formula
	73	Blank
	74-80	Catogory of work using standard code
	81-200	Authors list
	201-240	duplicate of col. 41-80

II) Theoretical and technical papers

(3 cards per reference records)

Col.	1-40	Journal reference using standard abbreviation
	41-80	Authors list
	81-200	Title of paper
	201-240	Duplicate of col. 41-80

Table A-6-1; Journals and the first issue surveyed.

Acta Cryst.	Vol. 16 (1963)
Ann. de Phys.	Serie 13, tome 8
Ann. of Phys.	Vol. 21 (1963)
Can. Journ. Phys.	Vol. 41 (1963)
Comptes Rendus	Tome 256 (1963)
Dissertation Abstracts	Vol. XXIV (1963-4)
Journ. App. Phys.	Vol. 34 (1963)
Journ. Phys. Chem. Sol.	Vol. 24 (1963)
Nucl. Inst. Met.	Vol. 20 (1963)
Phys. Rev.	Vol. 129 (1963)
Phys. Rev. Lett.	Vol. 10 (1963)
Phys. Stat. Sol.	Vol. 1 (1962)
Phys. Lett.	Vol. 1 (1962)
Proc. Phys. Soc.	Vol. 81 (1963)
Proc. Roy. Soc.	Vol. 271 (1963)
Rev. Scient. Inst.	Vol. 34 (1963)
Sol. Stat. Comm.	Vol. 1 (1963)
Sov. Phys. J.E.T.P.	Vol. 16 (1963)
Sov. Phys. Sol. State	Vol. 4 (1962)

Also surveyed were :

The proceedings of I.A.E.A. symposia held in Vienna (1960), Chalk River (1962), Bombay (1964) and Copenhagen (1968).

BIBLIOGRAPHY

Bacon, G.E., Lowde, R.D., Acta Cryst. 1, 303 (1948).

Bacon, G.E. Neutron Diffraction, Sec. Ed. (1962), Oxford University Press.

Bak, T.A. Editor, Phonons and Phonon Interactions, Aarhus Summer School-1963, W.A. Benjamin Inc. New York (1964) Paper by B.N. Brockhouse.

Barrett, C.S., Mueller, M. H. and Heaton, L., Rev. Scient. Inst. 34, 847 (1963).

Brockhouse, B.N., Inelastic Scattering of Neutrons in Solids and Liquids. (IAEA, Vienna) 113, (1961).

Brockhouse, B.N., Arase, T., Caglioti, G., Rao, K.R. and Woods, A.D.B., Phys. Rev. 128, 1099, (1962).

Brockhouse, B.N., deWit, G.A., Hallman E.D., and Rowe, J.M. Neutron Inelastic Scattering, Vol. 2 IAEA Vienna 259, (1968).

Coles, J. Inst. Met. 84, 346 (1956).

Cooper, M. J., Nathans R., Acta Cryst. 23, 357 (1967).

Copley, J.R.D. Ph.D. Thesis (unpublished) McMaster University (1970).

Cowley, E.R., Pant, A.K., Acta Cryst. to be published (1970).

Dolling, G., and Nieman, H., Nucl. Inst. Met. 49, 117 (1967).

Dymond, R.R. M.Sc. thesis (unpublished) McMaster University (1970).

Feynman, R.P., Leighton R.B., and Sands, M., The Feynman Lectures on Physics, Vol. III, Chap. 4. Addison Wesley (1965).

Gilat, G. Sol. State. Comm. 7, 55 (1969).

Gurevich, I.I., Tarasov, L.V. Low Energy Neutron Physics North Holland-Amsterdam (1968).

Hallman, E.D., Brockhouse, B.N., Can. J. Phys. 47, 1117 (1969).

Hallman, E.D. Ph.D. thesis (unpublished) McMaster University (1969).

James, R.W. The Optical Principles of the Diffraction of X-rays. Bell: London (1948).

Jones, S.L. Anal. Chim. Acta. 21, 532 (1959).

Konstantinović, J. Zivanocić, M., Davidović M., Nucl. Inst. Met. 65, 233 (1968).

Maliszewski, E., Sosnowski, J. Blinowski, K., Kozubawski, D.D., Padlo J., and Sledziewska D. Inelastic Scattering of Neutrons. IAEA II, 87 (1963).

Møller, H.B. Ph.D. thesis (unpublished) University of Copenhagen (1967).

Ng, S.C., Brockhouse, B.N., and Hallman, E.D., Mater. Res. Bull. 2, 69 (1967).

Nikotin, O.P. Nucl. Inst. Met. 72, 77 (1969).

Owen, Roberts. Phil. Mag. 27, 294 (1939).

Pearson, W.B. A Handbook of Lattice Spacing and Structure of Metals and Alloys. Pergamon Press (1958).

Reif, F. Fundamentals of Statistical and Thermal Physics. McGraw-Hill (1965).

Rowe, J.M., Ph.D. thesis (unpublished) McMaster University (1966).

Rowe, J.M., Brockhouse, B.N. and Svensson, C. Phys. Rev. Lett. 14, (1965) 554.

Roy, A.P. Ph.D. thesis (unpublished) McMaster University (1970).

Sjölander, A. Arkiv Fysik, 14, 315 (1958).

Smithells, C.J., *Metals reference book*. 3rd Edition, London: Butterworths (1962).

Svensson, E.C., Brockhouse, B.N., and Rowe, J.M. Phys. Rev. 155, 619 (1967).

Szabó, P. Nucl. Inst. Met. 5, 184 (1959).

Taylor, D.W. *Lecture Notes from Physics 731* (1970) unpublished.

Welcher, F.J. *The Analytical Uses of EDTA*. Van Nostrand Co. New York (1958).

Yu, Kagan in the *IVth IAEA Symposium on Neutron Inelastic Scattering* (Copenhagen 1968) Vol. I, p3 (English translation available from publisher).